Title

Modeling and Optimization Framework for Optical Design of Next-Generation Food Systems

Author

Mengi, Emre

Publication Date

2024

Peer reviewed|Thesis/dissertation

Modeling and Optimization Framework for Optical Design of Next-Generation Food Systems

By

Emre Mengi

A dissertation submitted in partial satisfaction of the

requirements for the degree of

Doctor of Philosophy

in

Engineering - Mechanical Engineering

and the Designated Emphasis

in

Computational and Data Science and Engineering

in the

Graduate Division

of the

University of California, Berkeley

Committee in charge:

Professor Tarek I. Zohdi, Chair
Professor Khalid M. Mosalam
Professor Francesco Borrelli

Summer 2024

Abstract

Modeling and Optimization Framework for Optical Design of Next-Generation Food Systems

by

Emre Mengi

Doctor of Philosophy in Engineering - Mechanical Engineering

and the Designated Emphasis in

Computational and Data Science and Engineering

University of California, Berkeley

Professor Tarek I. Zohdi, Chair

Agriculturally viable land has been the target of renewable energy production efforts, such as solar panels and wind turbines. The competition between energy production and agricultural production has led to restrictions on non-agricultural activity on agricultural land while pushing for sustainable agriculture and renewable energy production to reach the state's carbon-neutrality goals. Next-generation food systems are needed to alleviate such problems. The goal of this study is to analyze next-generation food systems from an optical modeling standpoint. This study develops a reduced-order geometric raytracing model to evaluate the performance of various food production systems, namely solar greenhouses, open-field agrophotovoltaics, and indoor pod farming systems. A digital-twin approach, where a digital replica of the physical system is modeled, is used to quickly and efficiently evaluate designs and optimize them using a genomic-based optimization algorithm. The digital-twin consists of modeling the optical properties of the system to accurately simulate the power distribution within the food systems through the raytracing algorithm. In addition, power sizing analysis of a real-life indoor farming system is performed. Extensions of the digital-twin framework and how it can be coupled with other physics models are provided using a crop performance driven optimization case study of an open-field agrophotovoltaic system. This computational framework and optimization scheme aims to provide a foundation for understanding, evaluating, and optimizing the food systems of the future and prove a useful tool to efficiently and sustainably produce food and generate power, driven by innovation and cutting-edge technology.

I would like to express my deepest appreciation to my advisor, Prof. Tarek I. Zohdi, for his guidance in both my research and professional development, helping me prepare for the next chapter in my life. I also would like to thank my dissertation committee for their invaluable knowledge and feedback.

Words cannot express my gratitude to my parents who provided all of their emotional and financial support to make our dreams come true. I wouldn't be where I am without them.

Lastly, I would like to thank all the people I had the pleasure of working with here at UC Berkeley and the lifelong friends I made in the Bay Area who made this journey fun and memorable.

Contents

List of Figures

List of Tables

Acknowledgments

This work has been partially supported by the UC Berkeley College of Engineering, the USDA AI Institute for Next Generation Food Systems (AIFS), USDA award number 2020-67021-32855.

Various chapters of this dissertation includes reprints of my previously published material. Chapter Two of my dissertation is a reprint of the material as it appears in *A digital twin framework for genomic-based optimization of an agrophotovoltaic greenhouse system* article published in *Proceedings of Royal Society A Journal*, co-authored with Roger S. Isied and Tarek I. Zohdi. Chapter Four of my dissertation is a reprint of the material as it appears in *A Digital-Twin and Rapid Optimization Framework for Optical Design of Indoor Farming Systems* article published in *Computational Mechanics Journal*, co-authored with Carla J. Becker, Mostafa Sedky, Shao-Yi Yu, and Tarek I. Zohdi. Chapter Six of my dissertation is a reprint of the material as it appears in *Crop-driven optimization of agrivoltaics using a digital-replica framework* article published in *Smart Agricultural Technology Journal*, co-authored with Omar S. Samara and Tarek I. Zohdi.

Chapter 1

Introduction

Agriculturally viable land has been the target of renewable energy production efforts, such as solar panels and wind turbines. The competition between energy production and agricultural production has led to restrictions on non-agricultural activity on agricultural land in California [1] while pushing for sustainable agriculture and renewable energy production to reach the state's carbon-neutrality goals [2]. Alternative solutions are needed to alleviate such problems. One possible way is by employing systems which combine solar energy generation with agricultural production, so-called agrophotovoltaic (APV) systems [3–5]. While there are many examples of APVs installed in open outdoor fields, a similar setup could be utilized for greenhouses, which offer more precise climate control of plant growth. Carbon-neutral agrophotovoltaic greenhouses, combined with vertical farming, can reduce agricultural land shortage problems and increase crop yields, regardless of the weather or season. These greenhouses also have the potential to be used in prospective space-exploration applications, where climate control and efficient use of habitable space are crucial.

Several experimental studies have been conducted on the feasibility of agrophotovoltaic greenhouse systems [6–10]. While experimental setups can provide insight for the best configuration for agrophotovoltaic systems where plant growth and energy production are maximized, physically testing all possible configurations is time-consuming and requires substantial financial undertaking.

Figure 1.1: Agrophotovoltaic greenhouse. Photo from public domain: https://pixabay.com.

Another approach to next-generation food production is through the use of indoor vertical farms, where crop production occurs in highly-controlled environments (i.e. temperature, hydroponic nutrient delivery, irradiation), supporting the continuous growth of crops throughout the year, regardless of the prevailing local climate conditions. These indoor farms can be installed in highly-populated areas, supplying fresh and local produce while offsetting the carbon footprint of food delivery from the field to the customer. The controlled environment also allows for reduced pesticide use and increased yield. With humanity grappling with food scarcity exacerbated by climate change and population growth, indoor farming emerges as a promising avenue, providing a more efficient and sustainable approach to food production. In this study, we will focus on indoor vertical farm designs with hydroponic nutrient delivery.

Hydroponics involves cultivating plants in a nutrient-rich solution, eliminating the requirement for soil. Depending on the crop, this technique can be implemented through various methods such as drip irrigation, aeroponics, nutrient film technique, ebb and flow, aquaponics, or deep-water culture. Despite the diverse physical approaches, these techniques generally follow similar principles: a specialized delivery system pumps a nutrient solution to the plants, and then the solution circulates back to a reservoir for replenishing the nutrients [11–15]. These types of methods use only 10% of the water utilized in traditional farming [16] in average since nutrients are delivered directly to the plant roots and no soil is used. Since the nutrient delivery is precise and without soil, there is also no risk of fertilizer runoff. These systems can be easily adjusted for growing a specific type of plant in the most optimal way due to the highly-controlled nature of the growing environment. However, these

systems have high start-up financial costs [17] and need high operational efficiency and yield to recoup these costs during the lifetime of the system.

Similarly, vertical indoor farming in highly controlled environments, enabled by LED lighting and hydroponic or aeroponic nutrient delivery, needs significant improvements to make it viable for crops beyond leafy greens and little work has been done to quickly and efficiently assess system performance of different indoor farming designs. A digital-twin approach for modeling and optimizing an indoor farming pod will provide a quick and efficient way of evaluating the performance of different system designs and identifying the optimal design parameters.

Figure 1.2: Indoor vertical farm. Photo from public domain: https://pixabay.com.

In order to alleviate these problems, this study will focus on building computational frameworks for different next-generation food systems to assess system performance, including solar power generation, crop growth metrics, irrigation requirements using optical modeling of the system, where various next-generation food system designs are computationally generated and light rays are tracked through a representative domain.

First, we will construct a system model for a representative agrophotovoltaic system. This involves simulating the absorption and reflection of solar rays on three-dimensional thin film panels enveloping the greenhouse. The simulation technology is then integrated with genomic optimization algorithms to determine system parameters, aiming to optimize the greenhouse's performance. While the agrophotovoltaic studies previously mentioned have either experimentally or computationally tested APV designs to find the best design,

the proposed framework will enable the user to quickly evaluate solar greenhouse designs with the reduced order model and find the "optimal" configuration within the design space using the genomic optimization framework. This would reduce the experimental testing of greenhouse designs to the top designs found by the genomic-based optimizer.

The system presents many challenges with regard to optimizing solar farm characteristics to ensure energy and agricultural needs are simultaneously met. The goal would be to balance plant growth and energy generation in a way where the greenhouse is self-sufficient and carbon neutral. In this study, a reduced-order digital-twin is proposed that allows the user to simulate a day of irradiation in seconds, which allows for optimization of system parameters on the order of minutes. Thus, the simulated APV greenhouse can be regarded as a digital-twin that can be simulated and optimized in real-time. It is noted that the optimized designs outputted by the genomic optimization algorithm can be then fed into higher fidelity models to evaluate the best designs further. This virtual setup allows the user to reduce the time and capital spent on the experiments to develop a carbon-neutral greenhouse APV system.

The greenhouse structure simulated provides a foundation for the capabilities of the raytracing model to accurately evaluate the power distribution within agrophotovoltaic systems. The next addition to the simulation will be modeling the interior of the greenhouse in terms of the plant configuration, namely the hydroponic structures. Greenhouses employ a variety of different configurations to grow plants. These include: (1) planting the crops in soil similar to an open field and using the greenhouse structure for sole purpose of climate control and protection from weather elements, (2) placing potted plants on benches in the greenhouse and repotting them as they grow, or (3) stacking them vertically by utilizing the most amount of space possible and precisely delivering nutrients to exposed roots. The third method is called vertical farming and includes the use of aeroponics and hydroponics [18], which we will focus on modeling the latter in terms of solar power absorption of plants and irrigation pump power requirements.

We will follow closely the digital twin framework used for the initial solar greenhouse model, where we will simulate different greenhouse geometries, as well as different hydroponic tower configurations, including the tower shape, sizing, refractive index, and proximity of towers to each other. The resulting solar power distribution within the system, namely the solar panel and plant energy absorption, and the irrigation pump power requirements will determine the "fitness" of the agrophotovoltaic design.

In addition to the increase in the popularity of agrophotovoltaic greenhouses, AI in food systems are moving towards aeroponic or hydroponic farming in indoor spaces, where light, nutrients, and water is precisely controlled and artifically supplied. One can extend the raytracing capabilities described in this dissertation so far to optical modeling and optimization of indoor farming systems. In this chapter, we will evaluate the optical performance of an indoor farming pod where plants are situated in vertical and horizontal racks. The indoor farming pod design parameters will consist of the LED properties, namely the aperture, lighting area per face, and the irradiated power on each side of the pod. A similar raytracing algorithm will be used to evaluate power absorption of the targets, a.k.a. plants, to deter-

mine the design fitness. Then, the aforementioned genomic optimizer will be used to find the optimal set of LED design parameters that produce the "best" indoor farming pod design.

(a) (b)

Figure 1.3: Solar farms. Photos from public domain: https://pixabay.com.

We have so far mentioned a digital-twin approach where the computational model of the system will inform the design of the real-life system. The next chapter will then bridge the gap between the models described in this dissertation with a real-life application of a next-generation food production system by analyzing an indoor farm in terms of its power requirements. The power sizing of an indoor farming system coupled with a solar farm and energy storage system will be performed on a UC Berkeley indoor farming container that is located at Richmond Field Station, CA. The power sizing of the indoor farming system will consist of determining the solar farm and energy storage system size and specifications needed to match the power draw of the equipment needed to run the farm within a day.

Lastly, we will look at possible extensions of the light-based simulation methods developed in this dissertation and how they can be connected to different physics models. The raytracing model developed can be used for a similar agrophotovoltaic setup for an open-field agricultural configuration. While the energy optimization function that evaluates the power absorption of surfaces provides a good starting point, the intricacies of crop growth require us to model the crop dynamics of the system for a more accurate system optimization framework. Therefore, this presents a great way to demonstrate how the optical model can be combined with a crop model in order to optimize the agrophotovoltaic system using crop performance and solar energy production metrics. The light model is run to obtain the solar panel power absorption and ground surface power absorption. Daily radiation values obtained through the light-based simulation are then passed into the crop model which calculates the reference and agrivoltaic crop yield. The crop model then outputs agrophotovoltaic and reference crop yields as well as other crop performance metrics. The light model simulates the sun's position for the crop season and calculates average ground radiation, which is then passed onto the crop model to calculate the crop biomass, evapotranspiration, water, and light use for a given agrophotovoltaic design. This routine is repeated for each

agrophotovoltaic design in the genetic optimizer in each generation to calculate the design fitness, rank designs, and use evolutionary principles to retain the best performers.

In summary, the goal of this study is to develop a reduced-order geometric raytracing model that can be used for system performance analysis for next-generation food systems and apply genomic-based optimization algorithms to improve system performance. Agrophotovoltaic greenhouse and indoor farming pod systems are used to demonstrate the capabilities of the computational framework. In addition, power sizing analysis of a real-life indoor farming system is performed. Extensions of the digital-twin framework and how it can be coupled with other physics models are provided using a crop performance driven optimization case study of an open-field agrophotovoltaic system.

Chapter 2

Solar Greenhouse Raytracing

The push for sustainable agriculture enabled various next-generation food production systems to be developed. One of the most prominent systems are what are called agrophotovoltaics (APVs). These systems enable food production and power generation to exist in the same domain. Example APV systems include (1) open-field agrophotovoltaics which crop production or livestock grazing occurs underneath an array of solar panels that provide both shade and energy production, (2) greenhouses that incorporate solar panels on the structure while allowing portions of the light to go into the greenhouse for crop production.

We will start developing our modeling and optimization framework by capturing the physics of light scattering in a solar greenhouse where the absorption and reflection, and refraction of solar rays hitting 3-dimensional thin film panels wrapped around the greenhouse is simulated (see Figure 1.1) [19]. This simulation technology is combined with genomic-based machine learning algorithms in order to ascertain the "optimal" system design parameters to maximize greenhouse food and energy production.

2.1 Model Overview

While the agrophotovoltaic studies previously mentioned have either experimentally or computationally tested APV designs to find the best design, the proposed framework in Figure 2.1 will enable the user to quickly evaluate solar greenhouse designs with the reduced order model and find the "optimal" configuration within the design space using the genomic optimization framework. This would reduce the experimental testing of greenhouse designs to the top designs found by the genomic-based optimizer.

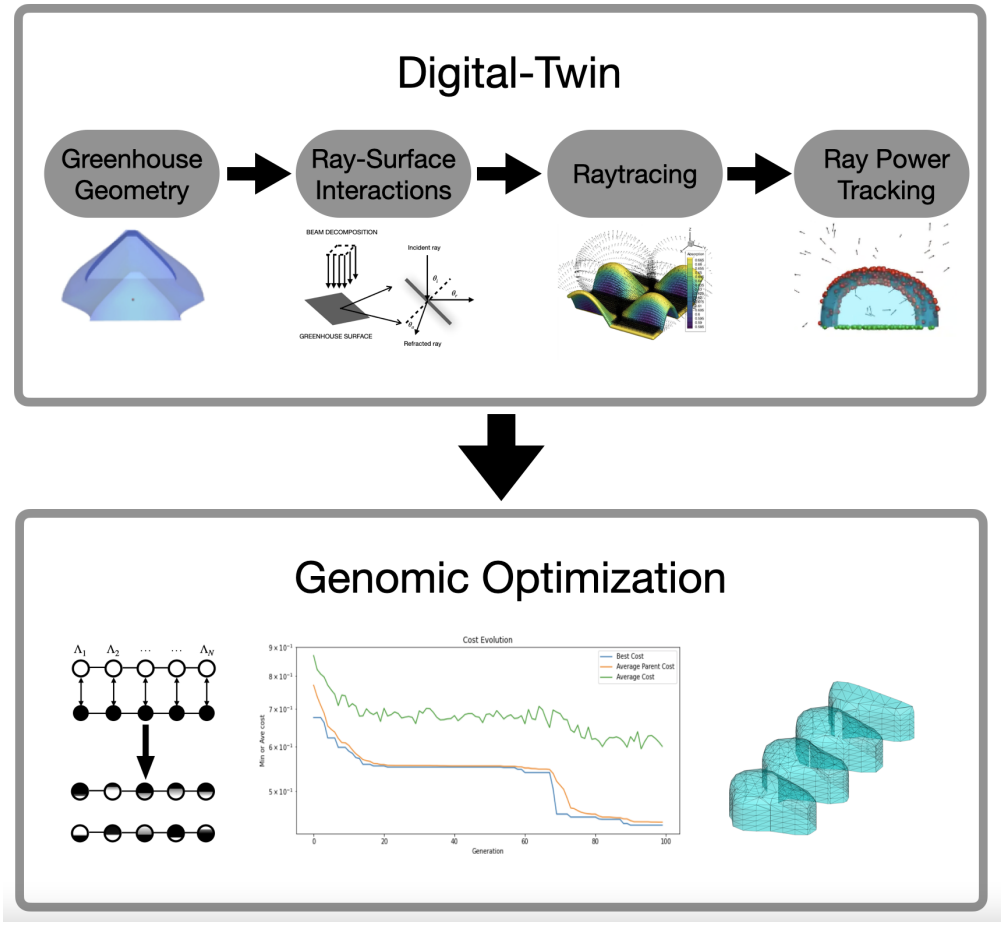

Figure 2.1: Digital-twin and genomic optimization framework.

In this study, the system parameters are greenhouse shape, solar panel translucency and solar panel refractive index. It is important to note that the complexity in determining the optimal translucency of the solar panels poses a significant challenge. La Notte et al. [20] presents novel translucent PV-cell technologies that use organic solar cells (OSC), dye-sensitized solar cells, and perovskite solar cells (PSC). These approaches utilize the wavelength-sensitive nature of photosynthesis, which favors radiation in the 400-700 nm range, called photosynthetically active radiation (PAR). These special solar cells absorb light outside of the PAR and transmit PAR to plants, where it is absorbed by the chlorophyll. Wavelength-specific transmittance of the solar panels can be part of the optimization algorithm to determine the optimal solar-cell technology to be used, as well as to aid the design of new solar cells with specific transmittance parameters on a per-plant basis.

The system presents many challenges with regard to optimizing solar farm characteristics to ensure energy and agricultural needs are simultaneously met. The goal would be to balance plant growth and energy generation in a way where the greenhouse is self-sufficient and

carbon neutral. Accordingly, in this work, a computational framework is developed to trace light rays through agrophotovoltaic greenhouses, in order to calculate the power generated by greenhouse solar cells, as well as the power absorbed by crops within the greenhouse. A geometric ray-tracing algorithm is developed to track the propagation, reflection, and refraction of light interacting with a translucent greenhouse. Genomic-based optimization techniques are utilized to meet a target greenhouse power generation level, as well as a targeted photosynthetic power absorption by optimizing the geometry, translucency, and material characteristics of the greenhouse. Representative numerical examples are provided. The framework can be used to generate tailored, temporal and location-specific, greenhouse designs.

There are high-fidelity light and plant modeling tools, such as HELIOS and Raytrace3D, which would most accurately simulate the energy distribution in agro-solar environments and provide useful insight into power generation and crop production while needing extensive libraries and relatively more computational power. In this study, a reduced-order digital-twin is proposed that allows the user to simulate a day of irradiation in seconds, which allows for optimization of system parameters on the order of minutes. Thus, the simulated APV greenhouse can be regarded as a digital-twin that can be simulated and optimized in real-time. It is noted that the optimized designs outputted by the genomic optimization algorithm can then be fed into higher fidelity models to evaluate the best designs further. This virtual setup allows the user to reduce the time and capital spent on the experiments to develop a carbon-neutral greenhouse APV system. We aim to create a digital-replica of a solar greenhouse to optimize land use and energy generation by calculating the ground and solar panel power absorption due to solar light-scattering within the system. This approach has the potential to deliver a tailored, situation-specific, self-sufficient agrophotovoltaic greenhouse system.

2.2 Physical Model and System Optimization

Creating Solar Panel Geometries

Surface functions are assumed to be known for the roof and side walls of the greenhouse $F(x_1, x_2, x_3)$. The ground is assumed to be flat at a constant height $x_3 = 0$. We check for light interactions between the greenhouse or ground by checking if $F(x_{1,j}, x_{2,j}, x_{3,j}) \leq 1$ for the greenhouse surface or if $x_{3,j} \leq 0$ for the ground. The ray position at the time of surface impact is used to compute the absorptivity and reflectivity of that beam.

We can use a generalized equation for an ellipsoid appended with a generalized sinusoid equation to represent a broad range of greenhouse geometries centered at the origin:

$$F(x_1, x_2, x_3) = \left|\frac{x_1}{R_1}\right|^{p_1} + \left|\frac{x_2}{R_2}\right|^{p_2} + \left|\frac{x_3}{R_3}\right|^{p_3} + a_1 \sin(\omega_1 x_1) + a_2 \sin(\omega_2 x_2) \leq 1 \tag{2.1}$$

where (R_1, R_2, R_3) are the generalized radii, (p_1, p_2, p_3) are the exponents of the generalized ellipsoid, (a_1, a_2) are the amplitudes of the sinusoid, and (ω_1, ω_2) are the associated frequencies of the sinusoid component. These scaling factors will be the design parameters used to optimize the shape of our greenhouse. It is assumed the solar panels will be form-fitted to the shape of the greenhouse. The resulting topology of the greenhouse can range from simple geometrical shapes to complex sinusoidal shapes, as visualized in Figure 2.2. The generalized radii and exponents control the ellipsoidal features of the greenhouse while the amplitudes and frequencies control the sinusoidal features. The contour nature of the greenhouse equation enforces an infinitely long greenhouse along its length. For visual purposes, the domain of the greenhouse has been constrained by the domain of simulated light rays. In practice, one can extend the cyclical greenhouse design according to land available.

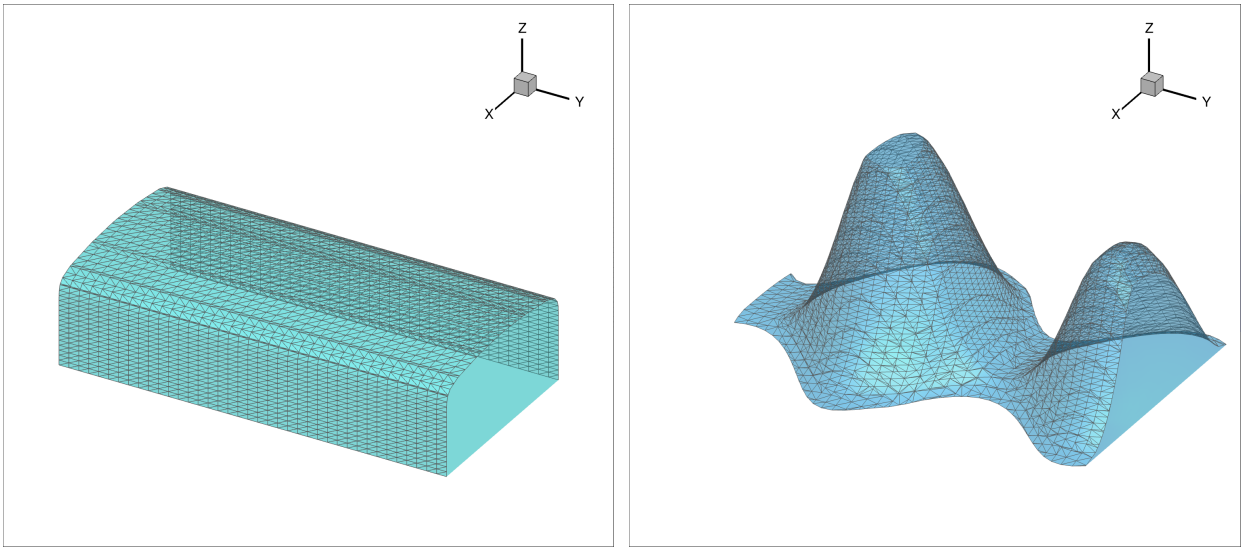

(a) (b)

Figure 2.2: Example greenhouse shapes for (a) $(R_1, R_2, R_3) = (0.5, 5, 0.5)$, $(p_1, p_2, p_3) = (20, 20, 20)$, $(a_1, a_2) = (0, 0)$, $(\omega_1, \omega_2) = (0.1, 0.1)$ and (b) $(R_1, R_2, R_3) = (0.5, 5, 0.5)$, $(p_1, p_2, p_3) = (0.5, 20, 0.5)$, $(a_1, a_2) = (0.5, 0.5)$, $(\omega_1, \omega_2) = (4, 7)$.

Reflection and Absorption of Rays

We assume the rays travel through a vacuum and thus we can use the nominal speed of light $(3 \times 10^8\ m/s)$. The design string parameters that are refined by the genomic-based optimizer can be selected by the user. The total power per surface area is given by P_{tot} which is evenly distributed among the rays based on the total area of light cover being considered A_b. The ray positions are generated randomly over a square region with a side length of $2s_{Reg}$. The center of the region is defined to follow the sun's trajectory during the day,

meaning that each run of the simulation will base the square beam at a point at which the beam is calculated to hit the greenhouse at that specific beam angle.

With these parameters, we can define the power per ray in a light pulse as follows:

$$P_r = \frac{P_{tot} A_b}{N_r} \tag{2.2}$$

We follow a standard euclidean basis $(\boldsymbol{e}_1, \boldsymbol{e}_2, \boldsymbol{e}_3)$ indicating horizontal, vertical, and in depth directions. To obtain the angle of incidence of the ray of light, θ_i, we first compute the inward unit surface normal vector $\boldsymbol{n}$ of the greenhouse surface F given by:

$$\boldsymbol{n} = \frac{-\nabla F}{||\nabla F||} \tag{2.3}$$

where

$$\nabla F = \frac{\partial F}{\partial x_1}\boldsymbol{e_1} + \frac{\partial F}{\partial x_2}\boldsymbol{e_2} + \frac{\partial F}{\partial x_3}\boldsymbol{e_3} \tag{2.4}$$

is the gradient of the greenhouse surface equation. Note that for the flat ground, the inward normal vector is constant and defined by $\boldsymbol{n}_g = [0, 0, -1]$. Next, we can then compute the angle of incidence (θ_i) via the cosine formula between the ray velocity vector $(\boldsymbol{v})$ and the inward unit normal vector of the solar panel surface $(\boldsymbol{n})$:

$$\theta_i = \cos^{-1}\left(\frac{\boldsymbol{v}_j \cdot \boldsymbol{n}_j}{\|\boldsymbol{v}_j\|\|\boldsymbol{n}_j\|}\right) \tag{2.5}$$

The component of the ray velocity normal to the surface of the solar panel is given by

$$\boldsymbol{v}_{j,\perp} = \|\boldsymbol{v}_j\| \cos\theta_i \boldsymbol{n}_j \tag{2.6}$$

We can calculate the outgoing reflected velocity $(\boldsymbol{v}_j^{\text{ref}})$ by turning the inbound normal velocity outward by subtracting it twice:

$$\boldsymbol{v}_j^{\text{ref}} = \boldsymbol{v}_j - 2\boldsymbol{v}_{j,\perp} \tag{2.7}$$

Next, we consider the material properties of the solar panel. We define $\hat{n}$ as the ratio of the refractive indices of the ambient (incident) medium (n_i) and absorbing medium (n_a) such that

$$\hat{n} = \frac{n_a}{n_i} \tag{2.8}$$

The absorbing medium refractive index, n_a (solar panel), is to be user designed based on the optimization model. We assume the incident refractive index to be that of a vacuum as $n_i = 1$. Figure 2.3 outlines the decomposition of an individual ray on the greenhouse surface.

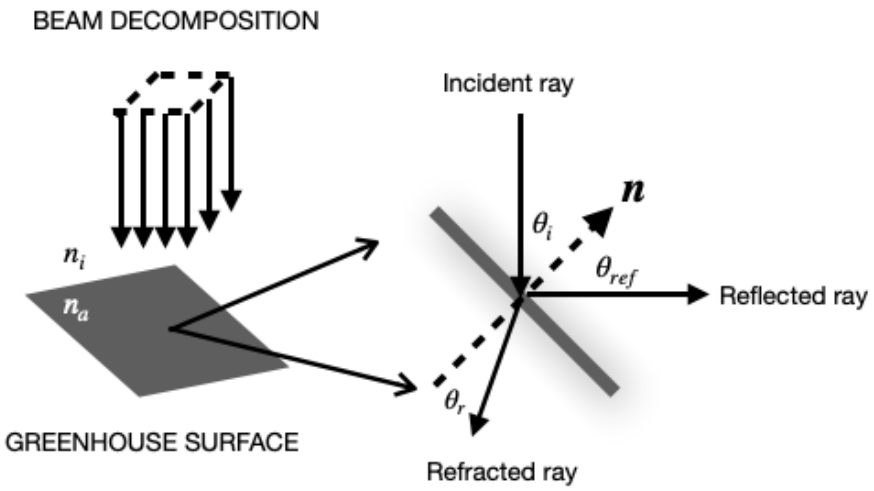

Figure 2.3: Beam decomposition for a geometric ray-tracing model.

With the above parameters defined, the refractive angle of incoming light can be obtained using Snell's law, namely:

$$\theta_r = \sin^{-1}(\frac{1}{\hat{n}}\sin(\theta_i)) \tag{2.9}$$

This angle is utilized for the light rays traveling into and out of the greenhouse. It is assumed that once refracting through the solar panel, the inner medium of the greenhouse is the same as that of outside the greenhouse. It is also assumed that the solar panel is sufficiently thin such that the change in curvature between the outer and inner surface is negligible. For computational efficiency, the refracted light rays were not tracked through time within the surface of the solar panel. Rather, refracted rays were manually translated through the medium according to Figure 2.4.

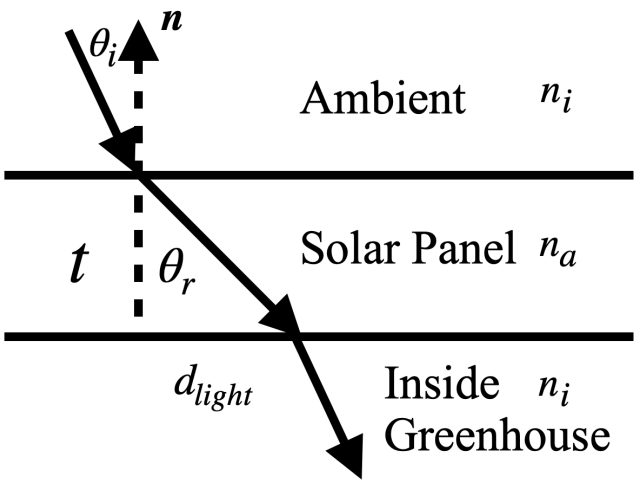

Figure 2.4: Evolution of light refraction through wall of greenhouse.

In this figure example, the light travels from the ambient environment, through the solar panel, and into the greenhouse. We define t as the thickness of the solar panel, θ_r as the refractive angle, and d_{light} as the translational distance the light ray travels before exiting the solar panel. Since it is assumed that the medium inside and outside of the greenhouse is the same, the light retains its initial incidence angle θ_i once it enters the greenhouse. Accordingly, the translational distance can be calculated as follows:

$$d_{light} = t \tan(\theta_r) \tag{2.10}$$

In practice, each light ray is manually translated according to Equation 2.10 when it comes in contact with the solar panel surface for both incoming and outgoing rays.

Power Tracking and Splitting

We consider a ray of light incident upon a material interface which produces a reflected ray and a transmitted/absorbed (refracted) ray. The ratio of reflected electromagnetic power (I_r) to the total incident electromagnetic power (I_i) defines the total reflectance $\mathcal{IR} \equiv \frac{I_r}{I_i}$ where $0 \leq \mathcal{IR} \leq 1$ for unpolarized electromagnetic radiation. We refer the reader to Zohdi [21] for a detailed derivation of $\mathcal{IR}$. The reflectance is a function of the angle of incidence of the incoming rays, the medium which the rays travel through, and the material which the rays intersect with. For this model, we will consider applications with non-magnetic media and frequencies where the magnetic permeability is virtually the same for both the incident and absorbing medium. Following Zohdi [21], we define the reflectivity $\mathcal{IR}$ as follows:

$$\mathcal{IR}(\hat{n}, \theta_i) = \frac{I_r}{I_i} = \frac{1}{2}\left(\frac{\hat{n}^2\cos\theta_i - (\hat{n}^2 - \sin^2\theta_i)^{\frac{1}{2}}}{\hat{n}^2\cos\theta_i + (\hat{n}^2 - \sin^2\theta_i)^{\frac{1}{2}}}\right)^2 \tag{2.11}$$

$$+\frac{1}{2}\left(\frac{\cos\theta_i - (\hat{n}^2 - \sin^2\theta_i)^{\frac{1}{2}}}{\cos\theta_i + (\hat{n}^2 - \sin^2\theta_i)^{\frac{1}{2}}}\right)^2$$

The reflectance is used to obtain the total amount of absorbed power by a material as follows:

$$P_{abs} = (1 - \mathcal{IR})P_r \tag{2.12}$$

We track the total power and position of a ray and stop tracking it if either the ray has moved outside of the user defined domain, or the ray's power is reduced below a user defined threshold.

The power absorbed by the ground and solar panel surfaces are obtained using the following flowcharts, shown in figures 2.5 and 2.6 during reflectance/absorptivity calculations that occur within the ray-tracing algorithm.

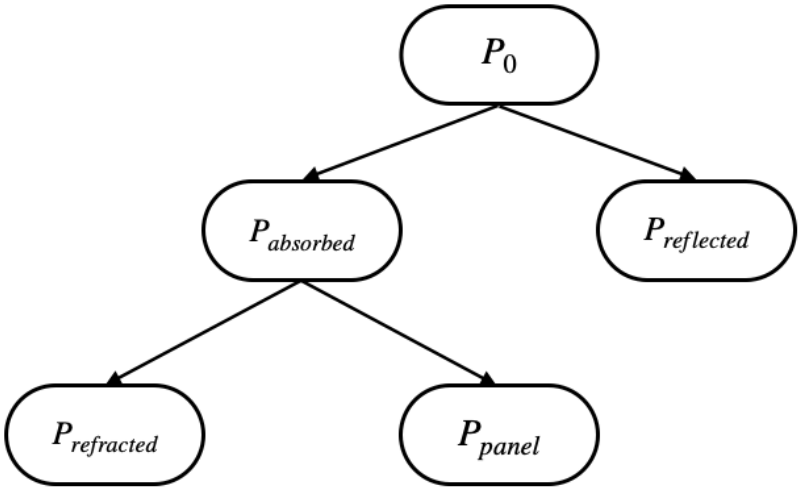

Figure 2.5: Power distribution on solar panels.

The incident light rays which come in contact with the solar panel are split into reflected, refracted, and power-converted light rays. The light that refracts into the greenhouse is based on the transmissibility of the solar panel defined by $\gamma \in [0, 1]$. The refracted power $P_{refracted}$ is set to be proportional to the transmissibility, namely:

$$P_{refracted} = \gamma P_{absorbed} \tag{2.13}$$

whereas the utilized light contains the remaining power, namely

$$P_{panel} = (1 - \gamma) P_{absorbed} \tag{2.14}$$

Similarly, the power distribution of the refracted ray when it hits the ground surface is determined by the reflectance parameter.

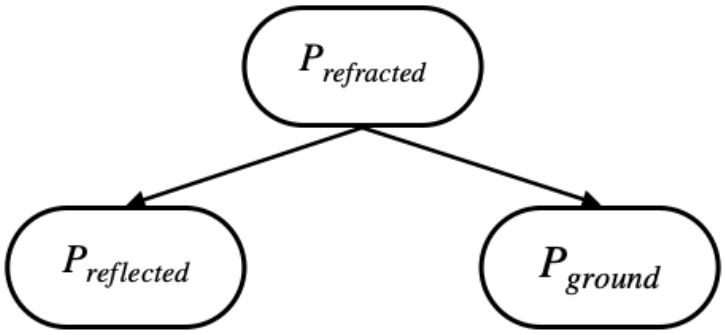

Figure 2.6: Power distribution on the ground.

While the power conversion efficiencies of the solar panels and the plants are dependent on ambient parameters, this study only takes the surface power absorption into account for simplicity.

Time-stepping Algorithm

We use the power propagation and ray-tracing algorithm described above in conjunction with an explicit time-stepping scheme (Forward Euler Method) to track the rays from time $t = 0$ to $t = t_{final}$ or until all rays are deactivated, whichever comes first. The time-stepping algorithm is as follows for all light rays $j = 1, \ldots, N_r$:

1. Initialize ray positions $\boldsymbol{r}_j(t = 0)$ and velocities $\boldsymbol{v}_j(t = 0)$
2. Iterate ray positions in time using:

$$\boldsymbol{r}_j(t + \Delta t) = \boldsymbol{r}_j(t) + \Delta t \boldsymbol{v}_j(t) \tag{2.15}$$

3. Check for surface-ray collisions. If ray has collided with a surface:
   a) Update power absorbed by the surfaces ($P_{abs} = (1 - \boldsymbol{\mathcal{IR}})P_r$) and remaining power for all rays ($P_{ref,_j} = \boldsymbol{\mathcal{IR}}_j P_{r,j}$),

b) Calculate new ray velocity values after reflection $\boldsymbol{v}_j^{ref}$,

c) Calculate ray refractions if ray hits the greenhouse surface,

4. Check for active rays:

a) **If no active rays are remaining:** End simulation,

b) **Otherwise:** Move to the next step,

5. Increment the time step to $(t = t + \Delta t)$ and go back to Step 2.

The time-step size Δt is chosen accordingly to capture all ray surface interactions using the formula $\Delta t = \xi \frac{h_0^{ray}}{c}$, where h_0^{ray} is the initial height of the generated rays, c is the speed of light, and ξ is a tunable parameter such that $\xi \in (0, 1]$. The high velocity of the light rays requires a time step size scaled to accurately observe the motion of the rays with a sufficient number of time steps. For this study, the parameter was chosen to be $\xi = 0.01$. This parameter was chosen to be sufficiently small to capture all ray interactions, while not causing a significant bottleneck for simulation time. Further refinement of this parameter can be obtained by conducting a convergence study in which an average F is calculated for all surface ray interactions as a function of ξ.

Process Optimization

The "design string" for this process contains all 8 controllable constants:

$$\boldsymbol{\Lambda}^i \equiv \{\Lambda_1^i, ..., \Lambda_N^i\} \equiv \{\gamma, \hat{n}_s, p_1, p_3, a_1, a_2, \omega_1, \omega_2\} \tag{2.16}$$

where γ is the transmissibility of the solar panels and $\hat{n}_s$ is the refractive index of the solar panels. These parameters can be controlled within user-specified bounds. All system parameters used in this simulation are displayed within Table 6.3.

A good set of characteristic parameters of our greenhouse design will allow for user-defined absorptivity of the solar panels (for energy production) as well as absorbed light by the ground (for plant growth). These two opposing objectives force the optimizer to design a solution which balances the two goals. It should be noted that this model does not penalize for over-irradiation/heating of crops in a time period throughout the day given that this framework is developed independently of specific crop characteristics. An application of this framework to a specific set of crops should consider this in choosing $P_{plant,des}$ and add a penalty term to the cost function which drastically increases the crops if the photosynthetic power exceeds a power threshold detrimental to the crops' growth.

With these objectives in mind, we construct the following cost function,

$$\Pi = w_1 \left| \frac{P_{solar,des} - P_{elec}}{P_{solar,des}} \right| + w_2 \left| \frac{P_{plant,des} - P_{photosynth}}{P_{plant,des}} \right| \tag{2.17}$$

where the weights are chosen to be $w_1 = 2$ and $w_2 = 1$. The weights can be assigned arbitrarily by the user as long as they are positive and reflect the relative importance of each objective term. The choice of weights in this work's numerical example is chosen to prioritize designs in which the electrical power is as close to the desired solar power as possible. Each term in equation 3.15 attempts to set power absorbed by the solar panels and power absorbed for plant growth as close as possible to their desired counterparts, $P_{solar,des}$ and $P_{plant,des}$. Note that all terms in the cost function are non-dimensional.

Process Optimization Scheme: Genetic Algorithm

The greenhouse digital twin is optimized using a genetic algorithm. All genetic algorithm parameters and search bounds chosen are displayed in Table 6.3. For applying a genetic algorithm, the algorithm is as follows:

1. Generate S random genetic strings, where $\mathbf{\Lambda}_i \in [\Lambda_i^-, \Lambda_i^+]$

$$\mathbf{\Lambda} = (\mathbf{\Lambda}^{(1)}, \mathbf{\Lambda}^{(2)}, ..., \mathbf{\Lambda}^{(i)}, ..., \mathbf{\Lambda}^{(S)}) \tag{2.18}$$

where

$$\mathbf{\Lambda}^{(i)} = \begin{pmatrix} \gamma^- \leq \gamma^{(i)} \leq \gamma^+ \\ \hat{n}_s^- \leq \hat{n}_s^{(i)} \leq \hat{n}_s^+ \\ p_1^- \leq p_1^{(i)} \leq p_1^+ \\ p_3^- \leq p_3^{(i)} \leq p_3^+ \\ a_1^- \leq a_1^{(i)} \leq a_1^+ \\ a_2^- \leq a_2^{(i)} \leq a_2^+ \\ \omega_1^- \leq \omega_1^{(i)} \leq \omega_1^+ \\ \omega_2^- \leq \omega_2^{(i)} \leq \omega_2^+ \end{pmatrix} \tag{2.19}$$

2. Compute fitness of each string by evaluating $\Pi(\mathbf{\Lambda}^{(i)}) \; \forall \; i$

3. Rank the genetic strings where the top rank has the minimum cost function $\Pi(\mathbf{\Lambda}^{(i)})$

4. Mate the top pairs of genetic strings to obtain 2 children, such that:

$$\mathbf{\Lambda}^{(ci)} = \begin{pmatrix} \gamma^{pi}\phi_1 + \gamma^{p(i+1)}(1-\phi_1) \\ ... \\ ... \\ \omega_2^{pi}\phi_8 + \omega_2^{p(i+1)}(1-\phi_8) \end{pmatrix}$$

where $\phi_j \in$ rand[0,1].

$$\mathbf{\Lambda}^{(c(i+1))} = \begin{pmatrix} \gamma^{p(i+1)}\hat{\phi}_1 + \gamma^{pi}(1-\hat{\phi}_1) \\ \cdots \\ \cdots \\ \omega_2^{p(i+1)}\hat{\phi}_8 + \omega_2^{pi}(1-\hat{\phi}_8) \end{pmatrix}$$

where $\hat{\phi}_j \in$ rand[0,1].

5. Remove bottom $S - P$ original strings from population. Generate $S - P - P$ new random genetic strings.

6. Repeat steps 2-5 with a new population until either one of these conditions is met:

   - G generations has been reached.
   - $min(\Pi) \leq TOL$.

2.3 Results

Convergence Study

A convergence study was conducted to observe the dependence of the physical model on sources of randomness of the simulation. The variance of the cost was observed as a function of the number of rays in the simulation. To do so, a single set of design parameters were chosen. For each number of rays tested, the simulation was run 100 times, and the cost parameters were saved.

Figure 2.7 outlines the results of the sensitivity study. Figures 2.7a, b, and c depict the variance of the overall cost, the solar cost, and the plant cost parameter over 100 test runs for the same design parameters. Figure 2.7d summarizes the standard deviation of the performance parameters as the number of rays increases. For the chosen number of rays for the numerical example outlined in the next section (500 rays), the standard deviation for all of the parameters falls below 3×10^{-3}.

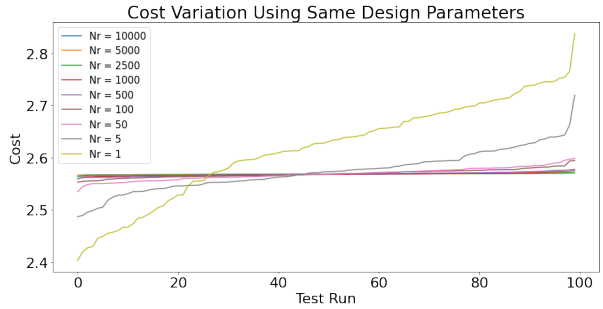

(a) Sensitivity of Total Cost over 100 simulation runs

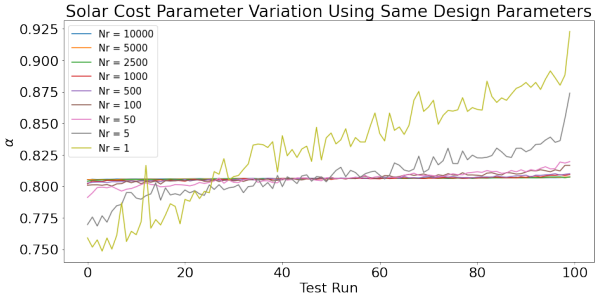

(b) Sensitivity of Solar Cost Parameter over 100 simulation runs

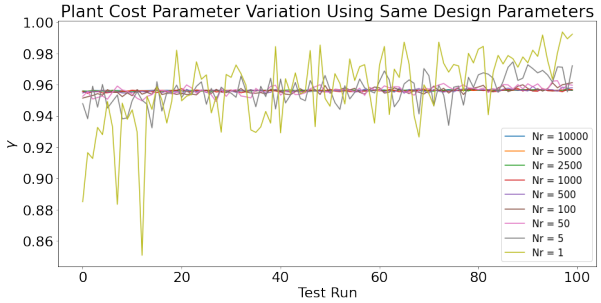

(c) Sensitivity of Plant Cost Parameter over 100 simulation runs

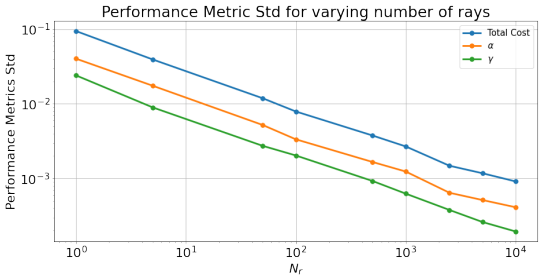

(d) Standard Deviation of Cost Parameters for varying Number of Rays

Figure 2.7: Summarized Results of Sensitivity Study

In choosing a representative numerical example discussed in the following section, it was important to consider a number of rays that would lead to reproducible and accurate results while not sacrificing efficiency of the simulation.

Numerical Example

A numerical example is generated based on the model previously described (source code available at https://github.com/ucb-msol/AgroPV.git). A single "flash" of light was used to represent an hour of irradiation. The *pysolar* python package was used to determine the azimuth and elevation angle of the incoming rays of light for a specified date, time, and location [22]. Based on these angles, the clear sky solar irradiance was determined from the package. The greenhouse was simulated for July 1st, 2021 in Berkeley, California. Figure 2.8 outlines the solar irradiance distribution over the simulated day and location. It was assumed that the greenhouse had no obstruction from the sun in its surroundings, and there were no terrain obstructions on the sun throughout the day. The model can be trivially extended to include terrain obstructions but was not considered for this study.

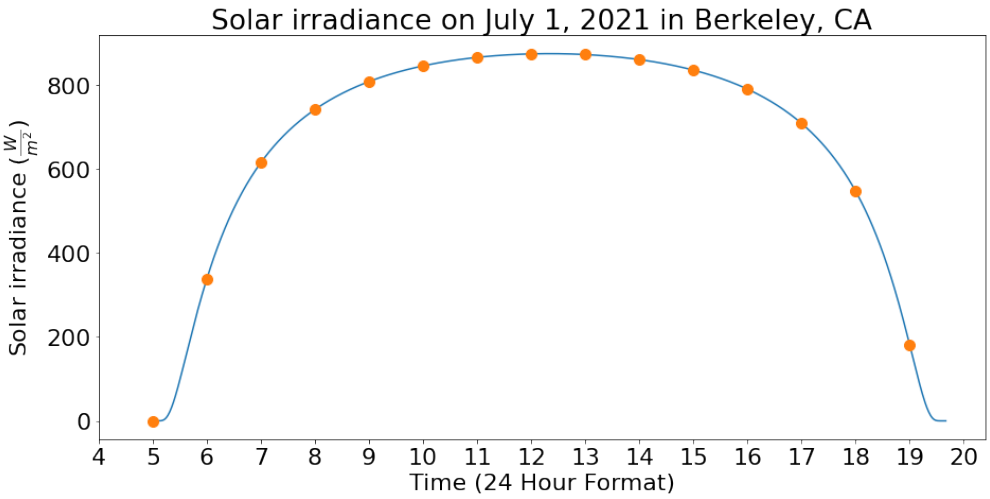

Figure 2.8: Evolution of clear sky solar irradiance on July 1st, 2021 in Berkeley, California.

The simulation was run for every hour throughout the day at which the altitude of the sun was above the horizon. For this particular time of year, the sun was located over the horizon from the hours of 5:00 and 19:00. As such, 15 iterations of the ray-tracing simulation were conducted for each design to determine its associated cost. The physical parameters used in the system are outlined in Table 6.1. The ground refractive index was chosen based on that of a leaf [23]. The fixed geometric exponent in the $\mathbf{e}_2$ axis was chosen to ensure the projected shape of the greenhouse would be rectangular from an aerial view. Lastly, the fixed generalized radii were fixed to allow the topology optimizer to be agnostic to the size of the incoming beam of light. This allowed for topological updates focused on the shape and waveform of the greenhouse rather than its size. A volume penalty term could be added to the cost if space constraints are of concern for a particular system.

Table 2.1: Numerical Example - Greenhouse System Parameters

Symbol	Type	Units	Value	Description
N_r	scalar	none	500	Number of light rays
n_g	scalar	none	1.4	Ground refractive index
c	scalar	m/s	3×10^8	Speed of light
t	scalar	m	0.1	Solar panel thickness
$[R_1, R_2, R_3]$	scalar	none	$[0.5, 5, 0.5]$	Generalized radii
p_2	scalar	none	20	Geometric exponent

Table 6.3 outlines the parameters used to set up the genetic algorithm in the numerical example shown. The number of design strings, parents, and generations were chosen to

be relatively low to highlight the efficacy of the computational framework without looking for a true optimized solution. The search bounds for the solar panel transmissibility were chosen from opaque to transparent. The solar refractive index was designed for optimal light reflection and refraction angles. It does *not* account for the particular wavelengths of the incoming rays. This is discussed further in Section 2.4. Ultimately, the search bound parameters chosen for this example are arbitrary as further verification and application of this framework requires an advanced degree of expertise in manufacturing, material, and ambient constraints to drive realistic search bounds for the design parameters of this system.

Table 2.2: Numerical Example - Genomic Optimization Parameters

Symbol	Type	Units	Value	Description
parents	scalar	none	6	Surviving strings for breeding
S	scalar	none	20	Designs per generation
G	scalar	none	200	Total generations
$[\gamma^-, \gamma^+]$	scalar	none	[0.25,1]	Solar panel transmissibility
$[\hat{n_s}^-, \hat{n_s}^+]$	scalar	none	[2,5]	Solar panel refractive Index
$[p_{1\ or\ 3}^-, p_{1\ or\ 3}^+]$	scalar	none	$[1, 20]$	Geometric exponents
$[a_{1\ or\ 2}^-, a_{1\ or\ 2}^+]$	scalar	none	$[0, 1.75]$	Sinusoid amplitudes
$[\omega_{1\ or\ 2}^-, \omega_{1\ or\ 2}^+]$	scalar	none	$[0, 10]$	Sinusoid frequencies
w_1	scalar	none	2	Weight of solar panel power in net cost
w_2	scalar	none	1	Weight of photosynthetic power in net cost
$P_{solar,des}$	scalar	W	$1/3\ P_0$	Desired power absorbed by solar panel
$P_{plant,des}$	scalar	W	$1/6\ P_0$	Desired power absorbed by plants

Figure 6.4 depicts the convergence of the cost function across 200 generations. The figure at the top indicates the cost of the best performing design after each generation while the figure at the bottom highlights the average cost of the parent strings at the end of each generation. The optimal design string parameters at the end of the final generation are displayed in Table 6.4. The uncertainty in the cost was determined using the results of the convergence study, and is reported with a 95% confidence interval over 100 test runs. Given the limited number of generations used, uncertainty in the optimal design parameters is not trivially quantifiable given the random nature of the genomic-based optimizer and the non-convexity of the cost function.

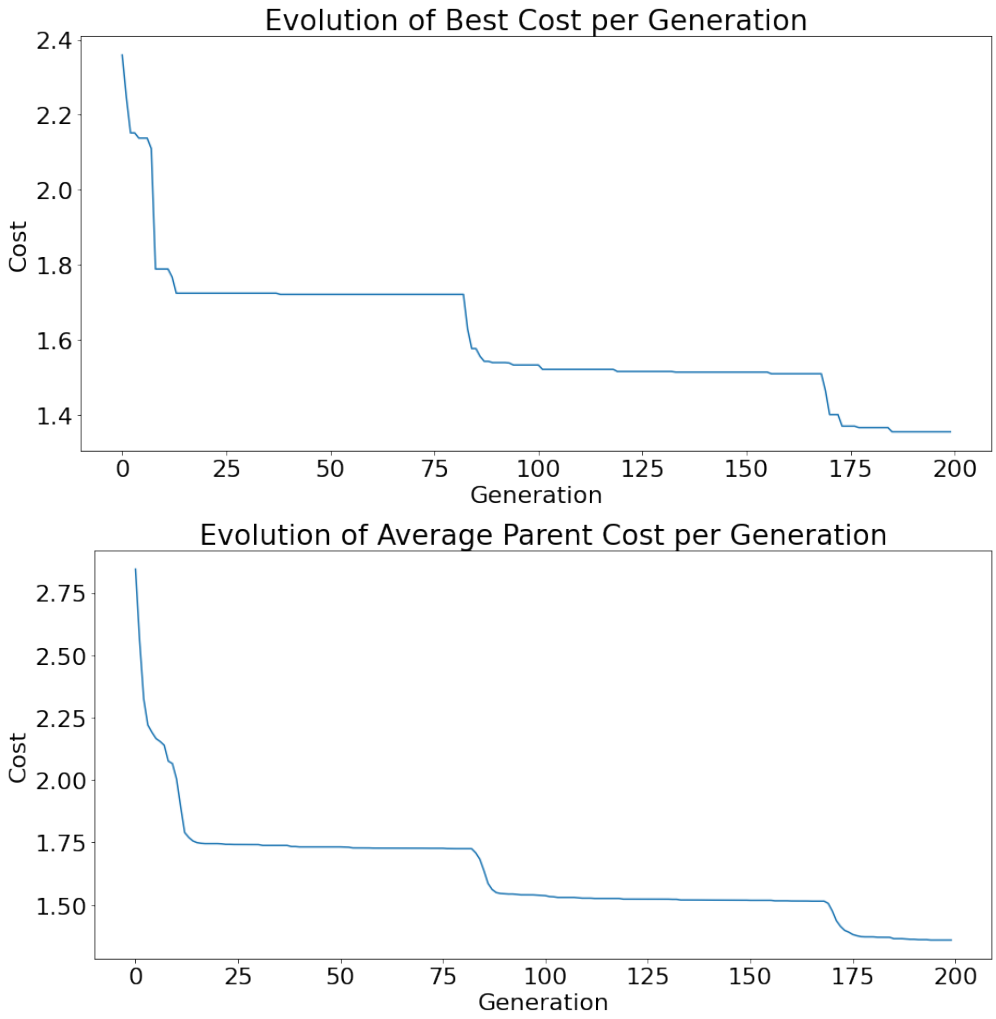

Figure 2.9: Evolution of best cost (top) and average parent cost (bottom).

Table 2.3: Numerical Example - Optimal Greenhouse Design Parameters

Π	γ	$\hat{n}$	p_1	p_3	a_1	a_2	ω_1	ω_2
1.35 ± 0.0028	0.26	2.00	12.45	6.64	1.00	1.55	4.76	7.51

These "optimal" design parameters translate into the "optimal" greenhouse illustrated in Figure 2.10. The ellipsoidal components of the generalized greenhouse contour equation are highlighted by the average value between the peaks, and follow a unique version of the shape depicted in Figure 2.2a while the alternating patterns denote the sinusoidal component of

the generalized greenhouse contour equation as depicted in Figure 2.2b. The intended nature of this optimized shape and physical intuition is further discussed in Section 2.4.

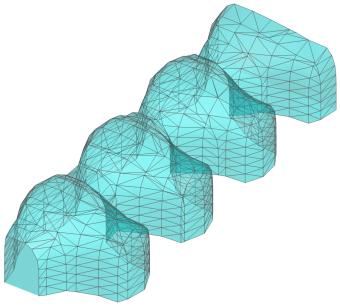

(a) Isometric view of optimized greenhouse design

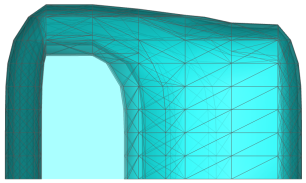

(b) Side view of optimized greenhouse design

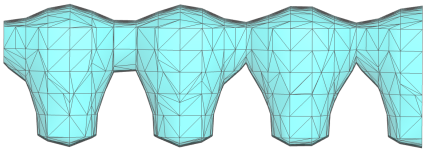

(c) Top view of optimized greenhouse design

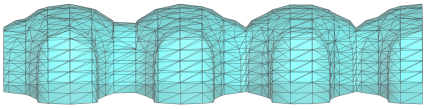

(d) Front view of optimized greenhouse design

Figure 2.10: Detailed views of optimized greenhouse design.

Figure 2.11 outlines key snapshots of the simulation at different times of the day. The times are broken down by every two hours to illustrate significant changes in the angle of incoming light to the greenhouse. The time was chosen to depict collision of the light rays with the greenhouse and ground as well as reflection of the rays simultaneously. In the earlier part of the day, the light rays are observed to become entrapped in reflections within the "sawtooth" convex section of the greenhouse, allowing for increased reflections. The convex portions of the greenhouse on the opposite end of the y axis (see Figure 2.11) are not as large in magnitude, but still provide an entrapment effect for the greenhouse.

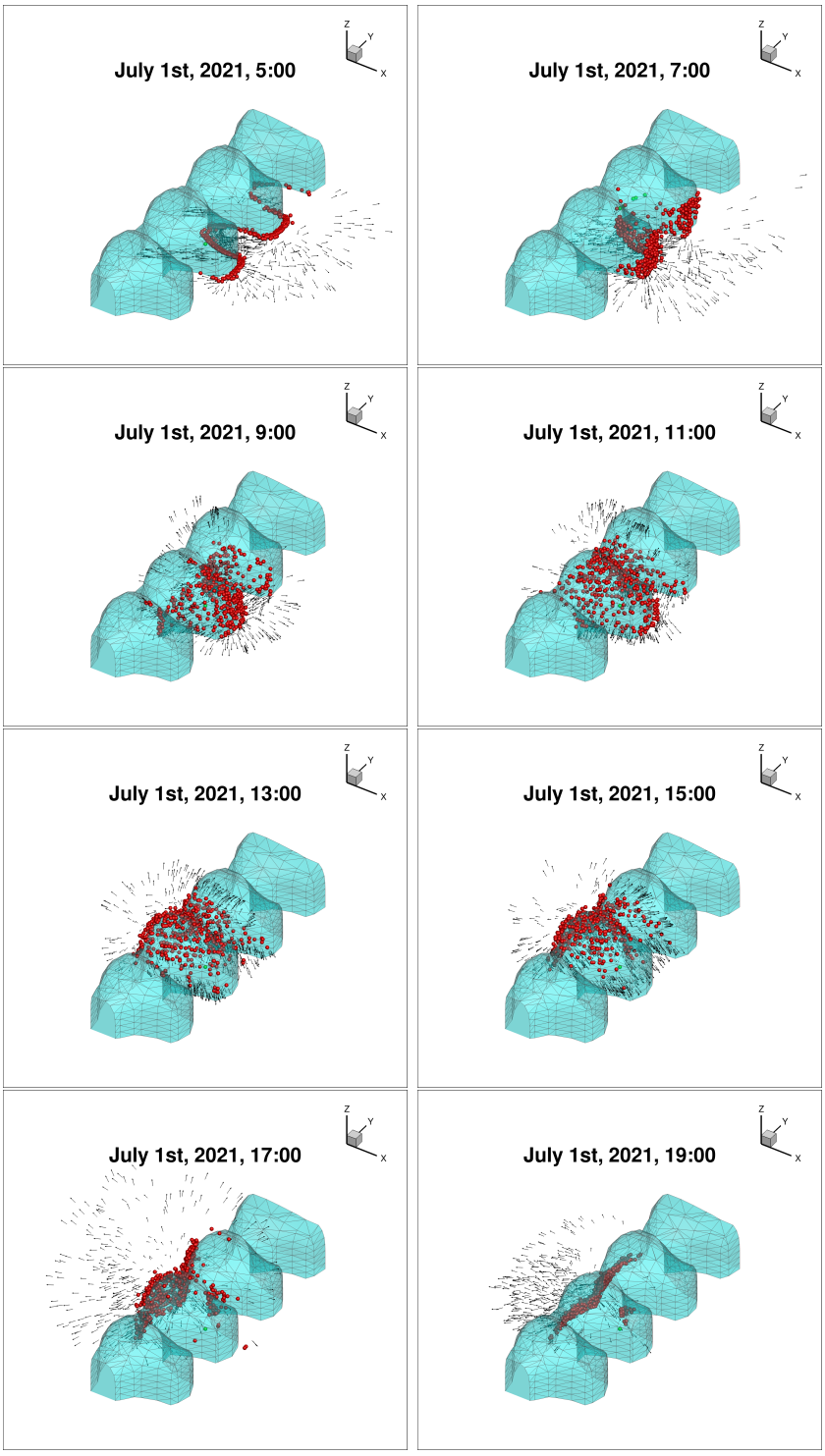

Figure 2.11: Full day simulation of best design.

A closer look at a full simulation is outlined in Figure 2.12 which outlines an incoming flash of light at 12PM on July 1st, 2021. As expected, the light rays enter the domain nearly perpendicular to the ground. The initial impact of the rays leads to pure reflection from the concave portion of the greenhouse. Refraction is not observed until rays come in contact with the convex portion of the greenhouse situated along the x-axis. At this point, there is a period of reflection and refraction within the "sawtooth" until the rays are reflected out or move below the designated power threshold. The simulation is stopped when no active rays are remaining in the domain.

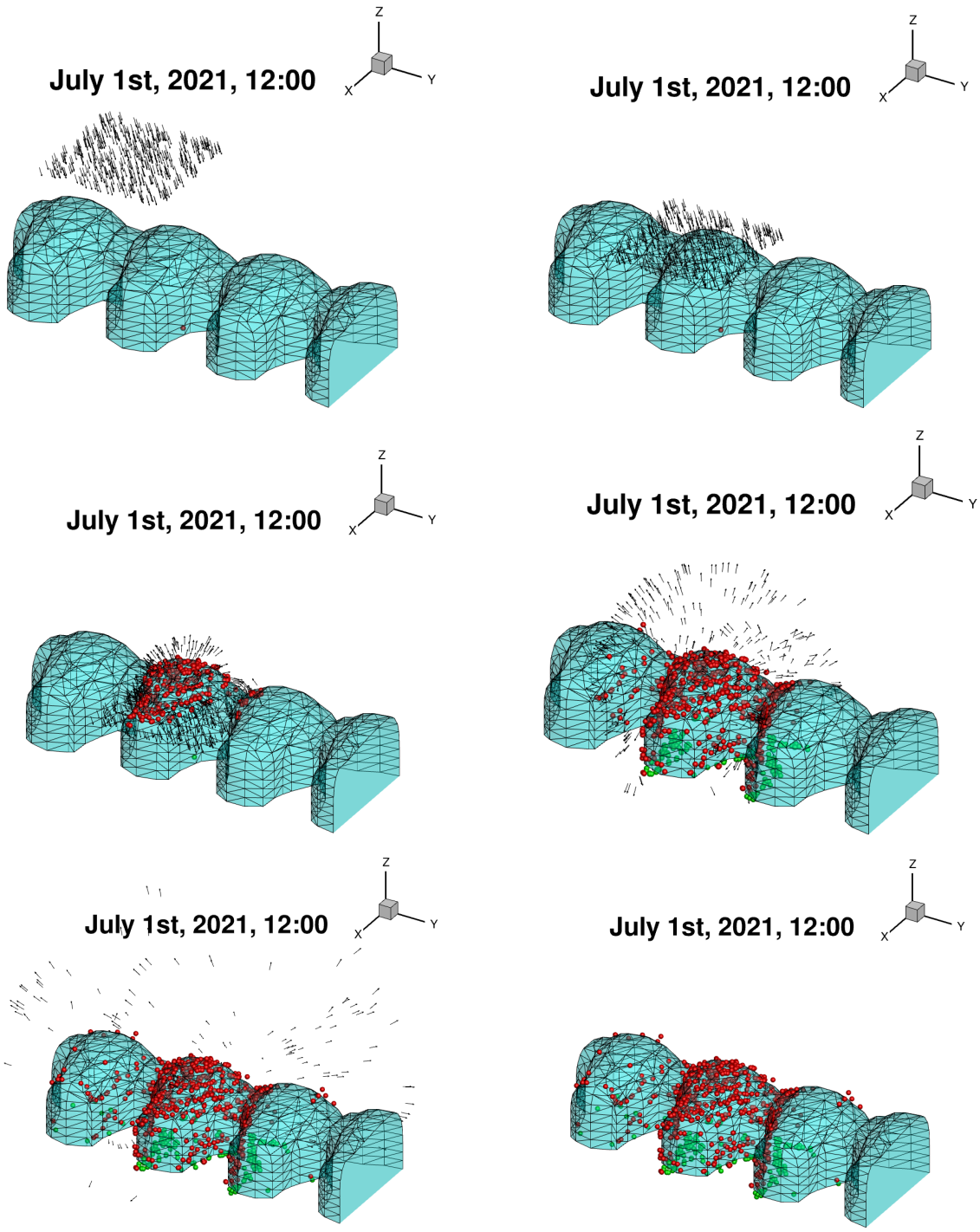

Figure 2.12: Detailed simulation of light flash at 12PM.

2.4 Discussion

The physical intuition of the optimized results can be understood through the design of the cost function. Based on the cost, the optimization scheme worked to maximize the power absorbed by both the solar panels as well as the crops (defined by the ground within the greenhouse). The physical nature of an agrophotovoltaic system deems the majority of the light will come in contact with the greenhouse exterior before refracting into its interior. As such, the algorithm is able to find an optimal path by first designing the greenhouse to generate as much power as possible since it will originally capture the clear sky radiation. It is observed that the optimal design was chosen such that the greenhouse was 74% opaque and thus greenhouse power generation is still prioritized.

This work provides a framework for producing fast, optimized agrophotovoltaic greenhouse designs given a particular location and time of year. Tuning parameters such as opacity to enforce the algorithm to allow a baseline power of light within the greenhouse could allow for a less prioritization of greenhouse power generation. An alternative and potentially more effective strategy for equal prioritization of both power generation and plant growth is to consider wavelength sensitive greenhouses. One such example of these systems is explored by Loik et al. [7]. This agrophotovoltaic system utilizes thin-film solar cells surrounding a greenhouse which work to filter designated wavelengths of light that are solar cell sensitive while refracting wavelengths of light that are crop sensitive for photosynthesis. This not only refines the power sharing strategy outlined in Figures 2.5 and 2.6, but also allows for more efficient processing of light for power generation and photosynthesis.

A wavelength-dependent computational framework also provides merit in addressing the cost reduction limitations of this physical system. These limitations are apparent in the cost evolution shown in Figure 6.4. The cost reduction after 200 generations is limited to roughly a 42.5% improvement from the best design in the initial generation. Ultimately, a wavelength dependent simulation would allow for a more refined cost reduction if the photosynthetically active radiation band of plants is utilized when designing the greenhouse system.

The optimal shape of the greenhouse follows a sawtooth cyclical pattern. The top view shown in Figure 2.10c most clearly illustrates this pattern. The physical intuition of this optimized geometry follows providing convex caves as a means of entrapping the incoming light throughout a single day. These entrapment zones are aligned along the x-axis, consistent with the incoming direction of the radiation. It is also observed that these entrapment zones are biased towards the rays in the first half of the day. This can be attributed to the particular nature of the solar irradiance for this particular day and location. As shown in Figure 2.8, the sun is above the horizon just before 5:00 in the morning, and the sun is below the horizon just after 19:00. As such, the first half of the day simulation includes one more flash of light in comparison to the second half of the day leading to a skewed entrapment of light for the first half of the day. This design, nonetheless, can be utilized as design inspiration for potential transparent greenhouse designs in which the greenhouse is symmetric about the x-axis to account for multiple different seasons within the year.

2.5 Summary

The solar greenhouse model captures the essential physics of ray scattering in a computationally efficient manner. However, the surfaces included in the geometric raytracing framework, the translucent greenhouse structure and the ground is only a starting point and needs improvement if it were to be used as a digital-twin of a real-life agrophovoltaic greenhouse which can be controlled and optimized in real-time. In real greenhouse systems, the plants are grown in different configurations, which include having them uniformly planted on the ground, grown in pots on benches, or stacked vertically to maximize the space utilized. Therefore, the next logical addition to our current modeling framework would be to incorporate racks or towers where the plants could be placed within the greenhouse. These plant racks, combined with soilless precise nutrient delivery systems, are often called hydroponics or aeroponics. The next chapter will improve our solar greenhouse model by adding hydroponic towers to the raytracing simulation as well as improve our optimization algorithm by adding a water pumping power penalty term to the design fitness function.

Chapter 3

Hydroponics and Irrigation

The solar greenhouse structure simulated in Chapter 2 provides a foundation for the capabilities of the raytracing model to accurately evaluate the power distribution within agrophotovoltaic systems. To build on this foundation, we need to consider and model how real-life greenhouses situate the plants inside. While the plants could be planted in the ground similar to an open-field agricultural setup, many greenhouses and indoor farming containers try to maximize the crop production space by stacking the plants vertically. In order to improve our modeling and optimization framework, we will next incorporate the structures plants are placed in within the greenhouse, which are often combined with precise nutrient delivery systems and are called hydroponics or aeroponics.

3.1 Model Overview

Greenhouses employ a variety of different configurations to grow plants. These include: (1) planting the crops in soil similar to an open field and using the greenhouse structure for the sole purpose of climate control and protection from weather elements, (2) placing potted plants on benches in the greenhouse and repotting them as they grow, or (3) stacking them vertically by utilizing the most amount of space possible and precisely delivering nutrients to exposed roots. The third method is called vertical farming and includes the use of aeroponics and hydroponics [18], which we will focus on modeling the latter in terms of solar power absorption of plants and irrigation pump power requirements.

Hydroponics is a method of growing plants in a nutrient rich solution without the need for soil. Depending on the type of crop, this method can be executed via drip irrigation, aeroponics, nutrient film technique, ebb and flow, aquaponics, or deep-water culture. Although physically very different in the method of delivery, most of these techniques share the same fundamentals: a nutrient solution is pumped to the plants via a specialized delivery system and then circulated back to a reservoir where the nutrients are replenished. We refer the reader to [11–15] for a comprehensive description of these techniques. Hydroponic methods use, on average, 10% of the water utilized in traditional farming [16] as nutrients

are delivered directly to the plant roots, minimizing water lost to evaporation. This mode of growing plants can be easily automated and, combined with the fact that the lack of soil protects against pests, these systems make it easier to cater to the unique physiological needs of the plants while eliminating the need for pesticides and other chemicals. These systems, however, have high start-up costs [17] and thus present a dire need for high operational efficiency to recoup these costs.

In this chapter, we will follow closely the digital twin framework used for the initial solar greenhouse model, where we will simulate different greenhouse geometries, as well as different hydroponic tower configurations, including the tower shape, sizing, refractive index, and proximity of towers to each other. The resulting solar power distribution within the system, namely the solar panel and plant energy absorption, and the irrigation pump power requirements will determine the "fitness" of the agrophotovoltaic design.

3.2 Hydroponics Model

Creating Hydroponic Tower Geometries

We will employ the 3D-ellipsoidal equation previously used in generating the greenhouse shape without the sinusoidal terms to create the hydroponic towers described by a surface function, $F(x_1, x_2, x_3)$:

$$F(x_1, x_2, x_3) = \left|\frac{x_1 - x_{1o}}{R_1}\right|^{p_1} + \left|\frac{x_2 - x_{2o}}{R_2}\right|^{p_2} + \left|\frac{x_3 - x_{3o}}{R_3}\right|^{p_3} \leq 1 \tag{3.1}$$

where (R_1, R_2, R_3) are the generalized radii, (p_1, p_2, p_3) are the exponents of the generalized ellipsoid, and (x_{1o}, x_{2o}, x_{3o}) are the center location of the ellipsoid. In this context, the center location will be determined by the design parameters that dictate the tower spacing within the greenhouse. While nearly all the scaling factors in this equation will be the hydroponics design parameters, R_3, the generalized radii in x_3 direction will be constricted by the height of the greenhouse structure at a given hydroponic tower location. Since the greenhouse scale is arbitrary, meaning is not part of the design optimization and set as constant in the model described in Section 2, the hydroponic tower spacing parameter is in terms of the fraction of the available greenhouse space on the ground level. The variety of hydroponic tower shapes and spacing that can be achieved is visualized in Figure 3.1.

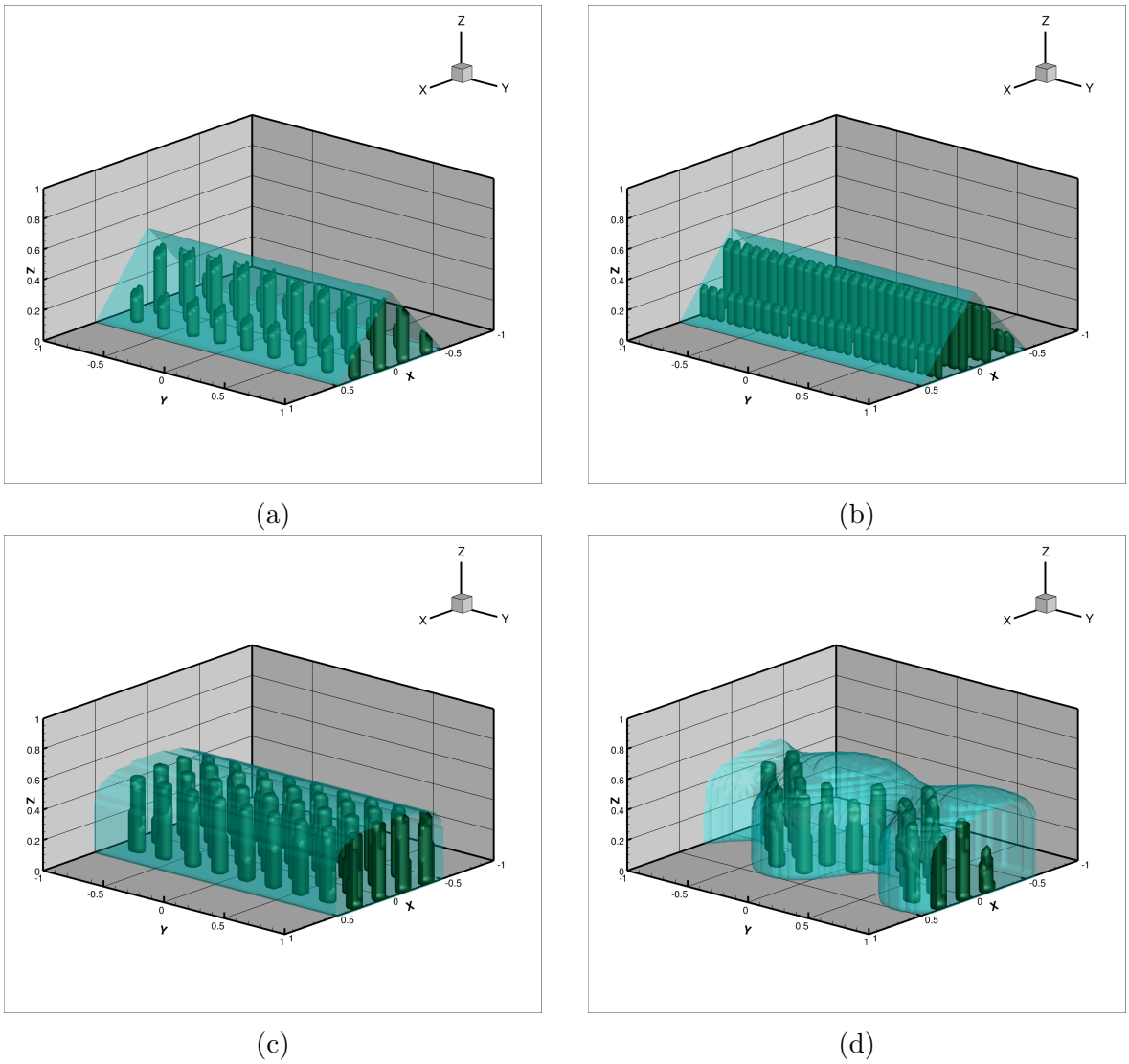

Figure 3.1: Example hydroponic greenhouse configurations created by greenhouse shape parameters $(p_{g,1}, p_{g,3}, a, b, w_1, w_2)$ and hydroponic shape $(p_{h,1}, p_{h,2}, p_{h,3})$ and size $(R_{h,1}, R_{h,2})$ parameters and spacing $(\Delta x_1, \Delta x_2)$.

Raytracing Algorithm

The details of the raytracing algorithm is identical to the greenhouse raytracing model introduced in Section 2, where rays are propagated in time using a Forward Euler time-stepping scheme. The ray-surface interactions are simulated using a collision check against the ellipsoidal elements (i.e. greenhouse structure and each hydroponic tower) and the ground. Once a hit is detected, the ray is split in the case of it hitting the translucent greenhouse structure

due to refraction and reflection or is only reflected if it hits the hydroponic towers or the ground.

The surface power absorption and ray power retention are calculated at each ray-surface interaction throughout the simulation. The power absorbed by the surface can be calculated by

$$P_{abs} = (1 - \mathcal{IR})P_r \tag{3.2}$$

The remaining power in the ray is calculated as follows:

$$P_{ref} = \mathcal{IR}P_r \tag{3.3}$$

The ray is tracked in the system as long as:

- the ray is within the system domain limits,
- its power is above the specified power threshold P_{min}.

Hydroponic Pump Power Requirements

The design fitness of the solar greenhouse so has so far only evaluated the power absorption of the solar panels situated on the greenhouse structure and the plants that were previously situated on the ground. With the addition of hydroponics to the model, we now need to assess the "cost" we will incur by placing hydroponic towers that vary in number, size, and shape. For example, this cost could be in terms of reduced solar power absorption by plants if the hydroponic towers placed are too many, too big, or have suboptimal shapes that block sunlight at given angles. While the power absorption penalty of the hydroponic towers will be evaluated through the raytracing model, another important aspect to assess hydroponics performance will be the irrigation pump power requirements due to the size and number of the hydroponic towers in the agrophotovoltaic system design.

To be able to calculate the pumping power, we will go through the following steps of calculations:

1. Calculate greenhouse model scale given common greenhouse sizing [24] of (L: 96 ft x W: 30 ft) and model size of (L: 1 u x W: 0.5 u). Since the length of the greenhouse in the model is not constrained and can be expanded, we will use the width in calculating the scaling factor:
$$r_{scale} = \frac{0.5}{30} = \frac{1}{60} \tag{3.4}$$
2. Choose hydroponics plant spacing per row (d_h) and between rows (d_v). In this study, we will choose the values arbitrarily while keeping it close to recommendations for real-life applications [25]:
$$d_h = 1 \text{ ft}, \quad d_v = 2 \text{ ft} \tag{3.5}$$

3. Calculate tower radius (R_{avg}) in $e_1 - e_2$ plane given ellipsoidal radii ($R_{h,1}$ and $R_{h,2}$):

$$R_{avg} = \frac{R_{h,1} + R_{h,2}}{2} \tag{3.6}$$

4. Calculate number of plants per rack (N_{ppr}) and the number of racks (N_{rack}) using the tower circumference and height, respectively:

$$N_{ppr} = \frac{2\pi R_{avg}}{d_h} \frac{1}{r_{scale}} \tag{3.7}$$

$$N_{rack} = \frac{h_{tower}}{d_v} \frac{1}{r_{scale}} \tag{3.8}$$

5. Calculate the total number of plants housed on a given tower:

$$N_{ptot} = (N_{ppr})(N_{rack}) \tag{3.9}$$

6. Calculate total water reservoir volume needed to irrigate the plants in the tower. This will depend on the hydroponic system used. We will use nutrient film technique (NFT) for our numerical example. Nutrient film technique system uses a slanted tray to move the nutrient solution from the top of the tray and use gravity to direct it to the plants at lower levels [26]. The rule of thumb described in many sources on hydroponic farming is that water needed per plant is: 1) 1/2 gal for small, 2) 1-1.5 gal for medium, and 3) 2-2.5 gal for large plants [27].

   Then, choosing 1.5 gal per plant for our calculations, the water reservoir required per tower is:

$$V_{water} = (1.5)N_{ptot} \tag{3.10}$$

7. Next, we will choose the flow rate for our system, in terms of the circulation time of the solution. This will be specific to the hydroponic application and can be adjusted by the user using this framework. We will use an arbitrary 2-hour cycle for the system, which then gives us the gallons per hour rate of flow:

$$\text{GPH} = \frac{V_{water}}{2} \tag{3.11}$$

8. Finally, we will employ a simple power pumping calculation dependent on the height of the hydroponic tower:

$$P_{tower} = (\text{flow rate})(\rho)(g)(h_{tower}) \tag{3.12}$$

9. Repeat Steps 1-8 for every hydroponic tower within the greenhouse to get total power needed to pump nutrients to the plants in the hydroponic system:

$$P_{pump} = (N_{tower})(P_{tower}) \tag{3.13}$$

The hydroponic pumping power required for a given greenhouse configuration will ultimately depend on the size and shape of the hydroponics, which are also tied to the greenhouse shape. Calculating the pumping power will allow us to include it in the design fitness function to better assess the power generation and consumption of our agrophotovoltaic system.

Process Optimization

The "design string" for this process contains all 17 controllable constants:

$$\mathbf{\Lambda}^i \equiv \{\Lambda_1^i, ..., \Lambda_N^i\} \equiv \{\gamma, \hat{n}_s, p_1, p_3, a_1, a_2, \omega_1, \omega_2, , \Delta x_1, \Delta x_2, p_{h,1}, p_{h,2}, p_{h,3}, R_{h,1}, R_{h,2}, \hat{n}_h, \hat{n}_g\} \tag{3.14}$$

where γ is the transmissibility of the solar panels, $\hat{n}_s$ is the refractive index of the solar panels, $\hat{n}_h$ is the refractive index of the hydroponic towers, $\hat{n}_g$ is the refractive index of the ground. The remaining design parameters relate to the shape parameters of the greenhouse and the hydroponic towers and the spacing of the said towers. These parameters can be controlled within user-specified bounds. All system parameters used in this simulation are displayed within Table 6.3.

A good set of characteristic parameters of our greenhouse design will allow for maximum absorptivity of the solar panels (for energy production) as well as absorbed light by the ground (for plant growth) and minimize the pumping power required to deliver nutrients and water to the plants situated in the hydroponic towers. As mentioned in Section 2, the necessary next step in improving the design cost function definition is to connect the plant solar energy absorption to crop performance metrics such as crop yield and water and light use efficiencies. This will ensure the plant power absorption is penalized when the crops are overexposed to sunlight during the day in the same way it will be penalized when there isn't enough sunlight. The details regarding improving the cost function will be discussed in extensions of this dissertation, in Section 6. Going back to the current hydroponic greenhouse model, given the objective of maximizing power absorption by the panels and plants, as well as minimizing the pumping power, we construct the following cost function,

$$\Pi = w_1 \left| \frac{P_o - P_{elec}}{P_o} \right| + w_2 \left| \frac{P_o - P_{photosynth}}{P_o} \right| + w_3 \frac{P_{pump} - P_{max}}{N_{tower} P_{max}} \tag{3.15}$$

where the weights are chosen to be $w_1 = 2$, $w_2 = 3$, and $w_3 = 1$. The weights can be assigned arbitrarily by the user as long as they are positive and reflect the relative importance of each objective term. The choice of weights in this work's numerical example is chosen to prioritize designs in which the hydroponic plant power absorption is maximized.

Note that all terms in the cost function are non-dimensional. In addition, the pumping power penalty term is divided by the number of towers within that design to avoid penalizing designs that include more towers and evaluate the cost to pump per tower basis. It is also normalized using the maximum solar power density achieved during the day simulation, P_{max}.

Given the cost function, the system can be optimized using the genetic algorithm described in Section 2. The genetic algorithm parameters and design parameter search bounds used in this work are included in Table 3.2.

3.3 Results and Discussion

A numerical example is used to demonstrate the capabilities of the hydroponic greenhouse digital-twin framework. Similar to the previous solar greenhouse model described in Section 2, the system is pulsed at hourly intervals with given clear sky radiation values, altitude and azimuth angles for July 1st, 2021 in Berkeley, California, using *pysolar* Python package [22]. In addition to the design parameters of the previous solar greenhouse model, we expect the genomic optimizer to find the optimal hydroponic design parameters that will maximize the power absorption of the panels, and plants, and minimize the hydroponic pumping power required for the system. The system parameters chosen for this numerical example are given in 3.1.

Table 3.1: Numerical Example - Greenhouse and Hydroponics System Parameters

Symbol	Type	Units	Value	Description
N_r	scalar	none	500	Number of light rays
c	scalar	m/s	3×10^8	Speed of light
t	scalar	m	0.1	Solar panel thickness
$[R_1, R_2, R_3]$	scalar	none	$[0.5, 5, 0.5]$	Generalized radii
p_2	scalar	none	20	Geometric exponent
r_{scale}	scalar	none	1/60	Greenhouse model scale
d_h	scalar	ft	1	plant spacing per row
d_v	scalar	ft	2	plant rack spacing
V_{wpp}	scalar	gal	1.5	water needed per plant (medium-sized)
ρ_w	scalar	kgm^{-3}	1000	water density

Table 3.2: Numerical Example - Genomic Optimization Parameters

Symbol	Type	Units	Value	Description
parents	scalar	none	6	Surviving strings for breeding
S	scalar	none	20	Designs per generation
G	scalar	none	150	Total generations
$[\gamma^-, \gamma^+]$	scalar	none	[0.25,1]	Solar panel transmissibility
$[\hat{n_s}^-, \hat{n_s}^+]$	scalar	none	[2,5]	Solar panel refractive index
$[\hat{n_h}^-, \hat{n_h}^+]$	scalar	none	[2,5]	Hydroponics refractive index
$[\hat{n_g}^-, \hat{n_g}^+]$	scalar	none	[2,5]	Ground refractive index
$[p^-_{g,1\ or\ 3}, p^+_{g,1\ or\ 3}]$	scalar	none	$[1, 20]$	Greenhouse geometric exponents
$[a^-_{1\ or\ 2}, a^+_{1\ or\ 2}]$	scalar	none	$[0, 1.75]$	Sinusoid amplitudes
$[\omega^-_{1\ or\ 2}, \omega^+_{1\ or\ 2}]$	scalar	none	$[0, 10]$	Sinusoid frequencies
$[\Delta x^-_{1\ or\ 2}, \Delta x^+_{1\ or\ 2}]$	scalar	none	$[0.10, 0.50]$	Tower spacing per axis
$[p^-_{h,1\ or\ 2\ or\ 3}, p^+_{j,1\ or\ 2\ or\ 3}]$	scalar	none	$[1, 20]$	Hydroponics geometric exponents
$[R^-_{h,1\ or\ 2}, R^+_{h,1\ or\ 2}]$	scalar	none	$[1, 20]$	Hydroponics generalized radii
w_1	scalar	none	2	Solar panel power penalty weight
w_2	scalar	none	3	Plant power penalty weight
w_3	scalar	none	1	Pump power penalty weight
P_{max}	scalar	Wm^{-2}	873.9	Maximum solar power density

Optimization results for the numerical example is given in Figure 3.2 for the first 150 generations. We clearly see an approximate 12% improvement of the system after the optimization run. While the improvement can be considered minor, a different set of system parameters and user defined objective function weights can drastically change the "optimal" design, as well as the percent reduction of the best design fitness across generations. The shortcomings and the proposed extensions to the model, as well as the optimization function, will be further discussed in the next section.

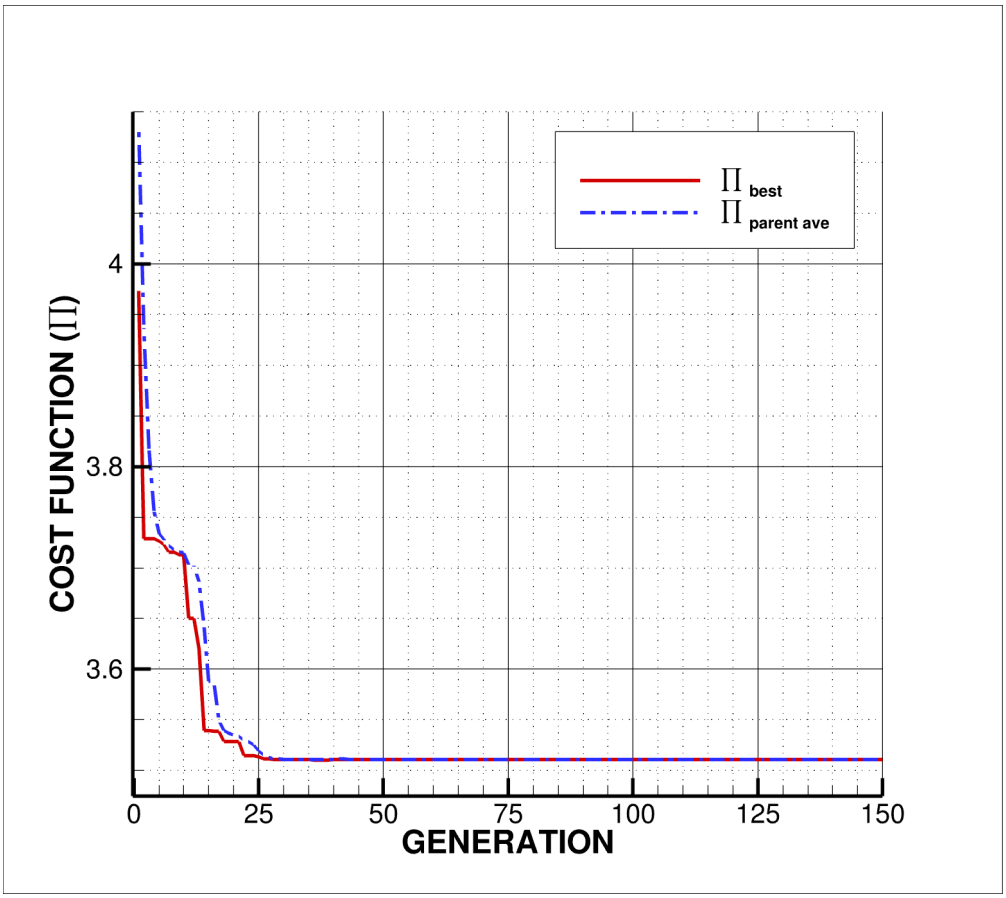

Figure 3.2: Evolution of system design costs (parent average, and best design cost).

Table 3.3: Numerical Example - Optimal Hydroponic Greenhouse Design Parameters

$\mathbf{\Pi}$	γ	n_s	$p_{g,1}$	$p_{g,3}$	a
3.51	0.272	2.79	5.66	11.3	1.13
b	ω_1	ω_2	Δx_1	Δx_2	$p_{h,1}$
0.096	3.53	4.80	0.167	0.182	5.35
$p_{h,2}$	$p_{h,3}$	$R_{h,1}$	$R_{h,2}$	n_h	n_g
7.04	2.638	0.032	0.045	3.23	50.8

The optimal agrophotovoltaic system design parameters can be seen in Table 3.3 and is also illustrated in Figure 3.3. We can see that the greenhouse shape follows the progression of the solar angles and maximizes the incoming radiation into the interior of the greenhouse,

as seen in Figure 3.5 and 3.6. In addition, the hydroponic towers are situated to maximize power absorption of the plants due to the nonzero azimuth angle of the sun.

The results shown demonstrate a framework to model and optimize a hydroponic agrophovoltaic system. While the intricacies of indoor farming and solar power generation expand beyond the capabilities of the current model described in this study, this model serves as a foundation for a fast simulation that can utilize GPU parallelization techniques and be used in genomic optimization. Further additions to this model can be made by coupling the raytracing algorithm with crop modeling, heat modeling, as well as ventilation systems, and air flow modeling.

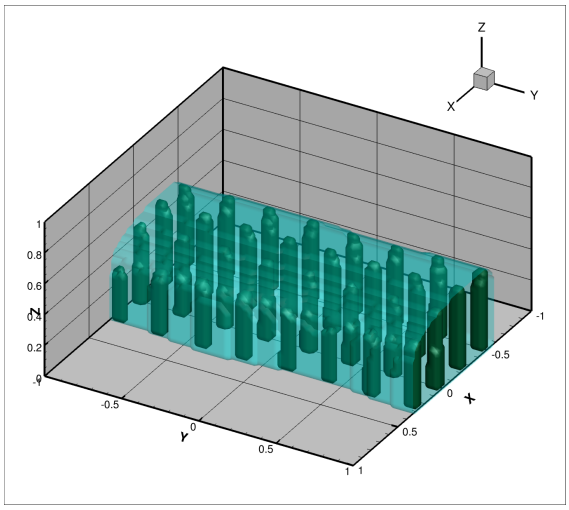

(a) Isometric view of optimized greenhouse.

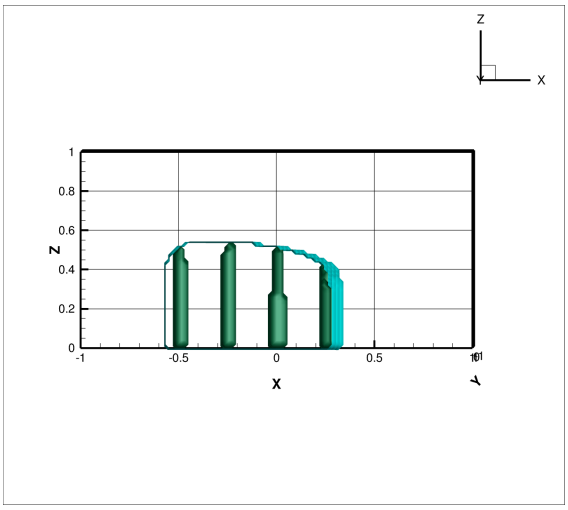

(b) Side view of optimized greenhouse.

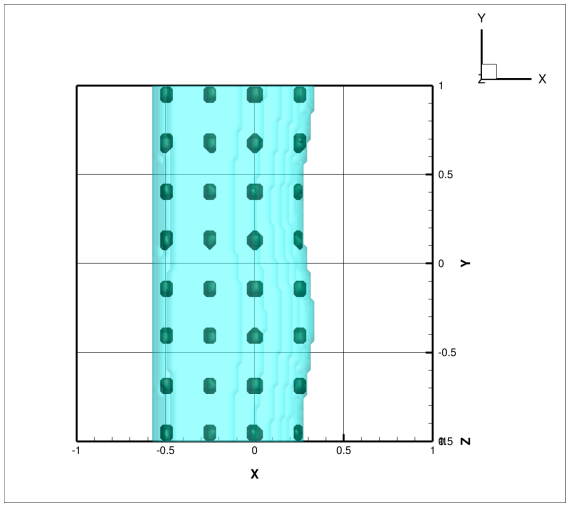

(c) Top view of optimized greenhouse.

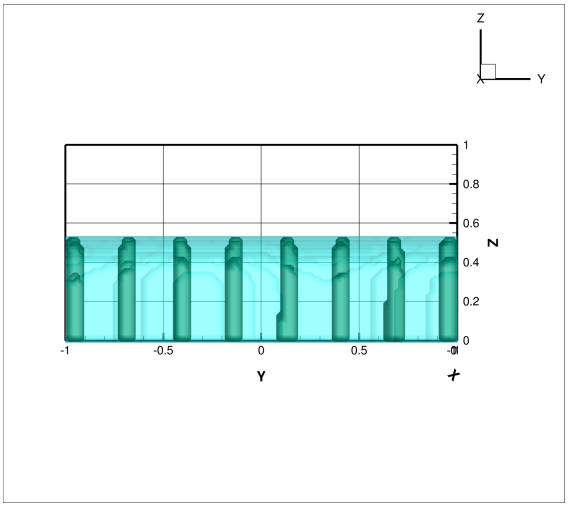

(d) Front view of optimized greenhouse.

Figure 3.3: Detailed views of optimized greenhouse design.

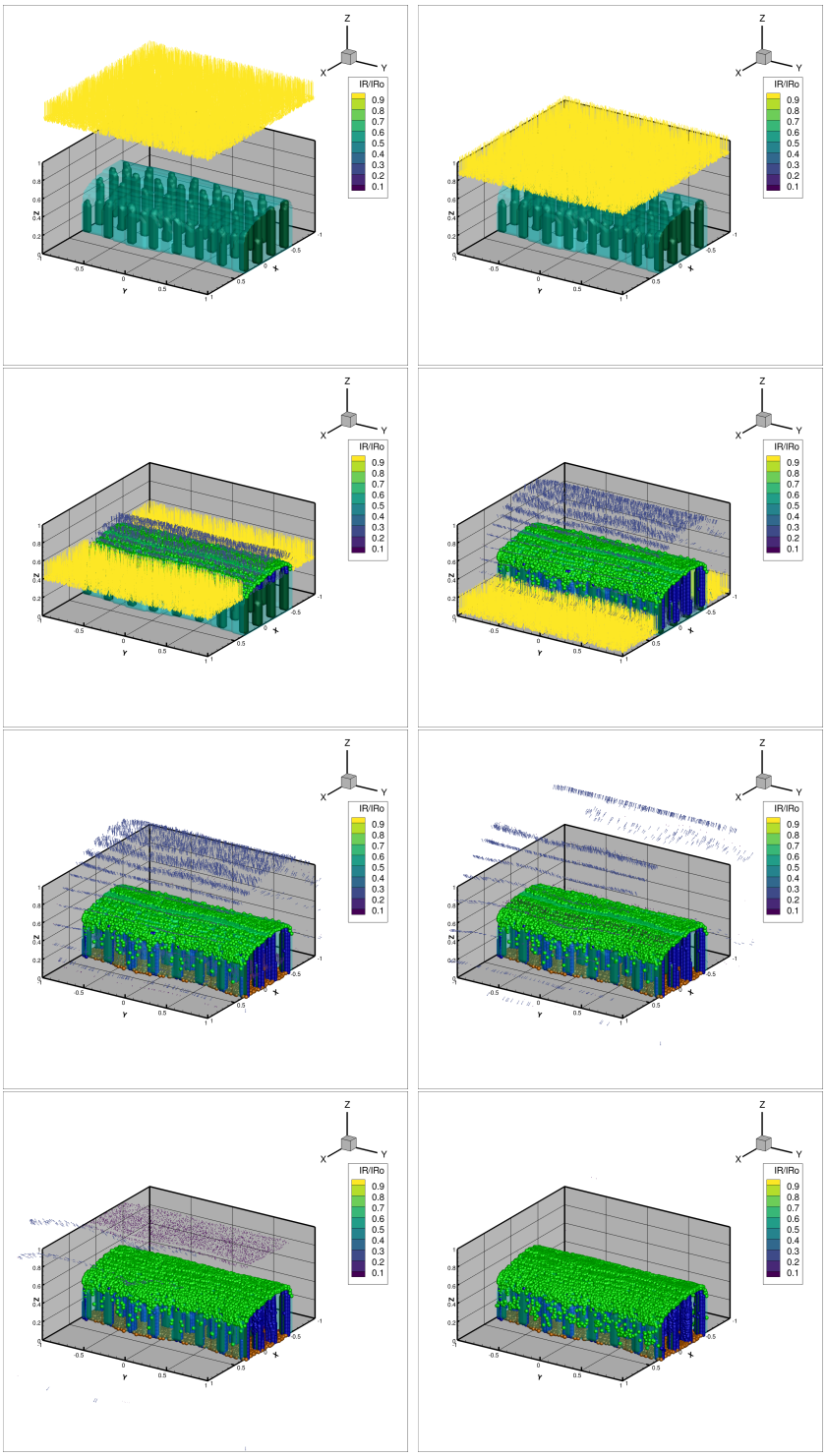

Figure 3.4: Detailed simulation of a light flash generated perpendicular to the ground.

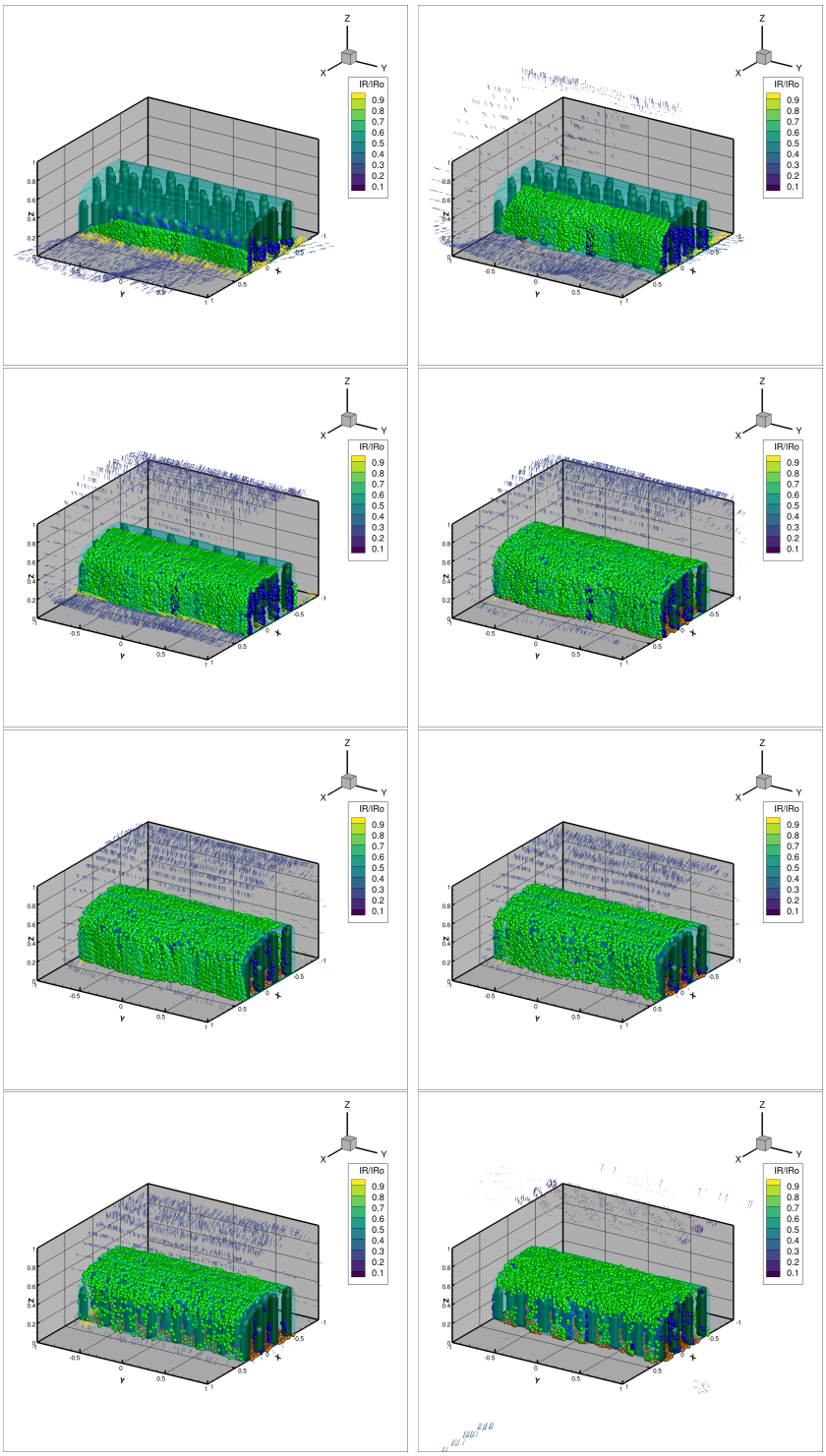

Figure 3.5: Full day simulation of best design. Moment rays hit the greenhouse is visualized for hours of the day (6AM-1PM).

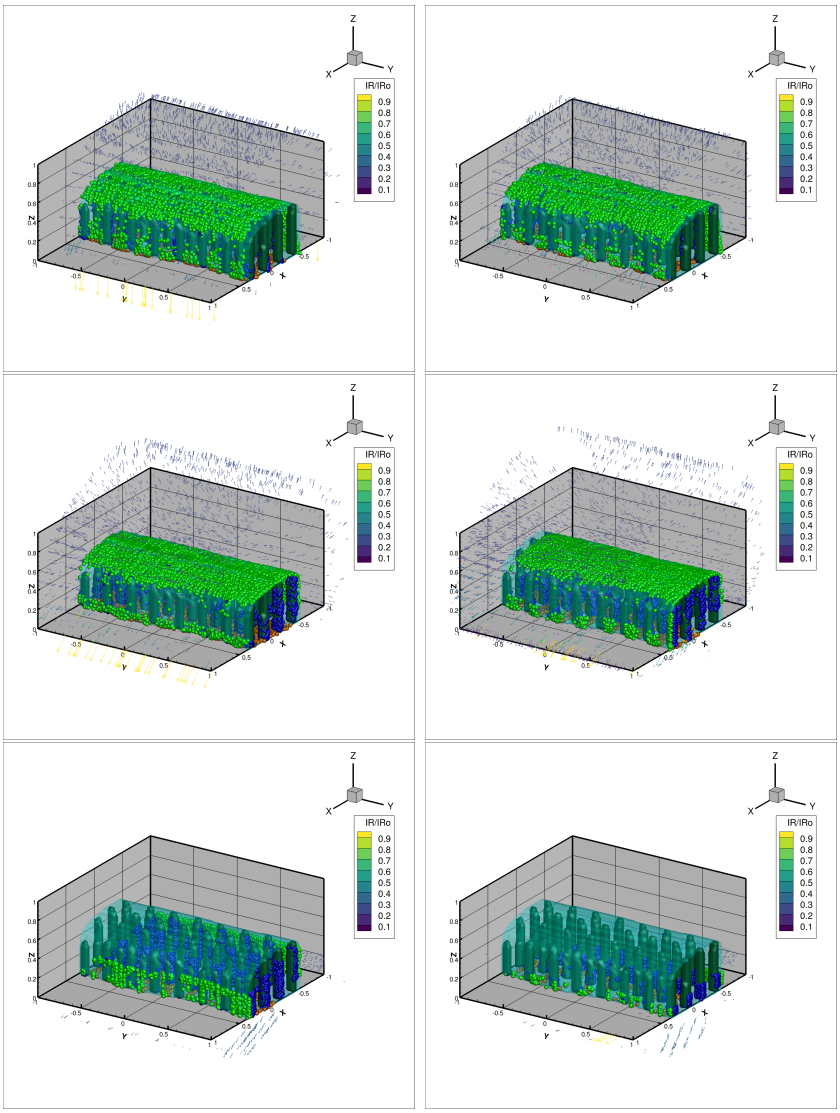

Figure 3.6: Full day simulation of best design. Moment rays hit the greenhouse is visualized for hours of the day (2PM-7PM).

3.4 Summary

Agrophotovoltaic systems offer agricultural production and power generation to exist in the same space. While the efficacy of these systems has been experimentally proven, there is a significant avenue yet to be explored using computational methods to model and optimize such systems. To drive innovation and utilize state-of-art food systems, we introduced a digital-twin of a greenhouse agrophotovoltaic system with hydroponics by modeling the optical properties of the system and the power requirements of the hydroponics. This frame-

work can easily be adapted to include other multiphysics models such as crop, heat, and ventilation models. The upgraded framework can be used as an invaluable tool to optimize real-life systems and reduce the financial cost of experimentally testing system designs.

It is important to note that next-generation food production systems span a variety of different configurations including open-field APVs, solar greenhouses, and indoor farming pods. While the hydroponic solar greenhouse model developed is a great tool to simulate and optimize an agrophotovoltaic greenhouse system, we need to look at other types of next-gen food systems. The optical modeling approach developed so far can also be applied to another popular crop production system: indoor farming pods. Indoor farming is a type of controlled environment agriculture (CEA) that allows the precise control of nutrients, climate, and lighting of food production. Since one of the most important factors that drive crop growth is radiation, the next step of our modeling and optimization framework for next-generation food systems is the optical modeling of indoor farming pods.

Chapter 4

Optical Design of Pod-Based Indoor Farming Systems

In addition to the increase in the popularity of agrophotovoltaic greenhouses, AI in food systems is moving towards aeroponic or hydroponic farming in indoor spaces, where light, nutrients, and water is precisely controlled and artificially supplied. As the lighting inside the indoor farming pod is highly controlled, there is a compelling reason to model and optimize the light scattering and absorption to improve crop growth efficiency. Therefore, the next step of our next-generation food system modeling and optimization framework is the optical simulation of the LED lighting inside an indoor farming pod using the previously developed raytracing approach [28].

4.1 Background Information

Vertical indoor farming

Indoor farming is a promising mode of next-generation agriculture, enabling year-round cultivation of produce, independent of local climate conditions. Indoor farms can be built in urban areas, making fresh, local produce available at lower prices to consumers, thanks to reduced transportation and irrigation costs. They also offer increased yields and reduced pesticide usage as, with soil-free hydroponics and a highly controlled growth environment, fewer plants are lost to pests and disease. In the face of a changing climate and "food deserts" prevalent in both urban and rural settings, indoor farming offers a sustainable solution to scarcity of fresh produce.

The concept of indoor farming has been explored for millennia. The concept of shielding plants from vacillating weather conditions by growing plants inside a greenhouse was first implemented by agrarian communities in 30 CE [29]. As time and technology progressed, full control over ventilation, air flow, growth medium, and light exposure became feasible. One of the first fully-fledged controlled environment research facilities began operation at North

Carolina State University in 1968 [30]. Recent developments in the semiconductor industry have made it cost effective for light-emitting diodes (LEDs), which can provide specific wavelengths of light for photosynthesis, to supplant broad-spectrum sunlight. This has given rise to "plant factories" [31] and indoor farming "pods" [32] (Figure 4.1): warehouses and shipping containers outfitted with LEDs, hydroponics, cameras and advanced sensors which are nominally more efficient than traditional farms and greenhouses.

Shade is not a concern for indoor farms as, with optimal optical design, all plants can receive the requisite light for photosynthesis. As such, many indoor farms will organize hydroponically grown plants in either 1) vertically stacked shelves or 2) adjacent panels hanging from the ceiling [33]. This dense packing of plants facilitates more growth on less land. To put this into perspective, a 30-story vertical indoor farm with a 5-acre base could produce a crop yield equivalent to 2400 acres of a traditional farm [34].

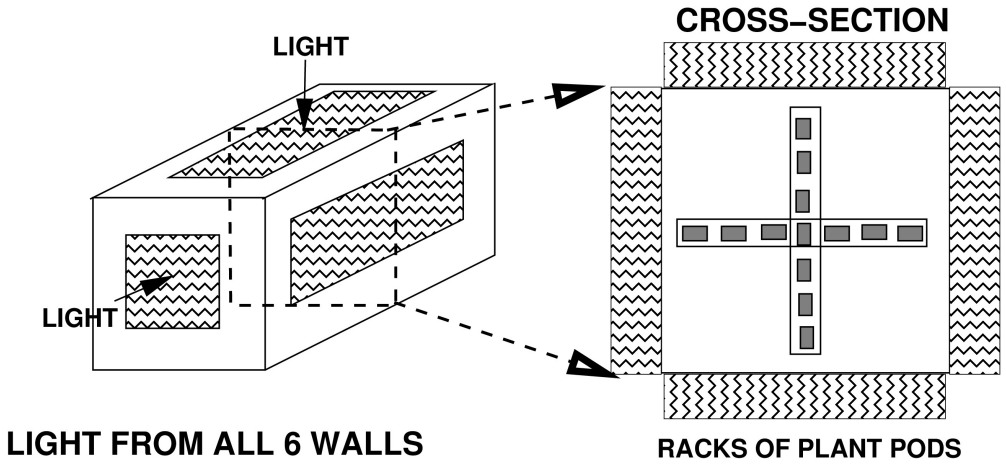

Figure 4.1: A general schematic of an indoor container farming pod.

LEDs: Light-emitting diodes

Different plants require different wavelengths of light for optimal photosynthesis and optimal growth of features such as stem length and leaf thickness [35]. LEDs are perfectly suited to supply plants with the specific, optimal combinations of colors of light they need, because LEDs emit a narrow band of wavelengths depending on the bandgap of their constituent semiconductor material. Thus, indoor pod farms with "walls" of LED light strips reduce energy waste by maximizing the amount of power absorbed by the plants and minimizing the power lost to excess heat. Beams of light supplied by LEDs can be collimated by the addition of optical lenses, further reducing energy lost to non-plant targets and reducing the distance between the plants and LEDs. Additionally, exponential development in the semiconductor industry over the past three decades has made LEDs smaller, faster-actuating, more efficient,

and more durable than traditional incandescent light sources, rendering LEDs economically viable for indoor farming applications.

Digital-twins and optimization

The practice of vertical indoor farming in shipping container "pods," enabled by LED light sources and hydroponic nutrient sources, is still nascent and little work has been done to quickly and efficiently model and optimize such systems. A digital-twin of an indoor pod farm can be safely and cheaply manipulated without jeopardizing the system or the plants' well-being, making it an exceedingly quick, inexpensive, and useful approach for identifying optimal operational parameters.

The indoor farming pod is a complex system with a multitude of physical phenomena including air flow, light propagation, and energy transfer. Several digital-twin frameworks have been developed to capture the physics of light propagation in greenhouse, agrophotovoltaic, and food decontamination applications using ray tracing techniques [21, 36] and to capture and optimize the physics of energy flow [37–39] and air flow [40, 41]. Ray tracing techniques decompose light into rays whose interactions with surfaces are quickly geometrically traced, facilitating fast computation of a large number of interactions between rays and surfaces and optimization of the surface shape for maximum absorption/reflection.

Digital-twins have been scarcely employed in optimizing agricultural systems [42–44], and they are even more rarely implemented in indoor farming pods. Two such implementations were carried out by Randolph et al. [45] and Sambor et al. [46] to optimize the energy consumption of an off-grid indoor farming pod to determine optimal operation time for each component of the system. These implementations, however, do not allow for manipulation of the orientation and/or shape of the system's components for maximum operational efficiency. In [47], computational fluid dynamics (CFD) methods were utilized to model the air flow inside an indoor farming pod, but such methods have a prohibitively high computational cost, especially when running various configurations and performing optimization. Thus, an easily manipulated, computationally inexpensive model that accurately captures the system's physics is desired.

Objectives

Over the past few years, around the world, many indoor farming companies have been proving that indoor farming is a viable mode of next-generation farming, but the systems remain energy-intensive, and little analysis has been performed to assess system efficiency. To optimize these systems and drive innovative solutions, this work develops a flexible digital-twin for the optical design of sustainable, small-scale indoor farming "pods," containing vertically grown plants with energy supplied by carefully controlled LEDs. Flow of LED power is rapidly computed with a reduced order model of Maxwell's equations based on high-frequency decomposition of the LED irradiance into multiple rays. These rays are then propagated forward in time to track their reflections and ultimate absorption. We simulate

thousands of source-system configurations, varying the emission characteristics of the LED "walls" and optimizing for maximal power absorption by the plant "targets."

The digital-twin consists of

- A model for the LED optics and tracking of power flow,
- A model for the absorption of the optical power by the pod components, and
- A genomic optimization of LED configuration and emission characteristics.

The digital-twin and optimization framework described in this work can be quickly and easily run on a laptop, making it more accessible than computationally-intensive alternatives. This work is motivated by the possibility that indoor farming researchers and practitioners will tailor this simulation paradigm to their specific system's needs.

4.2 Indoor Farming Model

Pod farm, plant, and LED geometries

We model an indoor pod farm as an enclosed rectangular box defined by "wall cutoff" values $(x_{w1\pm}, x_{w2\pm}, x_{w3\pm})$ which can be adjusted to simulate any pod size. Each wall has an array of LEDs whose beam spread, power, and geometric configuration (limited to a rectangle within the wall plane) can be configured for optimal performance. We can label the six walls by their inward surface normal in the standard Euclidean basis $(\boldsymbol{e}_1, \boldsymbol{e}_2, \boldsymbol{e}_3)$. Using Cartesian coordinates (x_1, x_2, x_3), we designate the center of the pod as the origin. Plants racks can then exist in planes parallel to $x_1 = 0$, $x_2 = 0$, and/or $x_3 = 0$. Example plant rack configurations are shown in Figure 4.2.

Once rays are emitted from one of the six walls of the pod, they are propagated forward in time. In each time step, we check to see if the ray has hit a wall or a plant or will simply continue propagating as in the previous time step. Once a ray-surface interaction happens, we determine the power absorbed by either the wall or plant, the residual power in the ray, and reflection normal for the ray.

Plant targets are modeled as generalized ellipsoids. We define the surface of plant i with

$$F_i(x_1, x_2, x_3) = \left|\frac{x_1 - x_{1i}}{R_1}\right|^{p_1} + \left|\frac{x_2 - x_{2i}}{R_2}\right|^{p_2} + \left|\frac{x_3 - x_{3i}}{R_3}\right|^{p_3} \leq 1 \tag{4.1}$$

where (R_1, R_2, R_3) are the generalized radii, (p_1, p_2, p_3) are the generalized exponents, and (x_{1i}, x_{2i}, x_{3i}) define the center of the plant.

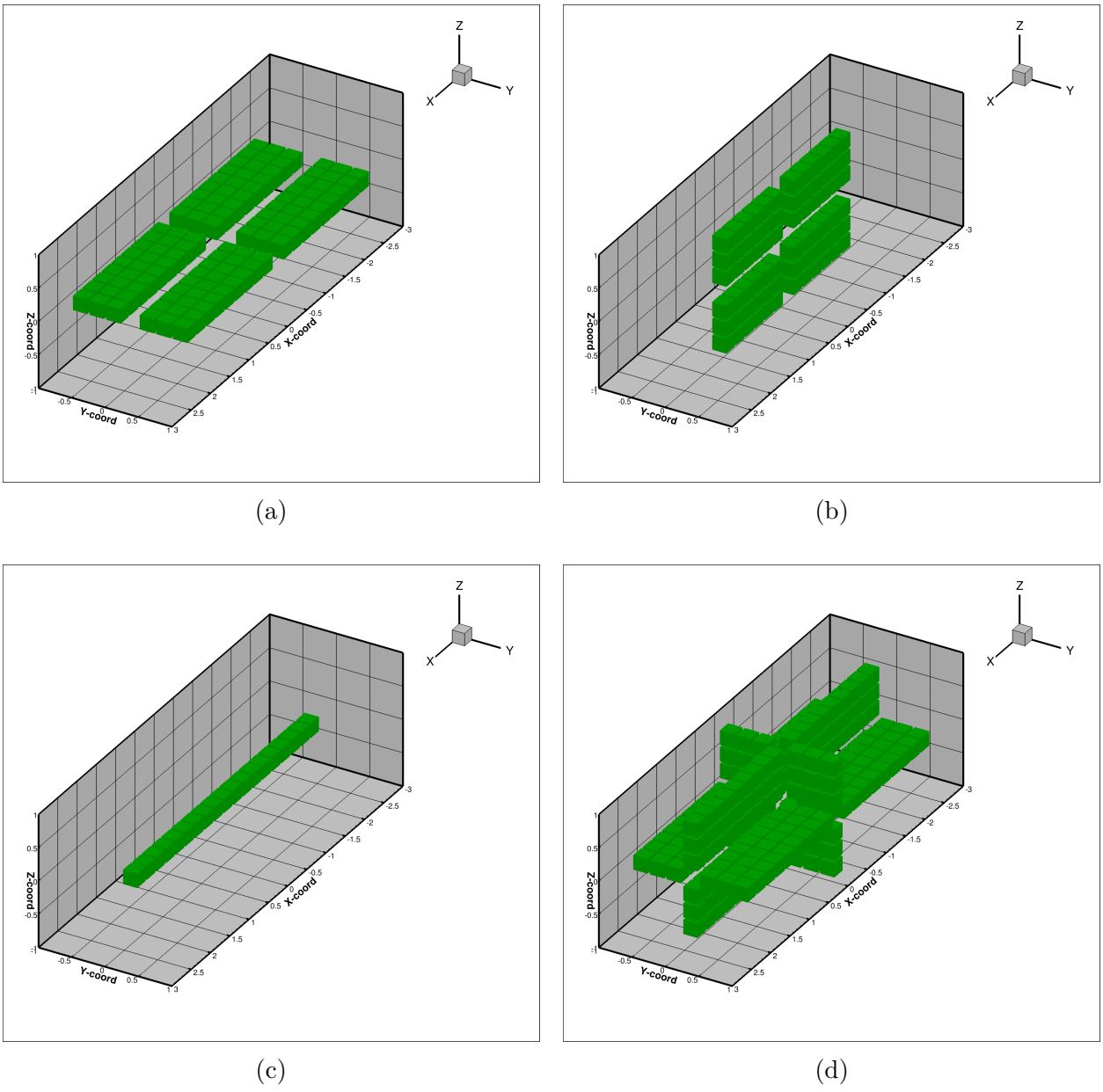

(a) (b)

(c) (d)

Figure 4.2: Example pod configurations for (a) rack: x_1x_2, number of targets: $x_1 : 9$, $x_2 : 3$, (b) rack: x_1x_3, number of targets: $x_1 : 6$, $x_3 : 3$, (c) rack: x_1, number of targets: $x_1 : 9$, and (d) racks: x_1x_2, x_1x_3, x_2x_3, number of targets: $x_1 : 9$, $x_2 : 3$, $x_3 : 3$. Plants are visualized as cubes for plot simplicity.

For ray j at location (x_{1j}, x_{2j}, x_{3j}), if

$$\begin{cases} x_{1j} \leq x_{w1-} & \text{or} \\ x_{1j} \geq x_{w1+} & \text{or} \\ x_{2j} \leq x_{w2-} & \text{or} \\ x_{2j} \geq x_{w2+} & \text{or} \\ x_{3j} \leq x_{w3-} & \text{or} \\ x_{3j} \geq x_{w3+}, & \end{cases} \tag{4.2}$$

then we say the ray has hit a wall. If for plant target i

$$F_i(x_{1j}, x_{2j}, x_{3j}) \leq 1, \tag{4.3}$$

then we say that ray j has hit plant i.

Initializing rays

Ray positions, $\boldsymbol{r}(x_1, x_2, x_3)$, are randomly initialized within a rectangular area defined by the "source tube" values ST_{1-12} (defined in Table 4.1) on the surface one of the six walls. For example, for the wall with surface normal $+\boldsymbol{e}_1$, rays will emanate from the point

$$\begin{cases} x_1 = x_{w1+}, \\ x_2 \in_{\text{rand}} [-ST_{11}, ST_{11}], \\ x_3 \in_{\text{rand}} [-ST_{12}, ST_{12}]. \end{cases} \tag{4.4}$$

As there are six walls and two source tube values per wall, there are a total of 12 source tube values.

Ray velocities, $\boldsymbol{v}$, are initialized with magnitudes equal to the speed of light and directions randomly determined from a set of "aperture" values A_{1-18}. As there are six walls and three aperture values per wall, there are a total of 18 aperture values. Once a direction of travel is determined from the aperture values, the direction is normalized and then scaled by the speed of light. That is, we first determine the un-normalized components of the direction (a_1, a_2, a_3):

$$\begin{cases} a_1 \in_{\text{rand}} [0, A_{x_1}], \\ a_2 \in_{\text{rand}} [0, A_{x_2}], \\ a_3 \in_{\text{rand}} [0, A_{x_3}], \end{cases} \tag{4.5}$$

then normalize

$$\begin{cases} \hat{v}_1 = \dfrac{a_1}{||\boldsymbol{a}||}, \\ \hat{v}_2 = \dfrac{a_2}{||\boldsymbol{a}||}, \\ \hat{v}_3 = \dfrac{a_3}{||\boldsymbol{a}||}, \end{cases} \tag{4.6}$$

where $||\boldsymbol{a}|| = \sqrt{a_1 + a_2 + a_3}$. Finally, we scale by the speed of the light, c, to obtain the components of the full initial velocity vector:

$$\begin{cases} v_1 = c\hat{v}_1, \\ v_2 = c\hat{v}_2, \\ v_3 = c\hat{v}_3. \end{cases} \tag{4.7}$$

Initial ray position and velocity determination is visualized in Figure 4.3.

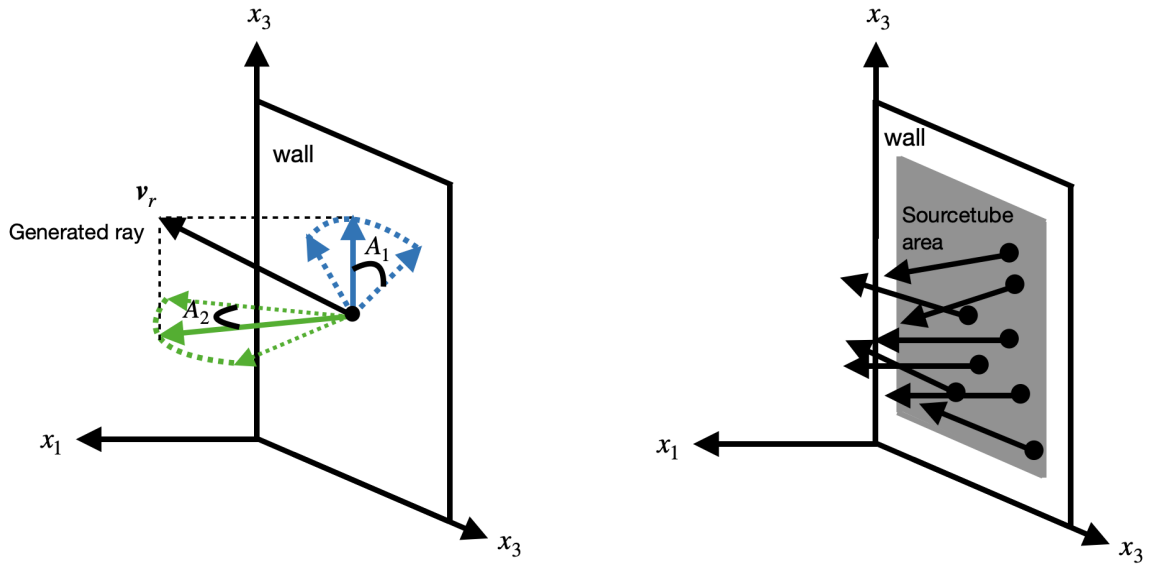

Figure 4.3: (a) Aperture settings determining initial ray direction. (b) Source tube parameters determining ray initialization area.

Ray power values are initialized as a fraction of the total power, P_w, coming from the wall associated with the initial ray position. If the total number of rays coming from the wall is N_r, then the power in each ray emanating from wall w is

$$P_{\text{ray}} = \frac{P_w}{N_r}. \tag{4.8}$$

As there are six walls and one total power value per wall, so there are a total of 6 wall power parameters P_{1-6}. The source tube, aperture, and wall power parameters comprise the 36 design parameters for optimization in this study.

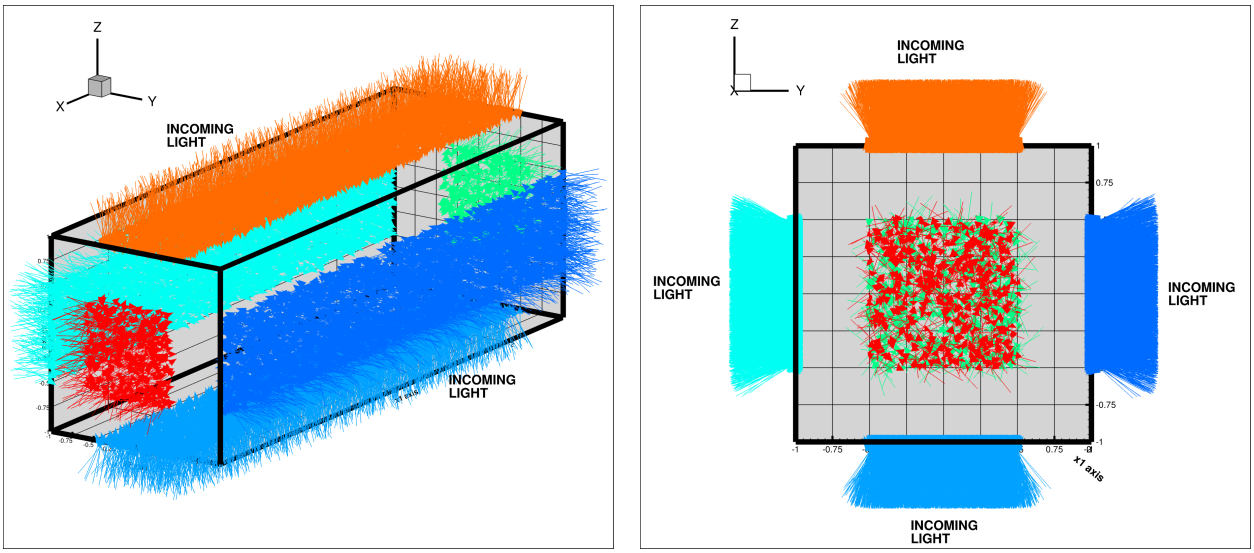

(a) (b)

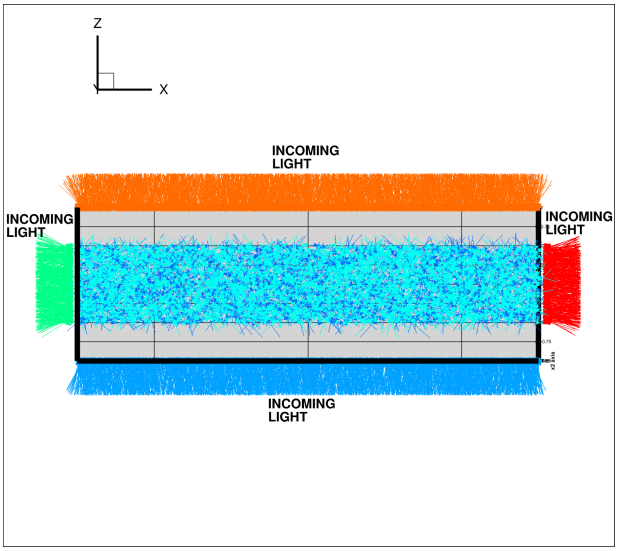

(c)

Figure 4.4: Ray initialization with 6 walls, aperture values A_{1-18} : 0.5 and source tube lengths ST_{1-4} : 0.5 and ST_{5-12} : 3. Ray color added for visual clarity.

Raytracing method

The details of the raytracing algorithm is identical to the greenhouse raytracing model introduced in Section 2. The power absorbed by the surface, P_{abs}, and the power retained

by the ray, P_{ref}, are computed as:

$$\begin{cases} P_{\text{abs}} &= (1 - \boldsymbol{\mathcal{IR}})P_{\text{inc}} \\ P_{\text{ref}} &= \boldsymbol{\mathcal{IR}}P_{\text{inc}} \end{cases} \tag{4.9}$$

where P_{inc} is the incident power. Ray power values are updated in each time step until the power in the ray falls below some threshold. At that point, the ray is considered fully absorbed and deactivated.

Time-stepping scheme

The power propagation scheme outlined in the previous section is achieved through an explicit time-stepping scheme with a time step size defined by

$$\Delta t = \left(\frac{\Delta x_1 + \Delta x_2 + \Delta x_3}{3c} \right) \xi \tag{4.10}$$

where $(\Delta x_1, \Delta x_2, \Delta x_3)$ are the voxel sizes per axis, c is the speed of light, and ξ is a tunable parameter for refining the step size. With higher values of ξ, the simulation runs faster and with lower values of ξ the collisions are modeled more accurately. In this study, we use $\xi = 2$ to accurately capture the ray interactions without significantly slowing down the simulation. A convergence study could be conducted by including ξ in the set of design parameters for more refinement, but this is beyond the scope of this study.

The rays are propagated in the system using the same explicit Forward Euler time-stepping scheme.

4.3 Machine-Learning, Optimization, and Automatic Design

Design parameters

The indoor farming system design consists of the following 36 design parameters:

$$\Lambda^i \equiv \{\Lambda_1^i, \ldots, \Lambda_N^i\} \equiv \{A_1, \ldots, A_{18}, ST_1, \ldots, ST_{12}, P_1, \ldots, P_6\} \tag{4.11}$$

where A_{1-18} are the aperture parameters (3 per wall) are used to determine the initial light direction, ST_{1-12} are the source tube values (2 per wall) that dictate the wall area in which the ray will be randomly initialized, and P_{1-6} are the total power values (1 per wall). Table 4.1 outlines which design parameters belong to each wall, where each wall is identified by its inward normal in the standard Euclidean basis.

Table 4.1: Design parameters associated with each wall.

Inward normal	Aperture parameters	Source tube length [m]	Power [W]
$-\boldsymbol{e}_1$	A_1, A_2, A_3	ST_9, ST_{10}	P_1
$\boldsymbol{e}_1$	A_4, A_5, A_6	ST_{11}, ST_{12}	P_2
$-\boldsymbol{e}_2$	A_7, A_8, A_9	ST_5, ST_6	P_3
$\boldsymbol{e}_2$	A_{10}, A_{11}, A_{12}	ST_7, ST_8	P_4
$-\boldsymbol{e}_3$	A_{13}, A_{14}, A_{15}	ST_3, ST_4	P_5
$\boldsymbol{e}_3$	A_{16}, A_{17}, A_{18}	ST_1, ST_2	P_6

Design fitness

The 36 design parameters define a design space which we can explore and evaluate with a cost function. Different parameter sets will result in different indoor farming system performance with lower values of the cost function corresponding to stronger design fitness. The definition of design fitness may differ between applications and the cost function can be tailored to each application. In this study, we seek to maximize the power absorbed by the plants inside the indoor farming pod. Accordingly, we construct the cost function

$$\Pi = 1 - \frac{\sum_{i=1}^{N_p} P_i}{\sum_{w=1}^{6} P_w} \tag{4.12}$$

where N_p is the total number of plants and the sum over P_w values represents the total initial power emitted by all 6 walls. The genomic optimization scheme will attempt to minimize Π, which ultimately maximizes the power absorbed by the targets. Note that the ratio of power absorbed over power irradiated in the cost function is non-dimensional and normalized.

Machine-learning optimization scheme: genetic algorithm

Given the cost function, the system can be optimized using the genetic algorithm described in Section 2. The genetic algorithm parameters and design parameter search bounds used in this work are included in Table 4.3.

4.4 Results and Discussion

Table 4.2: Indoor farming system parameters.

Symbol	Units	Value	Description
N_r	none	2000	Number of rays per face
`activeRacks`	none	x_1x_3, x_1x_2, x_2x_3	Active rack axes/planes
$N_{p,\pm1}, N_{p,\pm2}, N_{p,\pm3}$	none	$[9, 3, 3]$	Number of plants per axis
$\Delta x_1, \Delta x_2, \Delta x_3$	none	0.05	Voxel size
c	m/s	3×10^8	Speed of light
R_1, R_2, R_3	m	$2.75\Delta x$	Generalized radii
p_1, p_2, p_3	none	6	Generalized exponents

Table 4.3: Genetic algorithm parameters.

Symbol	Units	Value	Description
P	none	4	Surviving parent strings for breeding
K	none	4	Number of offspring per generation
S	none	24	Designs per generation
G	none	150	Total generations
A_{1-18}	none	$[0, 1]$	Aperture parameters
ST_{1-4}	m	$[0, 0.5]$	Source tube search bounds
ST_{5-12}	m	$[0, 3]$	Source tube search bounds
P_{1-6}	MW	$[1, 10]$	Total face power search bounds

We simulate a completely enclosed indoor farm with LED light sources on all six walls using the previously described digital-twin framework and optimization scheme. The dimensions of the simulated farming pod were $6 \times 1 \times 1$ m. We allow racks of plants to exist in the x_1x_2, x_1x_3 and x_2x_3 planes with generalized radii $R_1 = R_2 = R_3 = 0.1375$ m and generalized exponents $p_1 = p_2 = p_3 = 6$, effectively simulating the plants as bevelled cubes with volume 0.1375 m^3. For the racks in planes x_1x_2 and x_1x_3 there were $18 \times 6 = 108$ plants each and for the rack in plane x_2x_3 there were $6 \times 6 = 36$ plants, meaning the pod farm contained 252 plants in total. In each time step, we track the power absorbed by each plant, the fraction of rays interacting with a plant, and the total number of ray-surface interactions. Figure 4.6 shows the relative power absorption of different plants with red corresponding to the highest power absorption and blue corresponding to the lowest power absorption. While adjustable, we set the indices of refraction for the 6 walls to

($n_{w1-} = 10.0, n_{w1+} = 4.0, n_{w2-} = 1.5, n_{w2+} = 3.0, n_{w3-} = 9.0, n_{w3+} = 2.0$) and the index of refraction of the ambient container medium to $n_i = 1$. In all simulation figures in this work, a unique ray color denotes a distinct wavelength, but wavelength was not accounted for by the raytracing method used. Each wall $w = 1, \ldots, 6$ was initialized with power $P_w \in_{\text{rand}} 1 - 10$ MW and with ray density 2000 rays per source tube area. The indoor farming system parameters and the genetic algorithm parameters for optimization used in this study are included in Tables 4.2 and 4.3 respectively.

When simulating with equal index of refraction among all walls and plants, we find that the best design reduced the source tube areas to more closely overlap with the plant racks, increasing the ray density per source tube area and increasing the number of rays directly incident on the plants. With a larger number of rays directly incident on the plants, the number of reflections a ray makes is reduced, thereby decreasing the energy waste from reflections with each surface.

Optimal results are visualized in Figures 4.5 and 4.6 and are produced using the design parameters in Table 4.4. The relatively small optimal source tube areas depicted in Figure 4.6 can be attributed to not specifying a power absorption limit for the closest plant targets. The evolution of the best design cost and average design cost across the population over 150 generations with 24 design strings per population is shown in Figure 4.7. Every 10 generations, we allow the population to re-adapt by redefining the search bounds for each design parameter to be a range about the parameter values of the best string seen thus far.

These results serve to demonstrate a framework for the modeling and optimization of an indoor farming pod. This framework can be modified to better capture all aspects of the system by extending the design parameters and modeling other physical phenomena such as water absorption, air flow, multi-wavelength energy tracking, and setting power absorption caps for different plant types.

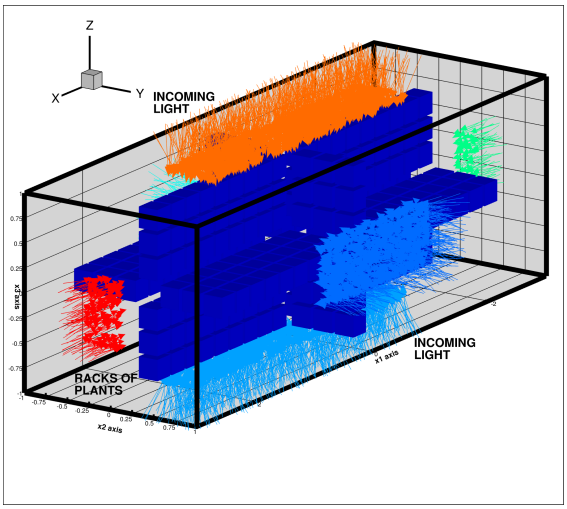

(a) Isometric view of optimized indoor farming design.

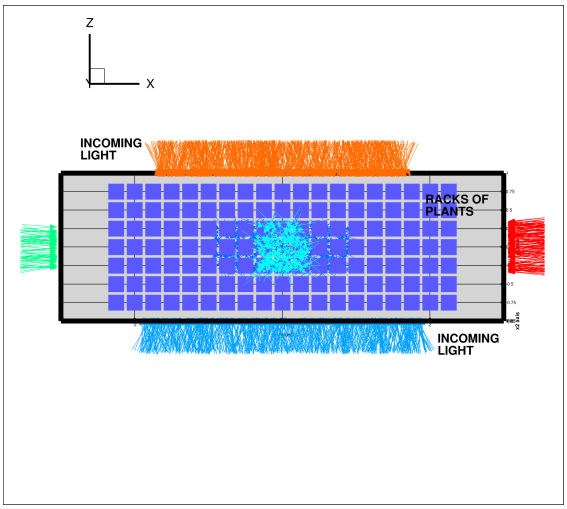

(b) Side view of optimized indoor farming design.

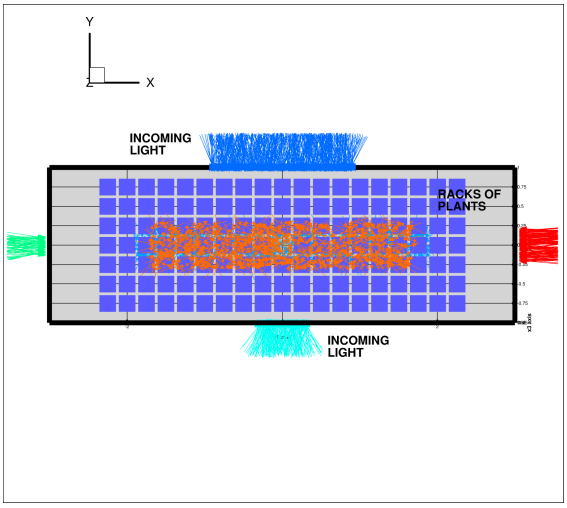

(c) Top view of optimized indoor farming design.

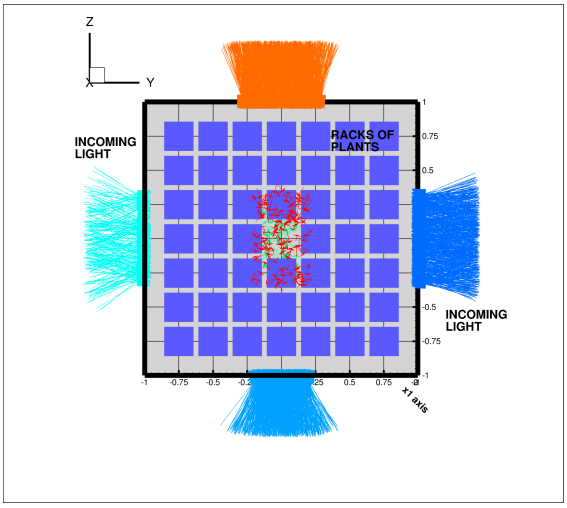

(d) Front view of optimized indoor farming design.

Figure 4.5: Detailed views of optimized indoor farming system design. Ray color added for visual clarity.

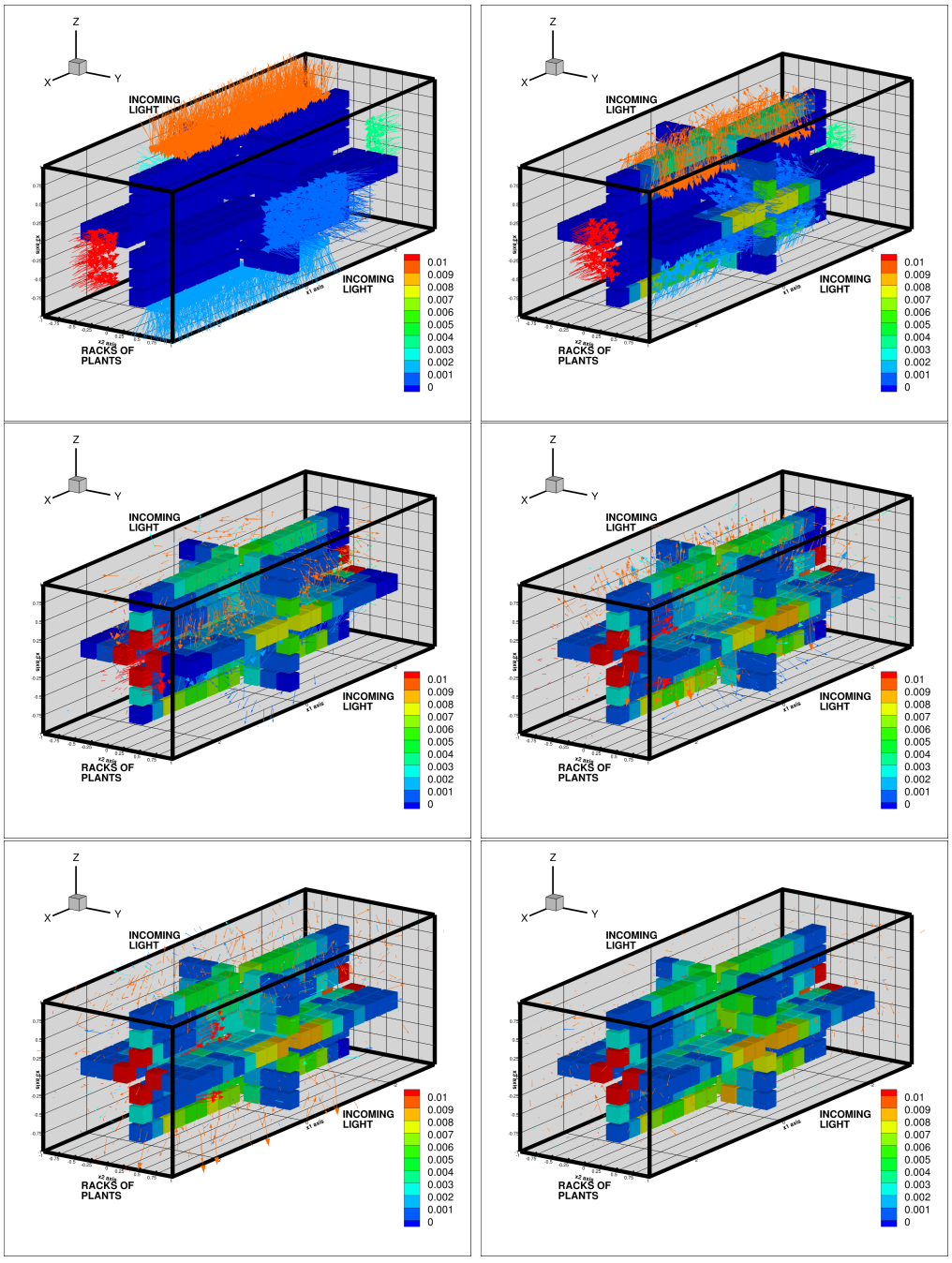

Figure 4.6: Optimal indoor farming system light pulse snapshots. Ray color added for visual clarity. Colorbar added to show differential power absorption by plants. Red corresponds to higher power absorption and blue to lower power absorption.

Table 4.4: Optimal indoor farming design parameters corresponding to $\Pi_{\text{best}} = 0.153$. aperture values are unitless. Source tube values in meters. Power values in megawatts.

A_1	A_2	A_3	A_4	A_5	A_6
0.567	0.108	0.174	0.636	0.216	0.195
A_7	A_8	A_9	A_{10}	A_{11}	A_{12}
0.515	0.252	0.421	0.740	0.416	0.578
A_{13}	A_{14}	A_{15}	A_{16}	A_{17}	A_{18}
0.586	0.394	0.198	0.597	0.690	0.199

ST_1	ST_2	ST_3	ST_4	ST_5	ST_6
1.909	0.207	1.692	0.295	0.326	0.328
ST_7	ST_8	ST_9	ST_{10}	ST_{11}	ST_{12}
0.914	0.334	0.120	0.283	0.215	0.360

P_1	P_2	P_3	P_4	P_5	P_6
5.66	5.68	7.22	6.29	3.28	4.03

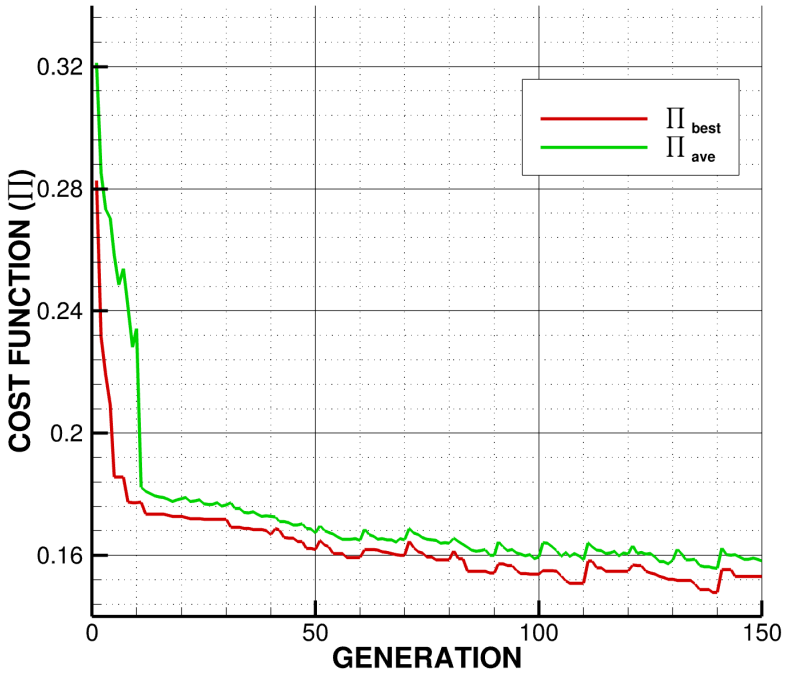

Figure 4.7: Cost function evolution over 150 generations. The plots show the cost of the best performing design (red) and the average cost of the entire population (green) as a function of successive generations. The GA was allowed to re-adapt every 10 generations. The lowest cost in generation 1 was $\Pi_{\text{best}}^{g=1} \approx 0.2826$ and was reduced to $\Pi_{\text{best}}^{g=150} \approx 0.1531$ by generation 150. This is a reduction of $\sim 45.82\%$.

4.5 Summary

Indoor farming is a promising mode of next-generation agriculture offering numerous benefits such as year-round crop cultivation, reduced transportation costs, and enablement of urban farms. However, these systems still face challenges related to energy consumption, and there has been limited quantitative analysis of their overall efficiency. To fill this gap and promote innovative design, we introduce a cost-effective digital-twin to analyze the optical properties of an indoor farming pod using a raytracing model. We utilize a genomic optimization scheme to identify the most optimal LED geometric configurations and emission characteristics toward maximizing energy absorbed by the constituent plants. The proposed digital-twin and optimization framework serves as a foundational framework that takes a physics-driven approach to optimize energy flow and paves the way for more sustainable indoor farming practices.

To adapt the framework to other indoor farming configurations, we can adjust design objectives via cost function design and incorporate constraints via parameter search bounds. The framework could also be extended to include models for water usage or crop-specific reactions specific to different chemicals/pesticides, thereby enhancing the accuracy of the digital-twin. Extending the framework to include wavelength-specific power flow could further improve predictions of energy efficiency and crop yield by providing each plant with its ideal lighting conditions. Such refined models can serve as valuable tools for testing and estimating how a particular design would perform in the real world, enabling farmers to make informed decisions and effectively optimize their own indoor farming setups.

The physics model developed in this chapter is effective in the preliminary evaluation of an indoor farming pod system. However, since our aspiration is to build a digital-twin framework, which allows for real-time control and optimization, we need to base our simulation on a real-life system. Thus, we will analyze an indoor farming pod that is currently installed in Richmond, CA by UC Berkeley in the next chapter. This will allow us to analyze the power consumption of the different components (irrigation, climate control, lighting) of an indoor farming pod and size a solar power generation station which will allow for sustainable crop production.

Chapter 5

Power Sizing Analysis

The optical model of the indoor farming pod explored in the previous chapter provides useful information regarding the optical power characteristics of the system. However, it is important to note that the aforementioned next-generation indoor farming systems are costly to build and operate due to the highly controlled nature of the environment, requiring precise lighting, irrigation, and climate control. In order to complete our digital-twin model framework, we will need to base our simulation on a real-life farming pod system, which can be then controlled and optimized in real-time. We have so far developed the light scattering model and will be evaluating the optical power characteristics of a real-life indoor farming container next. This chapter will explore the power requirements to build and operate an example indoor farming system and will develop power generation and energy storage solutions.

5.1 Background Information

Indoor farming has been a prominent way of agricultural production for a long time in the form of greenhouses. The basic types of greenhouses are translucent structures that allow sunlight to reach the plants while shielding them from the outside weather conditions. In addition, these greenhouses would block any evapotranspiration from exiting the crop growth area and keep the environment humid, as well as keep the heat from exiting due to the greenhouse structure.

The emerging food production technologies include augmenting the indoor farming sector by incorporating state-of-the-art lighting, irrigation, climate control and crop harvesting devices. One popular approach is the aforementioned indoor "vertical" farming, which stacks plants in the most optimal way to maximize number of plants grown in a given amount of space. To be able to pack these plants in the best way possible, it implements an irrigation method that delivers nutrients directly to the plant roots with no soil (i.e. hydroponics and aeroponics).

Figure 5.1: Indoor farming system example. Photos from public domain: https://pixabay.com.

Aeroponics suspend plant roots in air and use mist to deliver nutrients and water, while hydroponics submerge the plant roots in water and cycle nutrients within a time period. We have previously explored hydroponic nutrient delivery systems within the context of the solar greenhouse digital-twin model, in Section 2 through the hydroponic tower raytracing and irrigation power requirements. Similarly, we have also alluded to the use of hydroponics in the indoor farming optical model in Section 4 through the racks the plants were installed in the indoor farming pod. While the hydroponics power requirements is a significant contribution to the overall system power characteristics, one would need to evaluate the entirety of the indoor farming system to assess the cost to run such systems.

Indoor farming systems, depending on the type, can be costly to install and to operate, in terms of equipment cost and electricity use. While conventional greenhouses provide a passively controlled environment, novel approaches such as vertical farming use considerably more electricity to grow the same crop [48, 49] due to artificial lighting and climate control. While vertical farming has its advantages, such as freshness of produce, food safety, and reduced water use, the cost to install and operate these systems prevents them from being widely used for crops other than leafy greens, which are said to represent 57% of the vertical farming crops [50]. Leafy greens are said to be the most financially viable crop to grow in vertical farms due to the short crop season, mostly edible biomass, and the light weight the

vertical farming structures need to support. To be able to utilize vertical indoor farming systems to grow other crops, the systems need to be financially viable.

The cost of running an indoor vertical farm will be in two forms: capital cost (i.e. equipment purchase, structure construction) and the running cost (i.e. electricity, water, nutrients, equipment, and structural maintenance). While the capital cost is fixed and will be dependent on the equipment choices, we would expect the cost per crop to go down as the facility scales up. The running cost of the system will also be dependent on the scale of the facility, one can employ sustainable and renewable practices to alleviate the major running cost: *electricity*. It has been disclosed in a 2021 CEA Census that only 37% of the CEA facilities use renewable sources for electricity, for which 2/3 generate it onsite and 1/3 obtain it from the utility provider [48].

This chapter will evaluate the power requirements to operate an example indoor farming system based in Richmond, CA. This will provide a useful insight into the current state of indoor farming, in terms of the container sizing, equipment used, and power draw. We will then explore possible renewable energy sources and energy storage solutions that can power the said indoor farm and size it accordingly.

5.2 Indoor Farm Power Requirements

In this chapter, we will explore the power requirements of an indoor farm. The indoor farming system that will be used throughout this study was recently acquired by the University of California, Berkeley and AI Institute for Next Generation Food Systems (AIFS) and is installed at the Richmond Field Station Facility in Richmond, California, USA. This unit will provide an essential tool to validate currently developed models by the AIFS researchers and conduct experiments. Given the container size and the equipment needed to operate the pod, we can assess the power requirements of the system on a day-to-day basis.

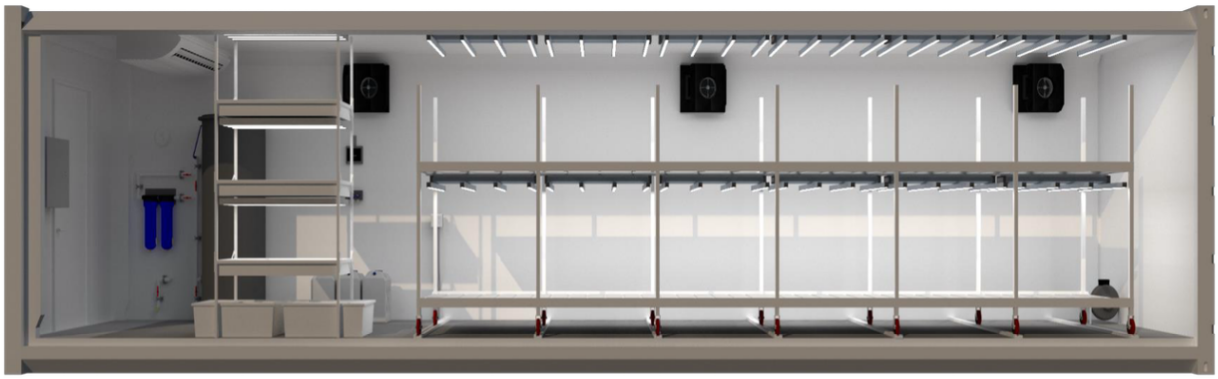

Figure 5.2: CropBox indoor farming system installed at RFS.

The indoor farming system, CropBox, was purchased from Vertical Crop Consultants [51] as a Type 40' High Cube Reefer structure with included HVAC, electrical, lighting, nursery, hydroponics, and sensor equipment, as seen in Figures 5.2 and 5.3. The indoor farm specifications and equipment are tabulated in Table 5.1.

Table 5.1: Indoor Farm Equipment Specifications.

Equipment	Type	Specs
Container	Structural	$40' \times 8' \times 9.5'$ High Cube Reefer
Air Conditioner	HVAC	TGM Seer 21 48,000 BTU Minisplit
Dehumidifier	HVAC	180 Pint Ideal-Air Pro Series
Fan	HVAC	(4) Quest F9 Air Mover 925 CFM
LED Grow Light	Lighting	(48) (Model-V) ThinkGrow Horticulture
Nursery Tray	Hydroponics	(3) $2' \times 4'$ Vertical Ebb and Flow
Nursery Light	Lighting	(3) AgroLED Sun 48 6500k 187 Watts
Tank	Hydroponics	120 gal Reservoir
Pump	Hydroponics	Leader Ecojet 110 Pump
Dosing Pump	Hydroponics	Nuravine Parastaltic (3 per reservoir)
EC Module	EC	Trolmaster EC
Sensors	EC	Temperature, Humidity, CO_2, Light Levels

(a) (b)

(c) (d)

Figure 5.3: Detailed views of the indoor farming container located in Richmond, CA.

The total power draw of the indoor farming container can be calculated by first tabulating the power draw of each component. Note that only major contributors to the power usage are considered, which include the air conditioning, lighting, and pumping equipment. The power draw of these equipment is tabulated in Table 5.2.

Table 5.2: Indoor Farm Equipment Power Draw.

Equipment	Name	Power Draw
Air Conditioner	TGM Seer 21 48,000 BTU Minisplit	48,000 BTU/hr [52]
Dehumidifier	180 Pint Ideal-Air Pro Series	1350 W [53]
Fan	(4) Quest F9 Air Mover 925 CFM	228 W [54]
LED Grow Light	(48) (Model-V) ThinkGrow Horticulture	350 W [55]
Nursery Light	(3) AgroLED Sun 48 6500k 187 Watts	187 W [56]
Pump	Leader Ecojet 110 Pump	800 W [57]

The total power draw of the indoor farming container is then calculated to be 34.5 kW. While there are other contributors to the power usage of the indoor farming system (i.e. external water pumps, electrical connectors, environment control units, lighting control units, etc.), the subsequent power calculations will use the power draw of the major contributors.

The indoor farming container is able to grow a variety of plants that span specialty plants for vaccine development to common leafy greens. In this study, we will use the common June-bearing strawberry [58] as an example. This type of strawberry produces the crop in 2-3 weeks in spring. We will use the crop season duration and the time of the year the crop grows naturally on an open field to base our power source sizing and energy storage calculations. Note that the crop dynamics of the strawberry in an indoor farming setting are beyond the scope of this power-sizing study. The indoor farming container power requirement calculations will assume that the system is running for the entire day during the crop season.

While the required power can be supplied by the utility provider, the goal is to operate this next-generation food production system in a sustainable way. The area where Richmond Field Station is located can be used to install a photovoltaic field that can supply the necessary electricity to the pod. While the environmental concerns about disrupting the flora or fauna of the RFS are valid and highly important, we will only explore this as a hypothetical scenario. Solar power is only available during the day hours, therefore, we will also explore energy storage strategies to power the indoor farm at night. The next section will calculate the required sizing of the solar field and the energy storage solutions.

5.3 Power Generation and Energy Storage Solutions

The state-of-the-art indoor farming systems provide a more sustainable way of food production by allowing the crops to be grown in densely populated areas by packing the plants in a smaller space through vertical farming and soil-free nutrient delivery systems. However, the indoor farming container this study is focused on is powered by the local utility provider, which may or may not generate the electricity delivered from renewable sources. In

addition, the power grid can be overloaded during peak times, requiring an alternative power solution. Another possible issue that may arise from indoor farming getting more popular in the future is the overloading of the grid due to many of these farms running concurrently.

We will develop renewable energy generation strategies to power our indoor farming container to reduce the carbon footprint and increase sustainability. this study will evaluate the power generation required to operate the indoor farming container as well as the energy storage solutions needed to run the farm when the power source is not available due to weather conditions.

Power Generation

Possible renewable options to power our indoor farming container are wind and solar. While the Bay Area is particularly windy, installing large wind turbines is not feasible due to high seismic activity and the local wildlife in Richmond Field Station area. Therefore, this study will use solar power to calculate the sizing required to power our container. While multiple solar power technologies are gaining popularity (i.e. photovoltaics (PVs), concentrated solar power (CSP)), photovoltaics would be the most feasible due to their ease of installation, wide availability, and cost.

Solar panel technologies have improved significantly with certain research modules reaching efficiencies of approximately 39% [59]. Different companies and research institutions such as Fraunhofer, and Hawnwa Qcells have been working on developing novel and more efficient solar cells with different materials. We will perform the solar farm sizing calculations with the assumption that the solar panels are of the most common type, monocrystalline silicon photovoltaics with efficiencies up to 20% [59]. These panels are widely available for purchasing and would be a reasonable indoor farmer's choice of solar panels.

Energy Storage

The aforementioned concentrated solar power (CSP) technology inherently enables energy storage by focusing the solar radiation onto a receiver tower which has a working material that absorbs thermal energy. This energy can then be used to power a conventional steam turbine to generate electricity. On the other hand, solar panels directly generate electricity using the photovoltaic effect. Thus, we also need to consider energy storage in the form of solar batteries to power the indoor farming system when sunlight is not available to generate electricity. The solar batteries will enable the solar farm to store excess electricity.

Power Sizing

The power sizing of the solar farm field will be based on the energy requirements of our indoor farming container, which is assumed to be operating 24 hours a day for 3 weeks to produce the June-bearing strawberries in Spring. We will first need to get the solar profile of Richmond, CA during the crop season to accurately size the solar panel field needed

to power the container. The study will be based on a crop season spanning from March 1st to March 21st of 2023. We can utilize the pysolar package previously used to simulate the agrophotovoltaic greenhouse in Section 2. The solar profile is discretized in 15-minute intervals during the 3-week period.

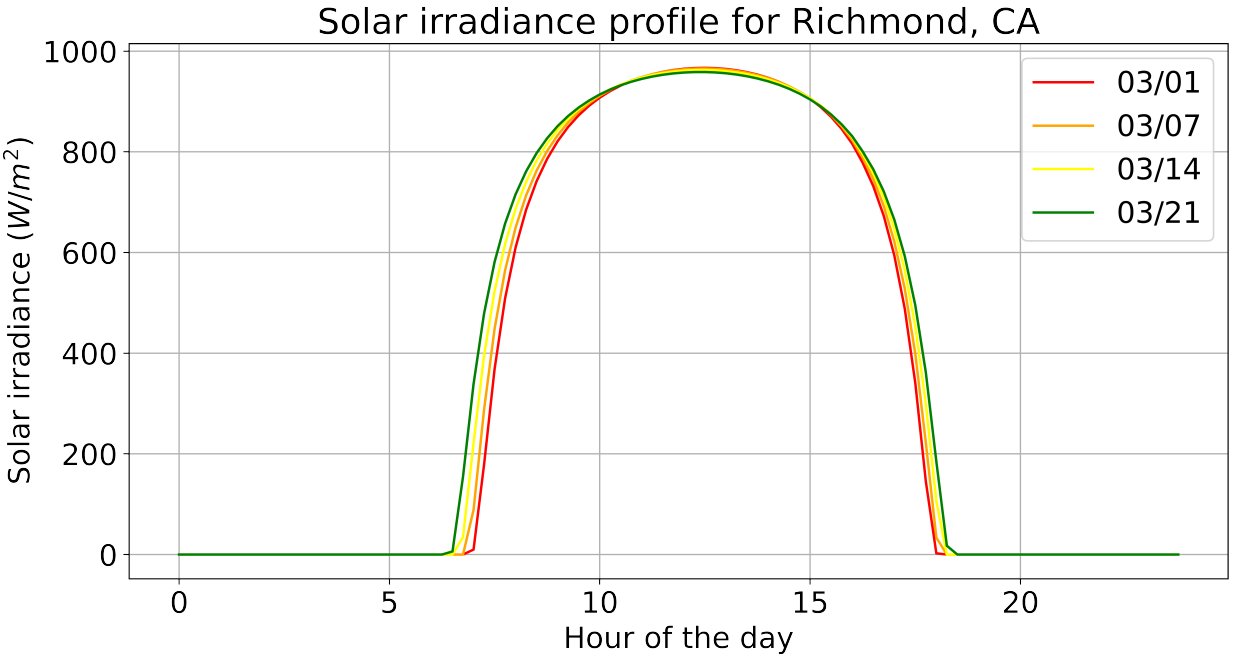

Figure 5.4: Richmond, CA clear sky radiation profile for March 1st - March 21st, 2023.

Figure 5.4 shows that the solar radiation, with the assumption that the weather conditions are clear skies, varies slightly throughout the year and reaches a maximum of 967 W/m^2. The solar irradiance will let us calculate the power output from the solar panels that will be hypothetically installed at Richmond Field Station. The commercial solar panels list their power output in Watts at Standard Test Conditions (STC). STC provides a common standard for testing and evaluating the solar panel performance under certain conditions: (1) zero solar incident angle, (2) 1000 W/m^2 solar irradiance, (3) 25°C ambient temperature, (4) 1.5 air mass coefficient (AM), and (5) zero system losses [60].

For our power sizing calculations, we will assume that the solar farm will consist of monocrystalline solar panels with tracking that will ensure the solar incident angle is always zero. The temperature and wind variation and their effect on solar panel performance are far more complex than the solar irradiance effect and is out of scope of this study. Similarly, losses within the individual systems, including PV panels, inverters, and other electrical equipment, as well as the battery packs to store excess energy, will not be considered.

The solar panel chosen for sizing the solar farm is the Renogy 550W Monocrystalline Solar Panel which outputs 550 W of power at STC using Passivated Emitter and Rear Contact

(PERC) solar cells with an efficiency of 22.8% [61]. We will assume that the power output will scale linearly with the solar irradiance, where the actual solar power output of the panel is:

$$P_{actual} = \left(\frac{P_{irrad}}{1000}\right) * 550 \text{ W} \tag{5.1}$$

Then, we can calculate the power output profile of a single panel during the crop season:

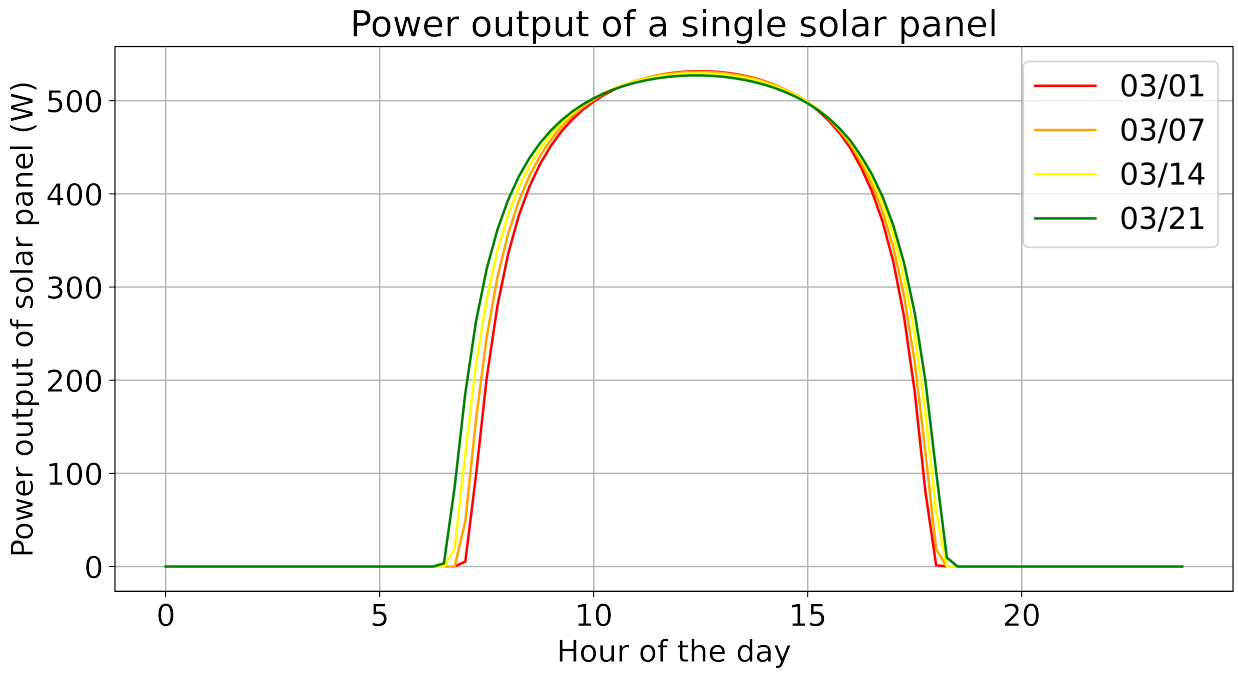

Figure 5.5: Power output profile of a single solar panel.

The power draw of the indoor farm was previously calculated to be 34.5 kW, which needs to be supplied by the solar panels during the day and the solar batteries at night. The number of solar panels and the solar battery capacity required to power the system day and night can be assessed by matching the solar farm energy production to the energy requirement of the pod over the crop season. The energy profile of the pod and a single panel for March 1st, 2023 is shown in Figure 5.6.

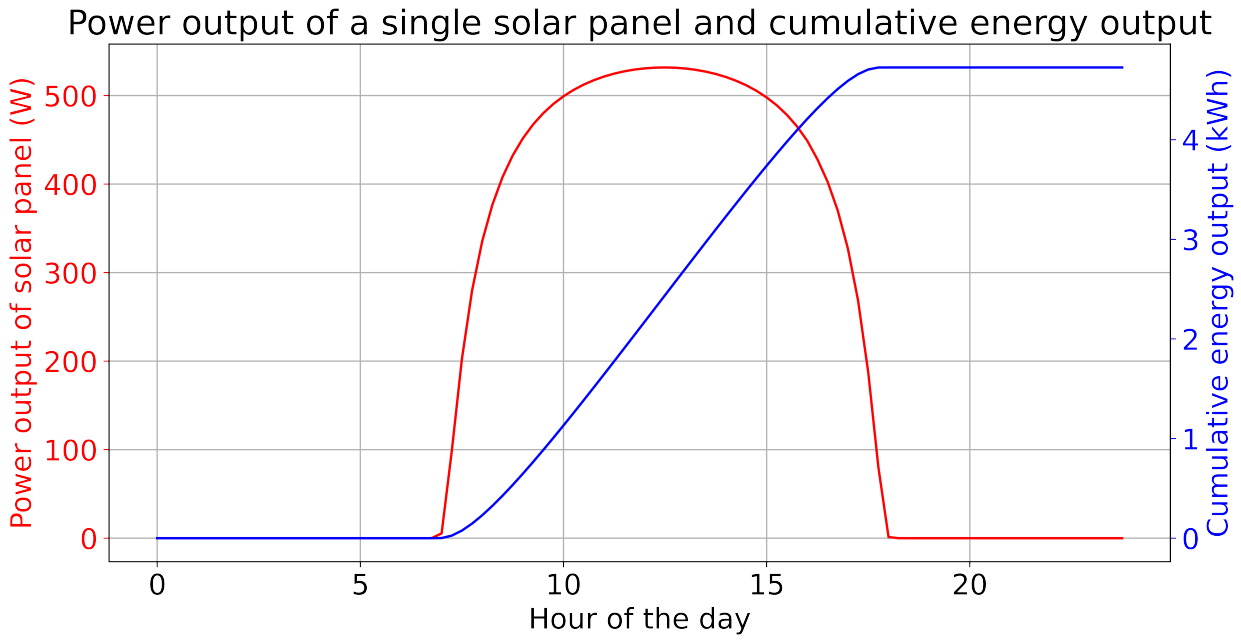

(a)

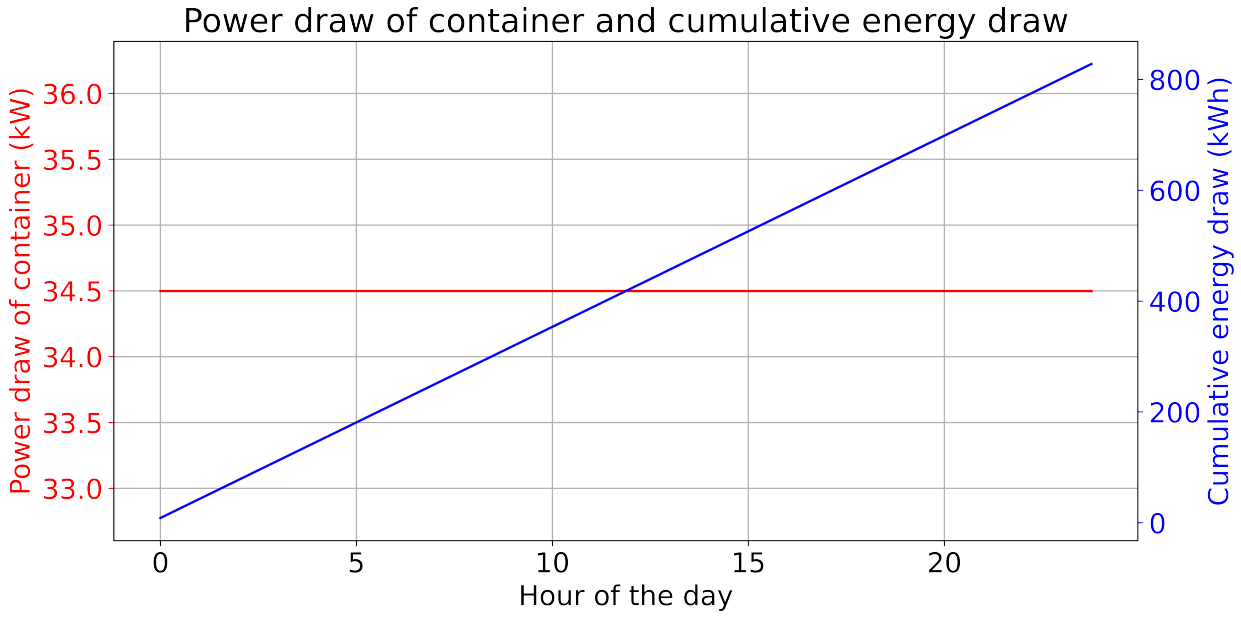

(b)

Figure 5.6: Energy profiles for: (a) Power output of a single solar panel and cumulative energy output for March 1st, 2023. (b) Power draw of container and cumulative energy draw.

In order to power the pod purely on solar power generated during the day, the cumulative energy production per day needs to match the cumulative energy requirement of the pod. While one can match the cumulative energy production for the entire crop season, this study will evaluate it on a daily basis and size the solar panel field according to the "worst" day in terms of solar power generation, determined by the solar irradiance profile for Richmond, CA during the crop season.

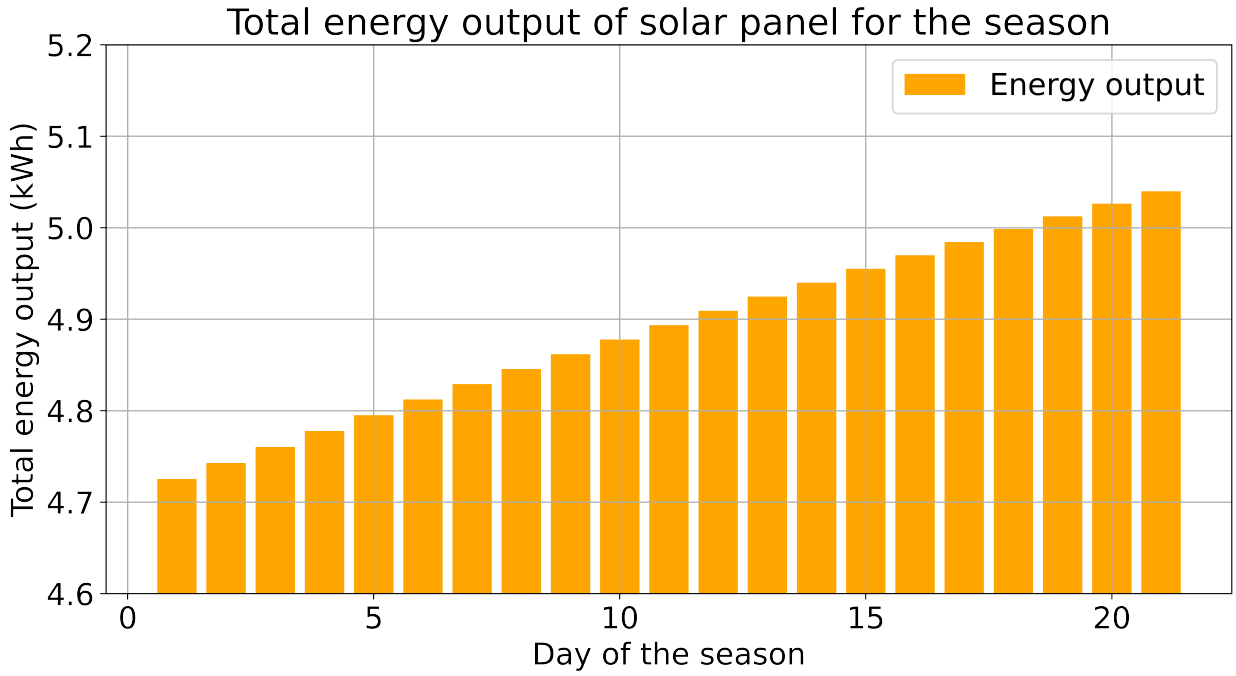

Figure 5.7: Energy output profile of a single solar panel between March 1st - March 21st.

As seen in Figure 5.7, the solar power generation efficiency will be the lowest on March 1st and will be the basis for our solar field sizing calculations. The indoor farming pod requires 827.98 kWh of energy per day to operate. Since the minimum amount of energy produced by a single solar panel during the crop season is 4.73 kWh, our calculations yield that $N_{panel} = 176$ panels are needed to satisfy the energy requirements on the day with the lowest solar irradiance. The resulting configuration produces the following energy profile:

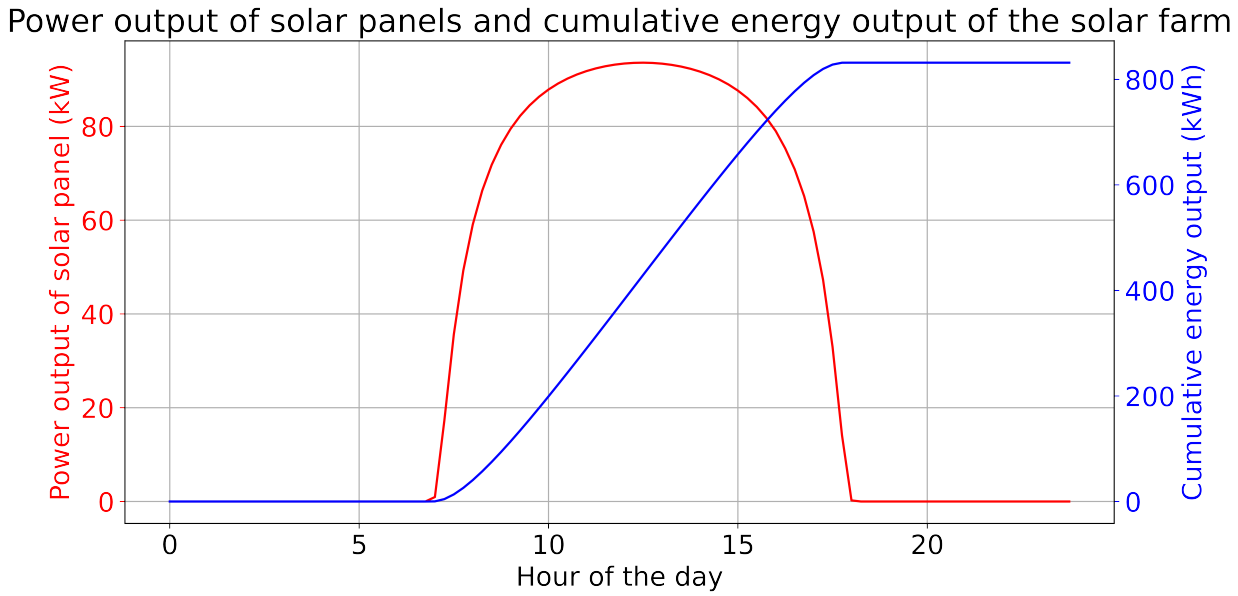

(a)

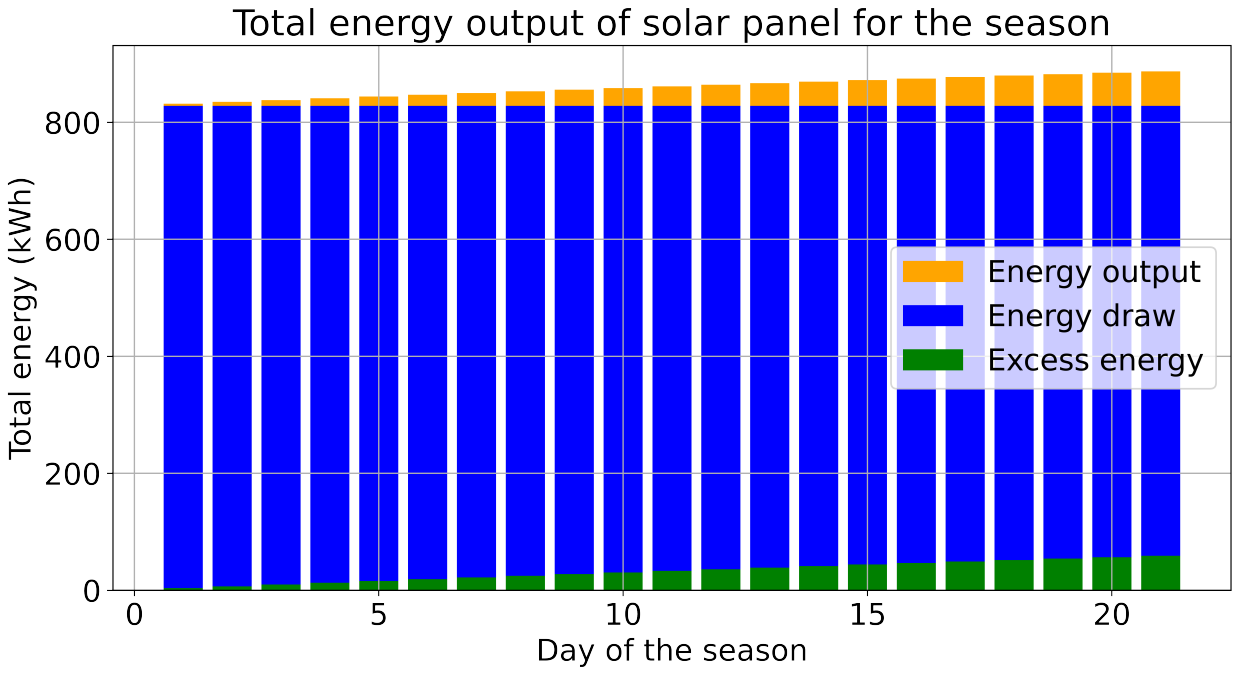

(b)

Figure 5.8: (a) Power output and (b) Total energy output profile of the solar farm (N_{panel} = 175).

As the solar irradiance increases throughout the crop season, the energy produced by the solar panels will be more than the pod energy requirements and can be sold back to the grid, if possible. Lastly, we need to calculate the number and the capacity of the solar batteries required to store the excess energy the solar panels produce to power the pod at night. The batteries will be expected to reach full capacity on the day with the most solar radiation, March 21st. The calculation yields 261.12 kWh of energy that needs to be stored to be used when solar power is unavailable. While there are many solar batteries commercially available, we will use the Tesla Powerwall 3 [62] with a capacity of 13.5 kWh and an 11.5 kW continuous power output. We would then require 20 of these solar batteries to power the system.

Table 5.3: Solar farm and energy storage parameters for the indoor farming system.

Parameter	Value
Solar panel type	Renogy 550W Monocrystalline Solar Panel
Solar panel power output at STC	550 W
Solar farm size	176 solar panels
Solar farm peak power output	93.59 kW
Total energy output of the solar farm	18071.97 kWh
Total energy draw of the container	17387.62 kWh
Total excess energy of solar farm	684.35 kWh
Battery type	Tesla Powerwall 3 (Lithium-ion)
Battery capacity	13.5 kWh
Energy storage size	20 batteries
Combined energy storage	270.0 kWh

The solar farm and battery storage solution parameters to completely power the indoor farming system on renewable and sustainable energy practices are tabulated in Table 5.3. While the calculations performed simplify the power analysis of the real-life indoor farming system, this can provide a useful tool in evaluating the feasibility of using on-site renewable energy sources to power the next-generation food systems.

5.4 Summary

Indoor farming systems, depending on the type, can be costly to install and to operate, in terms of equipment cost and electricity use. While conventional greenhouses provide a passively controlled environment, novel approaches such as vertical farming use considerably more electricity to grow the same crop due to artificial lighting and climate control. To be able to utilize vertical indoor farming systems to grow other crops, the systems need to be financially viable. The running cost of the system will also be dependent on the scale of the

facility, one can employ sustainable and renewable practices to alleviate the major running cost, which is electricity.

This chapter analyzed the power requirements of an indoor farm, run by the University of California, Berkeley, and AI Institute for Next Generation Food Systems (AIFS) and installed at the Richmond Field Station Facility in Richmond, California, USA. This unit will provide an essential tool to validate currently developed models by the AIFS researchers and conduct experiments. Given the container size and the equipment needed to operate the pod, we can assess the power requirements of the system on a day-to-day basis. While the calculations performed simplify the power analysis of the real-life indoor farming system, this can provide a useful tool in evaluating the feasibility of using on-site renewable energy sources to power the next-generation food systems.

We have so far developed simulation and optimization strategies for different next-generation food systems, including hydroponic solar greenhouses and indoor farming pods by using optical modeling strategies. One advantage of our geometric raytracing simulation method is that it can be coupled with other physics models (i.e. heat modeling, crop modeling, etc.). To conclude our study, we will finally look at how the developed optical modeling framework can be coupled with a crop model, which will allow for a more accurate crop growth response to the lighting of the domain.

Chapter 6

Extensions: Crop-driven Optimization of Agrophotovoltaics

The optical modeling and optimization framework developed in this study can easily be adapted to include other physics models to more accurately represent the real-life system and create a more realistic digital-twin. One possible coupling of the raytracing model is with a crop model, which will provide insight into the crop growth and light and water use efficiency of the plants. While the energy optimization function that evaluates the power absorption of surfaces provides a good starting point, the intricacies of crop growth require us to model the crop dynamics of the system for a more accurate system optimization framework. The light response of the surfaces can inform the crop model to better represent the incoming radiation and therefore the crop performance metrics.

6.1 Model Overview

This chapter aims to combine the raytracing framework with a crop model to evaluate agrophotovoltaic performance based on a crop-centered approach [63]. A digital-twin of an open-field agrophotovoltaic system is generated using the light model and the crop model to optimize the system design over a specified crop season with associated ambient parameters.

6.2 Digital-Twin Model

Light Model

Model Assumptions

The light model simulates a light pulse applied to the agrophotovoltaic system at hourly time intervals for hours where the sun is above the horizon for every day in a specified crop season. Solar angles are simulated using an open-source python package `pysolar` while

solar radiation values are read from a weather file. Increasing the number of simulated days rapidly increases runtime for the simulation, therefore, certain assumptions are made to reduce computational load:

- The solar panels are identical in shape, installation angle, and material,
- The light model flashes a unit area of the agrophotovoltaic field, assuming the distribution of solar panels on the field is uniform,
- The solar panels are bifacial, therefore able to absorb energy reflected from ground and other solar panels.

The detailed assumptions regarding the raytracing framework can be found in Zohdi [21].

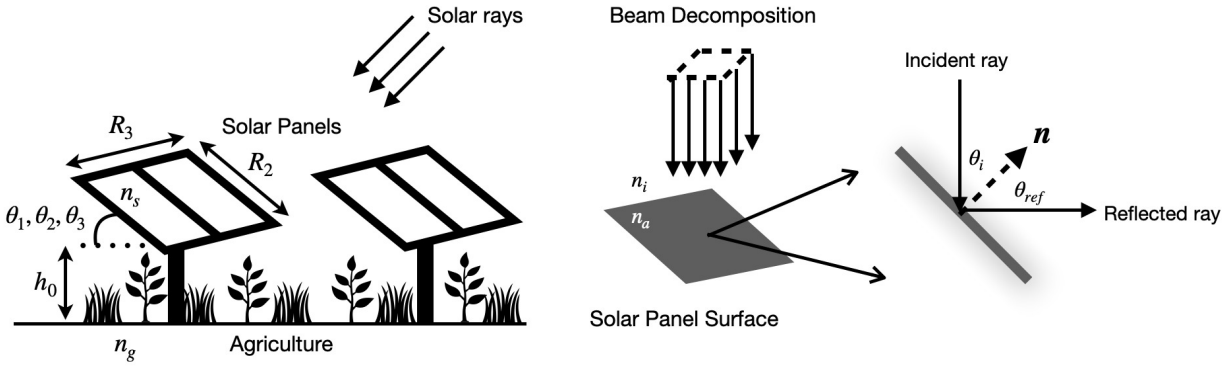

Figure 6.1: Left: Modeled APV system. Right: Beam decomposition for the raytracing model.

Solar Panel Geometry

The solar panel geometry is assumed to be known and described by a surface function, $F(x_1, x_2, x_3)$. The solar panel shapes are generated using the 3D-ellipsoidal equation:

$$F(x_1, x_2, x_3) = \left|\frac{x_1 - x_{1o}}{R_1}\right|^{p_1} + \left|\frac{x_2 - x_{2o}}{R_2}\right|^{p_2} + \left|\frac{x_3 - x_{3o}}{R_3}\right|^{p_3} \tag{6.1}$$

where (R_1, R_2, R_3) are the generalized radii, (p_1, p_2, p_3) are the exponents of the generalized ellipsoid, and (x_{1o}, x_{2o}, x_{3o}) are the center location of the ellipsoid. These are the design parameters we will optimize using the genomic optimization framework. Figure 6.2 shows various shapes the solar panels can attain.

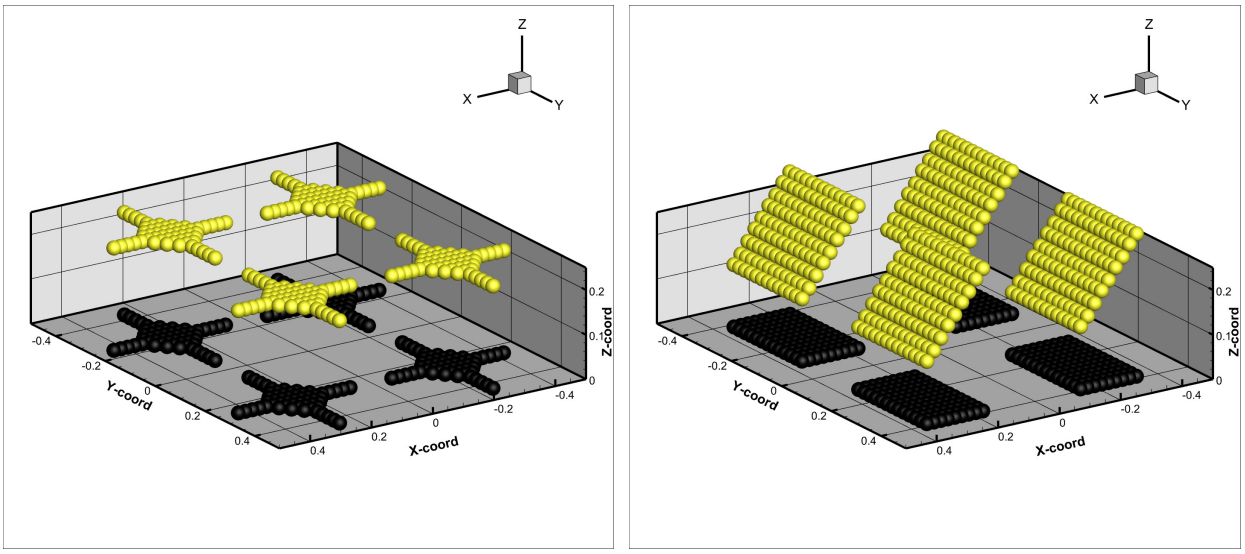

(a) (b)

Figure 6.2: Example solar panel shapes generated using the 3D-ellipsoidal equation for (a) $(\theta_1, \theta_2, \theta_3) = (0, \pi/2, \pi/2)$,$(R_1, R_2, R_3) = (0.002, 0.2, 0.2)$, $(p_1, p_2, p_3) = (5, 1/2, 1/2)$ and (b) $(\theta_1, \theta_2, \theta_3) = (0, -\pi/4, 0)$,$(R_1, R_2, R_3) = (0.002, 0.15, 0.15)$, $(p_1, p_2, p_3) = (20, 20, 20)$. The shadow cast by the panels at noon can be seen on the ground surface.

Rays traveling through the system collide with the solar panels if $F(x_{1,j},\, x_{2,j}, x_{3,j}) \leq 1$, where j indicates each ray. As the agrophotovoltaic system includes more than one panel on the field, the algorithm will check if a ray has collided with any of the solar panels located at $(x_{1o,i}, x_{2o,i}, x_{3o,i})$. Similarly, the ray is assumed to hit the ground surface if $x_{3,j} \leq 0$. The power absorption by the surface and power reflected by the ray can be determined using reflectivity calculations, which are described in the next section.

Raytracing Algorithm

It is assumed the light incident on the agrophotovoltaic system can be discretized as a collection of rays, which are propagated through the system using a time-stepping scheme. The initial collective power of the rays, P_{tot}, is read from a weather file for the given date, time, and location as the clear sky radiation given in $\frac{W}{m^2}$.

The details of the raytracing algorithm are identical to the greenhouse raytracing model introduced in Section 2. The surface power absorption and ray power retention are calculated at each ray-surface interaction throughout the simulation. The power absorbed by the surface can be calculated by

$$P_{abs} = (1 - \boldsymbol{\mathcal{IR}})P_r \tag{6.2}$$

The remaining power in the ray is calculated as follows:

$$P_{ref} = \mathcal{IR} P_r \tag{6.3}$$

The ray is tracked in the system as long as:

- the ray is within the system domain limits,
- its power is above the specified power threshold P_{min}.

The rays are propagated in the system using the same explicit Forward Euler time-stepping scheme.

Crop Model

Crop modeling aims to take in measured inputs and an understanding of plant physiological processes to determine when and how a crop will grow. This framework utilizes the SIMPLE Crop Model [64].

SIMPLE Crop Model

The SIMPLE Crop Model is a model designed to simplify crop modeling to basic components. It is well-validated and uses simple parameters allowing for straightforward and fast implementation. The model works on a daily time step by first looking at the crop's temperature, and determining where in the growth process it should be through cumulative thermal time. Once crop temperature is determined to be within the proper range, the growth stage and light input plus other crop parameters are used to simulate daily biomass growth, which is them summed through the season. At the end of the season, the cumulative biomass is multiplied by a harvest index to represent yield. The exact details are delineated in the original publication [64], but are summarized below:

$$B_{rate} = P \times f(Solar) \times RUE \times f(CO_2) \times f(Temp) \times min(f(Heat), f(Water)) \tag{6.4}$$

$$B_{cumulative,i+1} = B_{cumulative,i} + B_{rate} \tag{6.5}$$

$$Yield = B_{cumulative,maturity} \times HI \tag{6.6}$$

Where B_{rate} and $B_{cumulative}$ is the daily biomass gain and cumulative biomass respectively, and P is the daily radiation into the system.

Agrophotovoltaic theory is built on the analysis of CO_2 limited photosynthesis at high light levels resulting in a light saturation point [65–68] which facilitates dual use of the energy in excess to crop demands. While it would be preferable to use a more representative photosynthesis model to simulate plant growth, this paper presents an agrophotovoltaic

modeling framework and any crop model will serve as a substitute. It is not strictly necessary to undergo the complex studies required for a more accurate photosynthesis model to modify the SIMPLE model given the scope of this framework.

The SIMPLE Crop Model also has a robust air temperature response model, but no extensions are included in this framework to model the specific temperature impacts of agrophotovoltaics for either air or crop temperatures. While the agrophotovoltaic literature suggests there is some impact relating to air temperature at the plant level in the agrophotovoltaic installation [69], previous modeling has shown the overall impact of air temperature differences to not have meaningful impact on plant growth [70] (it is suggested light is the primary driver in any growth differences), particularly if the photovoltaics are sufficiently far from the plants [71] (over 1.5 m). This suggests modeling air temperature dynamics would have a marginal impact on this framework while dramatically increasing computational demands and simulation time, and for this reason is not conducted in this framework.

In addition to the outputs of the model, two additional metrics are added: Light Use Efficiency (LUE) and Water Use Efficiency (WUE).

$$LUE = \frac{Yield}{TLI} \tag{6.7}$$

$$WUE = \frac{Yield}{TWD} \tag{6.8}$$

Where $Yield$ is the total crop yield for the simulated season (which in this case is the system for either the or the reference crop, depending on which step of the simulation is being done), TLI is the sum total light into the system for the simulated season, and TWD is the sum total reference evapotranspiration for the simulated season as described below:

$$\int_{Planting}^{Harvest} P_{crop,daily} dt \tag{6.9}$$

$$\int_{Planting}^{Harvest} ET_o dt \tag{6.10}$$

The purpose of these additional metrics is to facilitate agriculturally focused optimization which allows for improved agricultural performance without strictly requiring increased yields. To support the WUE calculation, water use was also simulated by utilizing the Penman-Monteith equation to calculate daily reference evapotranspiration (ET_o) as described in [72]. ET_o is chosen over ET_c because the SIMPLE Crop Model does not contain a simple method for integrating crop coefficients (K_c values), and K_c values for agrophotovoltaic production are not well developed making the direct calculation of ET_c values difficult and beyond the scope of the framework.

Linking the Light and Crop Model

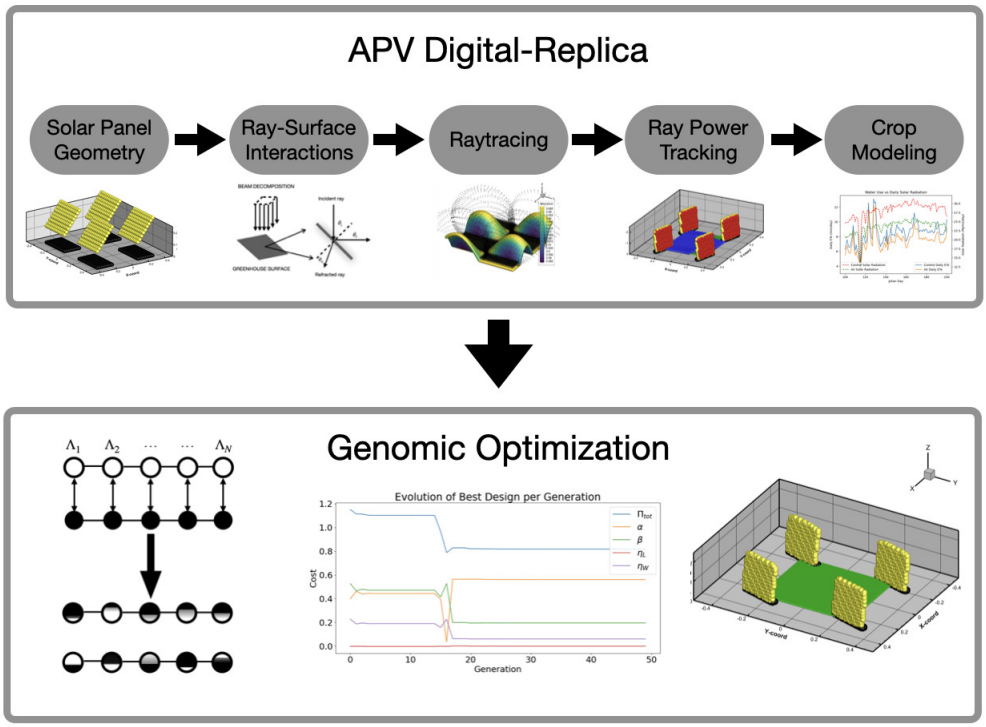

Figure 6.3: Digital-twin and genomic optimization framework.

The framework proposed in this study combines the light simulation model with the crop model in order to optimize the agrophotovoltaic system using crop performance and solar energy production metrics, as seen in the framework diagram in Figure 6.3. First, the light model is run to obtain the solar panel power absorption and ground surface power absorption. Daily radiation values obtained through the light-based simulation are then passed into the crop model which calculates the reference and agrophotovoltaic crop yield via the SIMPLE model. The crop model then outputs agrophotovoltaic and reference crop yields as well as other crop performance metrics discussed earlier. The entire framework has been built in Python 3.9 with only `numpy` and `pysolar` external packages. The main program with system parameters, the light model, and the genetic algorithm calls the crop model in a secondary program. The light model simulates the sun's position for the crop season and calculates average ground radiation ($\frac{W}{m^2}$), which is then passed onto the crop model to calculate the crop biomass, evapotranspiration, water, and light use for a given agrophotovoltaic design. This routine is repeated for each agrophotovoltaic design in the genetic optimizer in each generation to calculate the design fitness, rank designs, and use evolutionary principles to retain the best performers. Currently, the code uses manually inputted system parameters (i.e. weather data, crop type, solar panel properties, etc.) to optimize the design, although

it is possible to develop a GUI for crop growers to use this framework for their own choice of crops, solar panels, and location in future extensions.

6.3 Genomic Optimization Framework

Design Parameters

The system design is defined by the following variables:

$$\mathbf{\Lambda}^i \equiv \{\Lambda_1^i, ..., \Lambda_N^i\} \equiv \{\theta_2, \theta_3, \hat{n}_s, \hat{n}_g, h_0, R_2, R_3, p_1, p_2, p_3\} \tag{6.11}$$

where $\hat{n}_s$ and $\hat{n}_g$ are the refractive indices of the solar panels and the ground, R_2 and R_3 are generalized radii of the solar panels, θ_2 and θ_3 are the solar panel rotation around $\boldsymbol{e}_2$ and $\boldsymbol{e}_3$ axes, p_1, p_2, and p_3 are the geometric exponents. The thickness of the solar panel, R_1, and the rotation around $\boldsymbol{e}_1$ are kept constant. The rotation of solar panels around all three axes is not practical since the panels only need to adjust for the sun altitude and azimuth angles. While only stationary panels are considered for this study, solar tracking panels can be implemented by having one altitude and azimuth angle pair per day as part of the design variables. The design parameters in $\mathbf{\Lambda}^i$ can be chosen within user-specified bounds.

Design Fitness

The "fitness" or cost associated with a given agrophotovoltaic system design is determined by a custom cost function. A good agrophotovoltaic design will appropriately distribute incoming sunlight between the solar panels and the ground. However, the ground energy absorption does not fully represent the crop performance. Therefore, the crop yield from the agrophotovoltaic system needs to be comparable to the reference crop yield, which is independently calculated using the same ambient parameters but without the solar panels on the field. The following cost function is proposed to evaluate the agrophotovoltaic system performance:

$$\Pi = w_1\alpha + w_2\beta + w_3\eta_L + w_4\eta_W \tag{6.12}$$

where are defined by the following equations:

$$\alpha = \frac{P_{ref} - P_{solar}}{P_{ref}} \tag{6.13}$$

$$\beta = \frac{Y_{ref} - Y_{APV}}{Y_{ref}} \tag{6.14}$$

$$\eta_L = \frac{LUE_{ref} - LUE_{APV}}{LUE_{ref}} \tag{6.15}$$

$$\eta_W = \frac{WUE_{ref} - WUE_{APV}}{WUE_{ref}} \tag{6.16}$$

where the weights can be chosen by the user to prioritize agriculture, solar power generation, etc. The lack of an absolute value function on the agricultural cost parameters enables the optimizer to generate designs that can exceed the reference crop performance in terms of the individual cost parameters, as demonstrated in a 2017 German potato crop [73] where yields exceeded the reference yield. While this is a single example, and the SIMPLE crop model cannot strictly replicate this performance, there is the theoretical possibility of a more complicated crop model outputting improved yields compared to the reference crop. As such, this framework allows for the possibility of improved yields, even if only theoretical, to incentivize high crop yields in the designs. Note that all the cost parameters are non-dimensional and normalized.

Constraints

There are many critical constraints when considering design, however, two important ones identified in the literature are considered in this framework:

1. Agrophotovoltaics should focus on supporting agricultural production and should have a constraint that minimizes the negative impacts of shading on crop yield [74–76],

2. Agrophotovoltaic land use should not excessively compromise agricultural or photovoltaic production and should have a constraint ensuring the combined land equivalent ratio of agricultural and photovoltaic production is greater than single use of the land for either type of production to ensure any production compromises ultimately yield a net gain to the efficiency of the land use [77–80].

These two constraints are selected as they well represent the desire for agrophotovoltaics to provide value centered around agriculture, and can be mathematically described with the following equations:

$$\frac{Y_{APV}}{Y_{ref}} \geq \delta \tag{6.17}$$

$$\frac{Y_{APV}}{Y_{ref}} + \frac{P_{solar}}{P_{ref}} \geq 1 \tag{6.18}$$

where Y_{ref} refers to the reference crop yield (no solar panels on field), P_{ref} refers to the reference solar energy generation (no crops) and δ refers to the percent of acceptable loss of crop yield related to installing agrophotovoltaics. Because these constraints need to be enforced on the cost parameters rather than the design parameters, the design space cannot be limited to acceptable designs *a priori*. One option is to enforce *soft constraints* to the system by including penalty terms in the cost function with very large weights to eliminate

designs that do not abide by the constraints during the design evaluation process of the genomic optimization framework. The modified cost function can be written as:

$$\Pi = w_1\alpha + w_2\beta + w_3\eta_L + w_4\eta_W + P_1 + P_2 \tag{6.19}$$

where,

$$P_1 = \begin{cases} 10000 & \text{for} \quad \frac{Y_{APV}}{Y_{ref}} < \delta \\ 0 & \text{for} \quad \frac{Y_{APV}}{Y_{ref}} \geq \delta \end{cases} \tag{6.20}$$

$$P_2 = \begin{cases} 10000 & \text{for} \quad \frac{Y_{APV}}{Y_{ref}} + \frac{P_{solar}}{P_{ref}} < 1 \\ 0 & \text{for} \quad \frac{Y_{APV}}{Y_{ref}} + \frac{P_{solar}}{P_{ref}} \geq 1 \end{cases} \tag{6.21}$$

Given the cost function, the system can be optimized using the genetic algorithm described in Section 2.

6.4 Numerical Example

A numerical example is generated using the light model parameters in Table 6.1, and the optimization parameters in Table 6.3. An entire season was simulated with the crop model using weather data from a California Irrigation Management Information System weather station [81] located in Davis, California (38.53 N, 121.77 W) from April 10, 2021 to July 19, 2021. The crop model was run using settings in Table 6.2 to simulate SunnySD tomatoes for every day and hour in the aforementioned season where the altitude of the sun was above the horizon. The ground refractive index was made a variable to simulate various planting densities. The simulated agrophotovoltaic field has been rescaled to be of unit size to allow for a smaller number of rays to be used for the light model. Lastly, the reference solar power for the agrophotovoltaic constraint was calculated by running the genomic optimizer to maximize solely the solar power generation.

Table 6.1: Light Model Parameters

Symbol	Type	Units	Value	Description
N_r	scalar	none	196	Number of light rays
c	scalar	m/s	3×10^8	Speed of light
R_1	scalar	m	0.02	Solar panel thickness
n_{panel}	scalar	none	4	Number of solar panels

Table 6.2: Crop Model Parameters

Symbol	Units	Value	Description
Crop	none	Tomato	Crop species
Cultivar	none	SunnySD	Specific crop variety
T_{sum}	$^{\circ}C$ day	2800	Cumulative temperature requirement from sowing to maturity
HI	none	0.68	Harvest index (*i.e.* percent of harvestable biomass)
I_{50A}	$^{\circ}C$ day	520	Cumulative temperature requirement for leaf area development to intercept 50% of radiation
I_{50B}	$^{\circ}C$ day	900	Cumulative temperature till maturity to reach 50% radiation interception due to leaf senescence
I_{50maxH}	$^{\circ}C$ day	100	Maximum daily reduction in I_{50B} due to heat stress
I_{50maxW}	$^{\circ}C$ day	5	Maximum daily reduction in I_{50B} due to drought stress
T_{base}	$^{\circ}C$	6	Base temperature for phenology development and growth
$T_{optimal}$	$^{\circ}C$	26	Optimal temperature for biomass growth
T_{max}	$^{\circ}C$	32	Threshold temperature to start accelerating senescence from heat stress
$T_{extreme}$	$^{\circ}C$	45	The extreme temperature threshold when RUE becomes 0 due to heat stress
RUE	$\frac{g}{MJ*m^2}$	1	Radiation use efficiency (above ground only and without respiration)
S_{CO_2}	none	0.07	Relative increase in RUE per ppm elevated CO2 above 350 ppm
S_{water}	none	2.5	Sensitivity of RUE (or harvest index) to drought stress (ARID index)
δ	none	0.66	ratio of yield to reference yield (see eq. 6.17)

These parameters were selected based on the values given in [64] with the only modification being to the I_{50B} term to generate a senescence more in line with expected crop behavior.

This study presents a framework for crop-driven agrophotovoltaic optimization rather than searching for the "true" optimal solution. Thus, the agrophotovoltaic design is optimized for 20 design strings in the population and 50 generations of genomic optimization. The agrophotovoltaic design includes the altitude and azimuth angles, solar panel and ground

refractive index, solar panel height, size, and shape.

Table 6.3: Genomic Optimization Parameters

Symbol	Units	Value	Description
parents	none	6	Surviving strings for breeding
S	none	20	Designs per generation
G	none	50	Total generations
$[\theta_2^-, \theta_2^+]$	degrees	$[-\pi/2, \pi/2]$	Solar panel altitude angle
$[\theta_3^-, \theta_3^+]$	degrees	$[-\pi, \pi]$	Solar panel azimuth angle
$[\hat{n}^-, \hat{n}^+]$	none	[1,100]	Solar panel refractive index
$[h_0^-, h_0^+]$	none	[0.05,0.15]	Solar panel height
$[R_{2\ or\ 3}^-, R_{2\ or\ 3}^+]$	none	$[0.0125, 0.125]$	Generalized radii
$[p_{1\ or\ 2\ or\ 3}^-, p_{1\ or\ 2\ or\ 3}^+]$	none	$[1, 20]$	Geometric exponent
w_1	none	1	Weight of solar panel power in net cost
w_2	none	1	Weight of crop yield in net cost
w_3	none	1	Weight of light use efficiency in net cost
w_4	none	1	Weight of water use efficiency in net cost
P_{ref}	W	83.51	Reference solar power
Y_{ref}	$\frac{tons}{acre}$	1.7	Reference crop yield
LUE_{ref}	$\frac{tons}{acre}/\frac{MJ}{season}$	0.0006	Reference light use efficiency
WUE_{ref}	$\frac{tons}{acre}/\frac{mm}{season}$	0.002	Reference water use efficiency

The evolution of the design total cost per generation can be seen in Figure 6.4 over 50

generations of optimization. The design and cost parameters associated with the optimal agrophotovoltaic design are tabulated in Table 6.4.

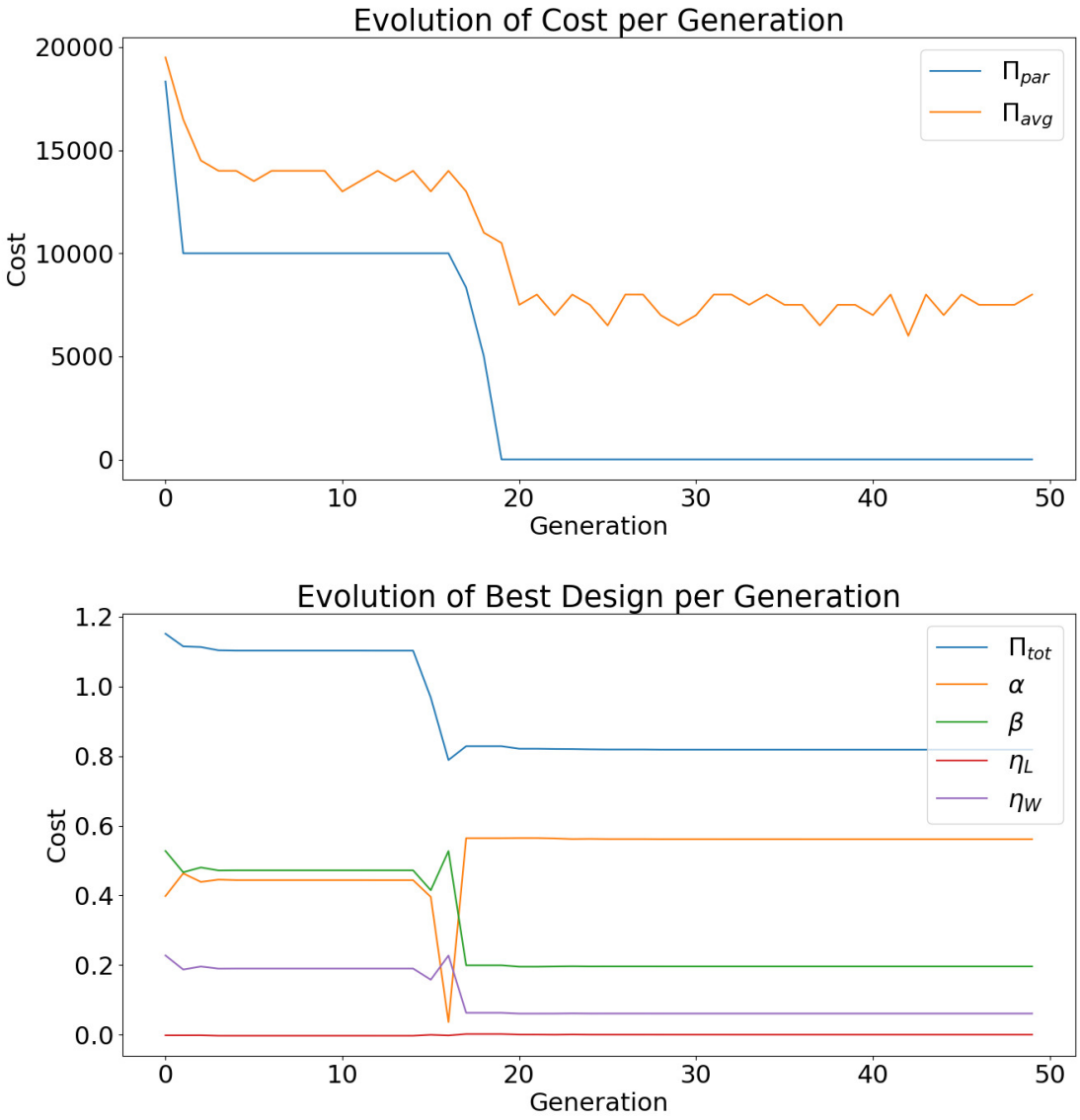

Figure 6.4: Evolution of total cost Π and individual cost parameters. Top: Average cost evolution of parent and overall population. Bottom: Individual cost parameter and best design cost (excluding penalty terms) evolution.

Table 6.4: Optimal Agrophotovoltaic Design Parameters for the Numerical Example

$\mathbf{\Pi}$	α	β	η_L	η_W	θ_2	θ_3	$\hat{n}_s$
0.818	0.561	0.196	0.0	0.061	-0.154	0.344	60.64
$\hat{n}_g$	h_0	R_2	R_3	p_1	p_2	p_3	
1.20	0.094	0.103	0.093	18.24	8.80	13.64	

The "optimal" design parameters obtained through the genomic optimization scheme are used to visualize the agrophotovoltaic design, seen in Figure 6.5.

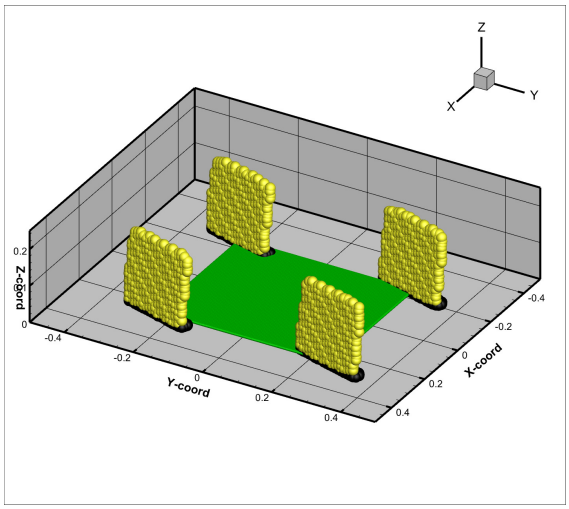

(a) Isometric view of optimized APV design.

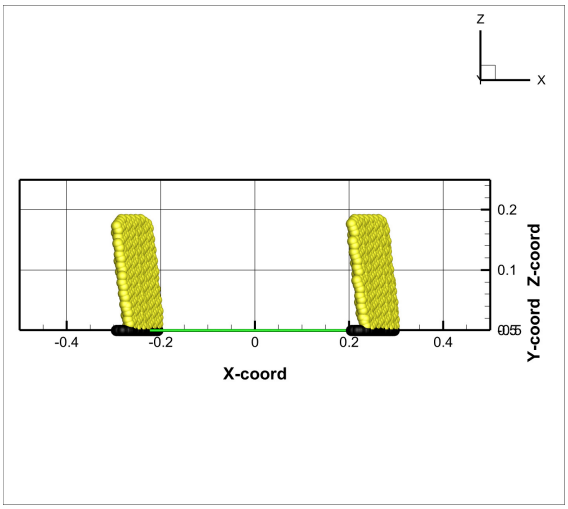

(b) Side view of optimized APV design.

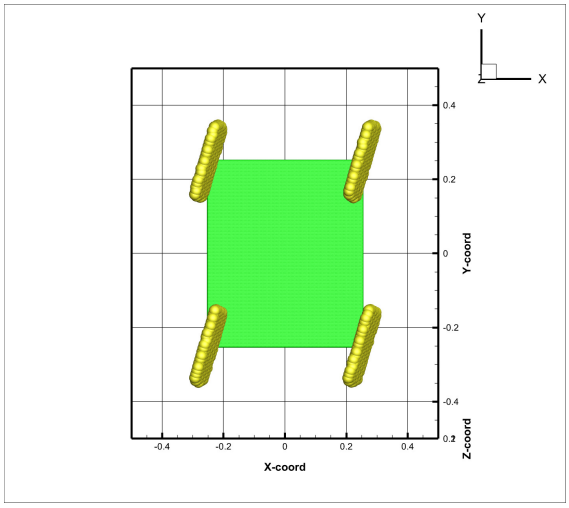

(c) Top view of optimized APV design.

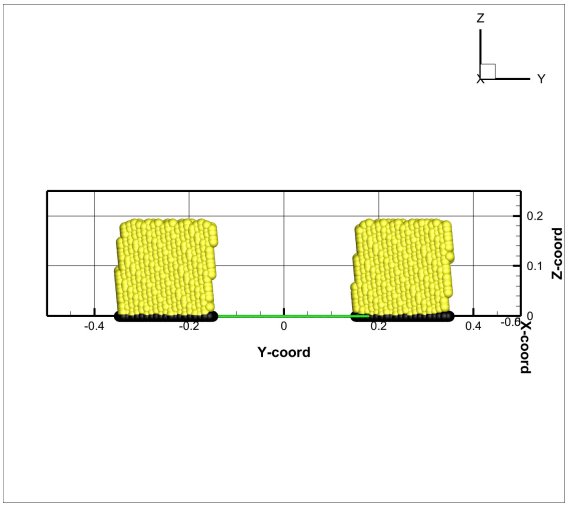

(d) Front view of optimized APV design.

Figure 6.5: Detailed views of optimized APV design where yellow indicates the solar panels and green represents the agricultural area.

An example of a single light pulse traveling through the medium and interacting with the surfaces is visualized using snapshots of the simulation, shown in Figure 6.6. It is important to keep in mind that these light pulse simulations are done hourly for the number of days the crop is simulated. We can see that the "optimal" design places the relatively reflective ($n \approx 60$) solar panels with an altitude of 81° and azimuth angle of 290° (converting θ_3 to the azimuth angle using $\phi_{azimuth} = \theta_3 \times \frac{180}{\pi} - 90°$), which results in sunlight reflecting off the panels and hitting the crops at lower solar angles.

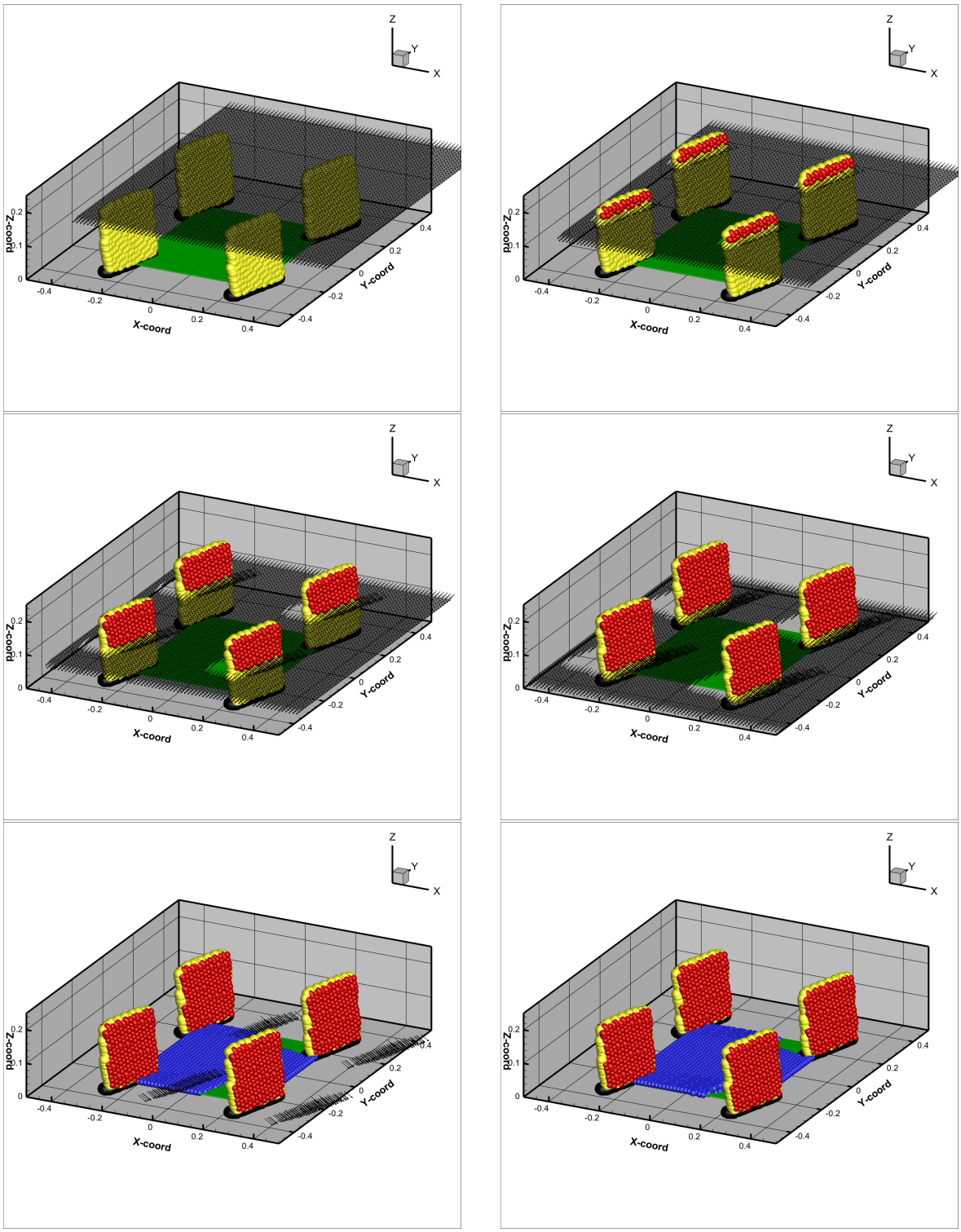

Figure 6.6: Raytracing of a single light pulse. The incoming light is discretized into rays which reflect off the solar panels (shown in yellow) and hit the ground (shown in green). Solar energy is absorbed by the solar panels, at locations marked as red dots and by the ground, at locations marked as blue dots.

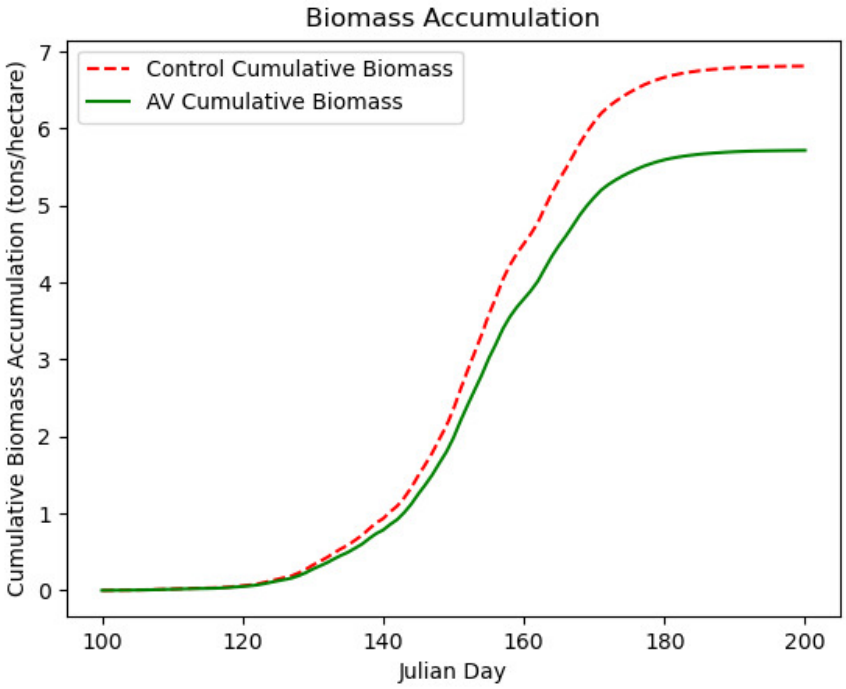

(a) Cumulative biomass for control and crops.

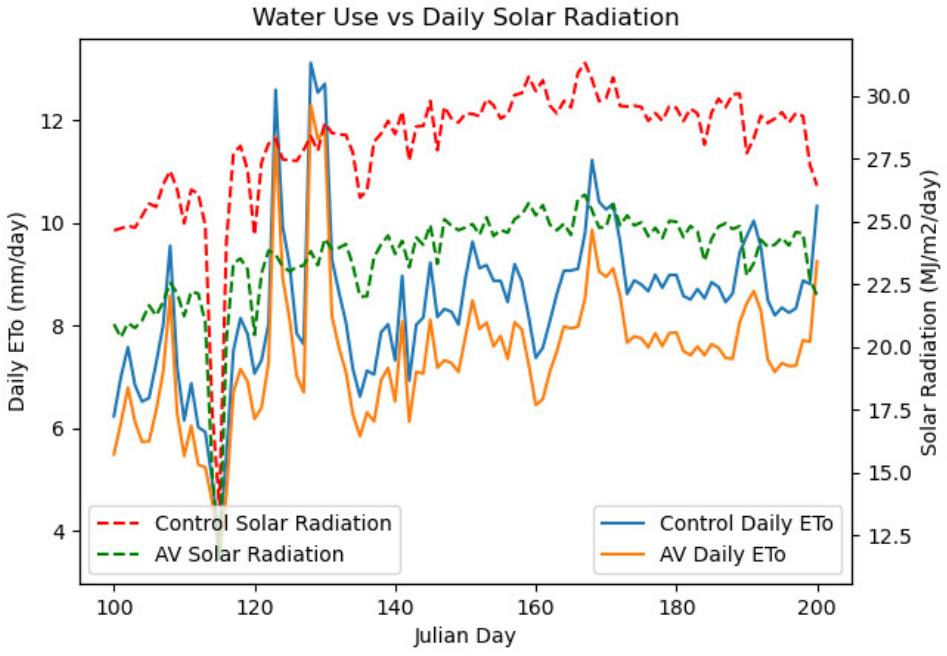

(b) Daily ETo compared with daily solar radiation.

Figure 6.7: Crop model outputs.

For any simulated crop design, a variety of different outputs are available for analysis within this framework. Outputs relating to crop growth, water use and light are shown in Figure 6.7. From the analysis of these graphs and related data, the crop performance of an agrophotovoltaic crop can be compared to a reference crop. These results are discussed in the next section.

6.5 Discussion

The optimized agrophotovoltaic design can be analyzed through the individual cost parameters that form the total cost. It can be seen that the best design has avoided violating the critical agrophotovoltaic constraints regarding the crop yield and solar power generation limits and incurring the large penalty terms described in Section 3. The genetic algorithm is conducting a global search within the design space and was able to obtain the presented lowest cost. Once there are designs that satisfy the soft constraints (i.e. negating the penalty costs), the genetic algorithm continues to reduce the cost by minimizing the individual cost parameters $(\alpha, \beta, \eta_L, \eta_W)$ as much as possible. Only a limited number of designs satisfies these agricultural constraints and reduces the cost further. The restrictions imposed by these constraints limit the design space which is the reason the cost can not be reduced beyond a certain number of generations.

The robustness of the genetic algorithm was tested by using different seeds in the random number generator for initializing the design population and got similar optimization results. The top plot in Figure 6.4 displays the parent cost for individual cost parameters which is expected to show a monotonically decreasing behavior while the average design cost is seen to be zig-zagy, which is due to random designs added to the population in each generation.

It is seen that the best agrophotovoltaic design after 50 generations employs highly reflective near-vertical panels that reflect sunlight for crop production while still generating solar power. This is in line with the genomic optimization setup where a minimum requirement on crop production was enforced by the use of a penalty term for the crop yield cost parameter.

These results of nearly vertical panels are interesting as they are counter-intuitive to the theory of agrophotovoltaic production discussed earlier where light during the most radiation-dense part of the day should be reduced to below the light saturation point. However, vertical panels match the findings of a similar design methodology [82] in Sweden which is driven more by photovoltaic performance relative to this work's crop-focused methodology. This finding is likely related to two particular limitations of this crop model: 1) a constant value is used for converting light into biomass (RUE) meaning a linear response between light and growth, and 2) the daily timestep used in the crop model does not characterize the time-sensitive responses to shading and photosynthesis and it appears designs which maximize light when light is most dense (i.e. the afternoon) are preferred as the timing of the energy makes no difference in this implementation. This highlights the need for specific agrophotovoltaic crop models to be developed. Resolving these challenges are beyond the scope of this study, but

the power of the framework presented allows for this modification to be made once more research is conducted into agrophotovoltaic crop modeling.

The cost reduction after 50 generations was determined to be 28.9% for the best design (excluding penalty terms) and 59.0% for the average design, meaning the design space was restricted to the design subspace that satisfied the agrophotovoltaic constraints. The crop performance as modeled was found to be 1.70 $\frac{tons}{acre}$ for the reference versus 1.43 $\frac{tons}{acre}$ for the agrophotovoltaic, representing an 18% loss of yield, which is less than the 34% loss acceptable in the design framework. The reference crop ET_O was calculated to be 853 mm of water for the season compared to 751 mm of water for the agrophotovoltaic, representing about a 12% decrease in reference evapotranspiration.

6.6 Summary

Agrophotovoltaic systems are rapidly developing as a solution to the land competition between agriculture and solar power generation. There have been several modeling approaches that integrate the dynamics of the agrophotovoltaic system to predict crop performance and power generation. Optimization through such high-fidelity models requires immense computational power. Instead, an alternative framework with a reduced-order order digital-twin is used in tandem with a genomic optimization scheme to find optimal agrophotovoltaic designs. The proposed framework would help justify investment in photovoltaic arrays over agricultural settings in a way that benefits crop production using genomic multi-objective optimization to simulate the impact of photovoltaic panels on the crop environment, the subsequent crop response, and solar power generation.

Overall, this framework demonstrates the potential to link light modeling with crop modeling to simulate agrophotovoltaic performance. Although the proposed digital-twin has limitations on crop model and raytracing accuracy, it provides a foundational framework that utilizes a physics-driven optimization approach for agrophotovoltaics.

This model can be extended to include thermal modeling of the system, wavelength-specific raytracing, and a more advanced crop model to further increase the accuracy of the digital-twin. Ultimately, a validated and refined digital-twin can be used to design and test agrophotovoltaic configurations for a given crop, location, and desired power generation before the real-life version is built.

The coupling of the optical model developed in this study with a crop model concludes the simulation and optimization framework presented in this dissertation. We will go over key findings and extensions of the proposed framework in the next chapter.

Chapter 7

Conclusions

The goal of this study is to analyze next-generation food systems from an optical modeling standpoint. We have developed a reduced-order geometric raytracing model to evaluate the performance of various food production systems, namely solar greenhouses, open-field agrophotovoltaics, and indoor pod farming systems. A digital-twin approach, where a digital replica of the physical system is modeled, is used to quickly and efficiently evaluate designs and optimize them using a genomic-based optimization algorithm. The digital-twin consists of modeling the optical properties of the system to accurately simulate the power distribution within the food systems through the raytracing algorithm. In addition, power sizing of a real-life indoor farming system is performed. Extensions of the digital-twin framework and how it can be coupled with other physics models are provided using a crop performance driven optimization case study of an open-field agrophotovoltaic system.

The initial solar greenhouse digital-twin framework developed in this project certainly has its limitations in terms of its accuracy and speed. While the solar energy production and photosynthesis are closely tied to the amount of sunlight absorbed, it is known that there are other factors such as water stress on plants, optimal temperature for solar panel operation, etc. that affect the efficiency of these processes beyond the values provided in literature for when there are ideal conditions. In addition, the resulting greenhouse shape can also be evaluated in terms of the cost-to-build and ease-of-build. Since the greenhouse takes any shape within the design space of the ellipsoidal and sinusoidal terms that constitute the greenhouse geometry, a cost parameter that penalizes a design for being hard to build or expensive to build will enable the genomic optimization scheme to favor easier-to-build designs for the user. Next, we have expanded the model capabilities to include a simple irrigation model. This expension included equipping the solar greenhouse raytracing model with hydroponics by modeling the optical properties of the hydroponic nutrient delivery system and the power requirements of the hydroponics. This framework has the flexibility to seamlessly incorporate additional multiphysics models, such as those related to crops, heat, and ventilation. The enhanced framework proves to be a valuable asset, serving as a tool to optimize real-world systems and curtail the financial expenses associated with experimental testing of system designs.

This system captures the essential physics in a computationally efficient manner. However, there are many improvements to the model presented. For example, this work can be extended to include detailed solar panel translucency analysis, which includes exploring the wavelength-specific nature of photosynthesis, which occurs when the plant receives a sunlight in a certain wavelength range called photosynthetically active radiation (PAR). Using solar cells that utilize this fact can be deployed for the greenhouse system where the solar panels would absorb certain wavelengths of light - this requires extending the light-scattering simulation described in this project to include a wavelength-specific power and ray tracking algorithm. As mentioned earlier, solar panel translucency is directly tied to the photosynthetically active radiation a plant needs, which will ultimately influence the optimal solar-cell design for a specific plant to be grown in a self-sufficient greenhouse.

The optimization framework used in this project is adequate for the given system, but it should be noted that any increase in the computational cost of the greenhouse simulation will result in a larger increase in the runtime of the genomic optimization scheme. Therefore, alternative machine-learning algorithms (i.e. artificial neural networks (ANN)) can be utilized to circumvent this issue, where the optimization of the system can take place without running an extensive physical simulation of the system and allow us to test more designs within our design space.

Overall, the greenhouse digital-twin framework developed can be both used to assess the performance of a greenhouse system, as well as find the optimal greenhouse design for specific system parameters. The digital-twin can used as design tool that can be deployed for customers that plan on building a solar greenhouse with specific objectives, whether it is to maximize crop yield or maximize solar energy production, etc. Indoor agricultural production integrated with solar energy production has a potential to alleviate the energy and food demands of the world and machine-learning can help us achieve that, as seen in this study.

Then, we moved onto another innovative food production system, indoor pod farming, to demonstrate the capabilities of our reduced-order geometric raytracing algorithm and genomic optimization framework. Indoor farming emerges as a promising frontier in the evolution of agriculture, presenting various advantages like continuous crop cultivation, decreased transportation expenses, and the possibility of urban farming. Nevertheless, these systems grapple with energy consumption challenges, and there exists a scarcity of comprehensive quantitative analyses gauging their overall efficiency. To address this gap, we introduced a digital-twin model of the optical design of an indoor farming pod, where the LED lighting system parameters are able to be optimized for maximum plant power absorption using the proposed genomic optimization framework. The suggested digital-twin and optimization framework lays the groundwork by adopting a physics-driven approach to optimize energy flow, thereby paving the path for the implementation of more sustainable practices in indoor farming.

The proposed modeling framework captures the overall optical characteristics of an indoor farming system, however, it can be connected to other multiphysics simulations such as heating, ventilation, irrigation, and crop models to form a complete digital-twin of the

system. However, this study sets the foundation for implementing such models by providing the solar/optical power absorption characteristics of these systems. Possible improvements to this model include adjusting the design objectives via cost function design and incorporate constraints via parameter search bounds. Extending the framework to include wavelength-specific power flow, similar to the greenhouse digital-twin extensions mentioned above, could further improve predictions of energy efficiency and crop yield by providing each plant with its ideal lighting conditions. Such refined models can serve as valuable tools for testing and estimating how a particular design would perform in the real world, enabling farmers to make informed decisions and effectively optimize their own indoor farming setups.

We then analyzed an indoor farming system in terms of power requirements and energy storage. The indoor farming pod used in this example was based on a real-life indoor farming container situated in Richmond Field Station in Berkeley, California, run by the University of California, Berkeley and AI Institute for Next Generation Food Systems (AIFS). Given the container size and the equipment needed to operate the pod, we assessed the power requirements of the system on a day-to-day basis. While the calculations performed simplify the power analysis of the real-life indoor farming system, this can provide a useful tool in evaluating the feasibility of using on-site renewable energy sources to power the next-generation food systems.

Lastly, we looked at extensions for the light-based simulation methods developed within this dissertation. The proposed extension was to form a multiphysics model of an open-field agrophotovoltaic system by connecting the raytracing algorithm to an external experimental crop model to simulate the growth conditions of crops in a given agrophotovoltaic setup. This alternative framework with a reduced order digital-twin is used in tandem with a genomic optimization scheme to find optimal agrophotovoltaic designs. The proposed framework would help justify investment in photovoltaic arrays over agricultural settings in a way that benefits crop production using genomic multi-objective optimization to simulate the impact of photovoltaic panels on the crop environment, the subsequent crop response, and solar power generation. Overall, this framework demonstrates potential to link light modeling with crop modeling to simulate agrophotovoltaic performance. Although the proposed digital replica has limitations on crop model and raytracing accuracy, it provides a foundational framework that utilizes a physics-driven optimization approach for agrophotovoltaics. This model can again be extended to include thermal modeling of the system, wavelength-specific raytracing, and a more advanced crop model to further increase the accuracy of the digital-twin. Ultimately, a validated and refined digital replica can be used to design and test agrophotovoltaic configurations for a given crop, location, and desired power generation before the real-life version is built.

In conclusion, this dissertation aims to provide insight to next-generation food systems through the lens of optical modeling. The devised geometric raytracing model is used to assess the efficacy of the food production systems with given numerical examples, namely solar greenhouses, open-field agrophotovoltaics, and indoor pod farming systems. Employing a digital-twin methodology, which involves creating a digital replica of the physical system, we swiftly and efficiently assess designs and optimize them using a genomic-based optimization

algorithm. The digital-twin encompasses the modeling of optical properties within the system, facilitating accurate power distribution simulations through the raytracing algorithm. I hope that this computational framework and optimization scheme provide a foundation for understanding, evaluating, and optimizing the food systems of the future and prove a useful tool to efficiently and sustainably produce food and generate power, driven by innovation and cutting-edge technology.

Bibliography

[1] California Department of Conservation. *Williamson Act Program.* URL: https://www.conservation.ca.gov/dlrp/wa.

[2] California Air Resources Board. *CARB releases ambitious draft climate action plan to slash use of fossil fuels and reach carbon neutrality by 2045.* URL: https://ww2.arb.ca.gov/news/carb-releases-ambitious-draft-climate-action-plan-slash-use-fossil-fuels-and-reach-carbon.

[3] M. Beck et al. "Combining PV and food crops to Agrophotovoltaic–optimization of orientation and harvest". In: *EUPVSEC proceedings* 1 (2012).

[4] S. Schindele et al. "Implementation of agrophotovoltaics: Techno-economic analysis of the price-performance ratio and its policy implications". In: *Applied Energy* 265 (2020), p. 114737. ISSN: 0306-2619. DOI: https://doi.org/10.1016/j.apenergy.2020.114737. URL: https://www.sciencedirect.com/science/article/pii/S030626192030249X.

[5] A. Weselek et al. "Agrophotovoltaic systems: applications, challenges, and opportunities. A review". In: *Agronomy for sustainable development* 39.4 (2019), pp. 1–20.

[6] R. H. E. Hassanien, M. Li, and W. Dong Lin. "Advanced applications of solar energy in agricultural greenhouses". In: *Renewable and Sustainable Energy Reviews* 54 (2016), pp. 989–1001. ISSN: 1364-0321. DOI: https://doi.org/10.1016/j.rser.2015.10.095. URL: https://www.sciencedirect.com/science/article/pii/S1364032115011740.

[7] M. E. Loik et al. "Wavelength-selective solar photovoltaic systems: Powering greenhouses for plant growth at the food-energy-water nexus". In: *Earth's Future* 5.10 (2017), pp. 1044–1053. DOI: 10.1002/2016ef000531.

[8] K. Ezzaeri et al. "The effect of photovoltaic panels on the microclimate and on the tomato production under photovoltaic canarian greenhouses". In: *Solar Energy* 173 (2018), pp. 1126–1134. ISSN: 0038-092X. DOI: https://doi.org/10.1016/j.solener.2018.08.043. URL: https://www.sciencedirect.com/science/article/pii/S0038092X18308132.

[9] M. Cossu et al. "An algorithm for the calculation of the light distribution in photovoltaic greenhouses". In: *Solar Energy* 141 (2017), pp. 38–48. ISSN: 0038-092X. DOI: https://doi.org/10.1016/j.solener.2016.11.024. URL: https://www.sciencedirect.com/science/article/pii/S0038092X16305564.

[10] Z. Nakoul et al. "Optimization of a Solar Photovoltaic Applied to Greenhouses". In: *Physics Procedia* 55 (2014). 8th International Conference on Material Sciences, CSM8-ISM5, pp. 383–389. ISSN: 1875-3892. DOI: https://doi.org/10.1016/j.phpro.2014.07.055. URL: https://www.sciencedirect.com/science/article/pii/S1875389214001175.

[11] S. Khan, A. Purohit, and N. Vadsaria. "Hydroponics: current and future state of the art in farming". In: *Journal of Plant Nutrition* 44 (10 2020), pp. 1515–1538. ISSN: 15324087. DOI: 10.1080/01904167.2020.1860217.

[12] R. S. Velazquez-Gonzalez et al. "A Review on Hydroponics and the Technologies Associated for Medium-and Small-Scale Operations". In: *Agriculture (Switzerland)* 12 (5 May 2022). ISSN: 20770472. DOI: 10.3390/agriculture12050646.

[13] A. Fussy and J. Papenbrock. "An Overview of Soil and Soilless Cultivation Techniques—Chances, Challenges and the Neglected Question of Sustainability". In: *Plants* 11 (9 May 2022). ISSN: 22237747. DOI: 10.3390/plants11091153.

[14] B. M. Eldridge et al. "Getting to the roots of aeroponic indoor farming". In: *New Phytologist* 228 (4 Nov. 2020), pp. 1183–1192. ISSN: 14698137. DOI: 10.1111/nph.16780.

[15] G. Niu and J. Masabni. *Hydroponics*. Elsevier, 2022, pp. 153–166. DOI: 10.1016/B978-0-323-85152-7.00023-9.

[16] N. Sharma et al. "Hydroponics as an advanced technique for vegetable production: An overview". In: *Journal of Soil and Water Conservation* 17 (4 2018), p. 364. ISSN: 0022-457X. DOI: 10.5958/2455-7145.2018.00056.5.

[17] S. V. Souza, R. M. T. Gimenes, and E. Binotto. "Economic viability for deploying hydroponic system in emerging countries: A differentiated risk adjustment proposal". In: *Land Use Policy* 83 (Apr. 2019), pp. 357–369. ISSN: 02648377. DOI: 10.1016/j.landusepol.2019.02.020.

[18] *Aeroponics versus Conventional Hydroponics — agrotonomy.com*. https://agrotonomy.com/aeroponics-versus-conventional-hydroponics/. [Accessed 07-10-2023].

[19] R. S. Isied, E. Mengi, and T. I. Zohdi. "A digital-twin framework for genomic-based optimization of an agrophotovoltaic greenhouse system". In: *Proceedings of the Royal Society A: Mathematical, Physical and Engineering Sciences* 478.2267 (2022). DOI: 10.1098/rspa.2022.0414.

[20] L. La Notte et al. "Hybrid and organic photovoltaics for greenhouse applications". In: *Applied Energy* 278 (2020), p. 115582. ISSN: 0306-2619. DOI: https://doi.org/10.1016/j.apenergy.2020.115582. URL: https://www.sciencedirect.com/science/article/pii/S030626192031093X.

[21] T. Zohdi. "A digital-twin and machine-learning framework for the design of multiobjective agrophotovoltaic solar farms". In: *Computational Mechanics* 68.2 (2021), pp. 357–370.

[22] B. Stafford. *pysolar (0.9)*. 2020. DOI: https://doi.org/10.5281/zenodo.5518074.

[23] S. Jacquemoud and F. Baret. "PROSPECT: A model of leaf optical properties spectra". In: *Remote Sensing of Environment* 34 (1990), pp. 75–91.

[24] *What Size Greenhouse Do I Need? — advancingalternatives.com*. https://www.advancingalternatives.com/blog/greenhouse-tips-size-greenhouse-need/. [Accessed 11-10-2023].

[25] NoSoilSolutions. *A Simple Guide To Hydroponic Plant Spacing - NoSoilSolutions — nosoilsolutions.com*. https://www.nosoilsolutions.com/simple-guide-hydroponic-plant-spacing/. [Accessed 11-10-2023].

[26] E. van Os, T. H. Gieling, and J. H. Lieth. "Chapter 13 - Technical Equipment in Soilless Production Systems". In: *Soilless Culture (Second Edition)*. Ed. by M. Raviv, J. H. Lieth, and A. Bar-Tal. Second Edition. Boston: Elsevier, 2019, pp. 587–635. ISBN: 978-0-444-63696-6. DOI: https://doi.org/10.1016/B978-0-444-63696-6.00013-X. URL: https://www.sciencedirect.com/science/article/pii/B978044463696600013X.

[27] *Hydroponic Pumps: What You Need to Know — agrowtronics.com*. https://www.agrowtronics.com/sizing-hydroponic-pumps-what-you-need-to-know/. [Accessed 11-10-2023].

[28] E. Mengi et al. "A digital-twin and rapid optimization framework for optical design of Indoor Farming Systems". In: *Computational Mechanics* (2023). DOI: 10.1007/s00466-023-02421-9.

[29] C. A. Mitchell. "History of Controlled Environment Horticulture: Indoor Farming and Its Key Technologies". In: *HortScience* 57 (2 Feb. 2022), pp. 247–256. ISSN: 0018-5345. DOI: 10.21273/HORTSCI16159-21.

[30] P. J. Kramer, H. Hellmers, and R. J. Downs. "SEPEL: New Phytotrons for Environmental Research". In: *BioScience* 20 (22 Nov. 1970), pp. 1201–1208. ISSN: 00063568. DOI: 10.2307/1295626.

[31] T. Kozai. *Smart Plant Factory*. Ed. by T. Kozai. Springer Singapore, 2018. ISBN: 978-981-13-1064-5. DOI: 10.1007/978-981-13-1065-2.

[32] "Freight Farms". URL: https://www.freightfarms.com/home/.

[33] A. M. Beacham, L. H. Vickers, and J. M. Monaghan. "Vertical farming: a summary of approaches to growing skywards". In: *Journal of Horticultural Science and Biotechnology* 94 (3 May 2019), pp. 277–283. ISSN: 14620316. DOI: 10.1080/14620316.2019.1574214.

[34] K. Al-Kodmany. "The vertical farm: A review of developments and implications for the vertical city". In: *Buildings* 8 (2 Feb. 2018). ISSN: 20755309. DOI: 10.3390/buildings8020024.

[35] G. D. Massa et al. "Plant Productivity in Response to LED Lighting". In: *HortScience* 43 (7 Dec. 2008), pp. 1951–1956. ISSN: 0018-5345. DOI: 10.21273/HORTSCI.43.7.1951.

[36] T. Zohdi. "Rapid simulation of viral decontamination efficacy with UV irradiation". In: *Computer Methods in Applied Mechanics and Engineering* 369 (2020), p. 113216. DOI: https://doi.org/10.1016/j.cma.2020.113216.

[37] T. Zohdi. "A machine-learning digital-twin for rapid large-scale solar-thermal energy system design". In: *Computer Methods in Applied Mechanics and Engineering* 412 (July 2023), p. 115991. ISSN: 00457825. DOI: 10.1016/j.cma.2023.115991.

[38] T. I. Zohdi. "An adaptive digital framework for energy management of complex multi-device systems". In: *Computational Mechanics* 70 (4 Oct. 2022), pp. 867–878. ISSN: 0178-7675. DOI: 10.1007/s00466-022-02212-8.

[39] T. I. Zohdi. "A digital-twin and machine-learning framework for precise heat and energy management of data-centers". In: *Computational Mechanics* 69 (6 June 2022), pp. 1501–1516. ISSN: 0178-7675. DOI: 10.1007/s00466-022-02152-3.

[40] T. Zohdi. "A machine-learning framework for rapid adaptive digital-twin based fire-propagation simulation in complex environments". In: *Computer Methods in Applied Mechanics and Engineering* 363 (May 2020), p. 112907. ISSN: 00457825. DOI: 10.1016/j.cma.2020.112907.

[41] T. I. Zohdi. "Modeling and simulation of the infection zone from a cough". In: *Computational Mechanics* 66 (4 Oct. 2020), pp. 1025–1034. ISSN: 0178-7675. DOI: 10.1007/s00466-020-01875-5.

[42] M. Singh et al. "Applications of Digital Twin across Industries: A Review". In: *Applied Sciences* 12 (11 June 2022), p. 5727. ISSN: 2076-3417. DOI: 10.3390/app12115727.

[43] C. Pylianidis, S. Osinga, and I. N. Athanasiadis. "Introducing digital twins to agriculture". In: *Computers and Electronics in Agriculture* 184 (May 2021), p. 105942. ISSN: 01681699. DOI: 10.1016/j.compag.2020.105942.

[44] P. Goodrich et al. "Placement and drone flight path mapping of agricultural soil sensors using machine learning". In: *Computers and Electronics in Agriculture* 205 (Feb. 2023), p. 107591. ISSN: 01681699. DOI: 10.1016/j.compag.2022.107591.

[45] O. Randolph and B. Asiabanpour. "Energy Consumption Optimization in Off-Grid Vertical Farming". In: *IIE Annual Conference. Proceedings* (2020), pp. 861–866.

[46] D. Sambor et al. "Development of a Tool for Optimizing Solar and Battery Storage for Container Farming in a Remote Arctic Microgrid". In: *Energies* 13 (19 Oct. 2020), p. 5143. ISSN: 1996-1073. DOI: 10.3390/en13195143.

[47] G. Natarajan et al. "Modeling of air distribution inside a shipping container plant factory using computational fluid dynamics (CFD)". In: 2022, p. 020091. DOI: 10.1063/5.0117095.

[48] URL: https://www.agritecture.com/census.

[49] A. Jenkins. "Food security: vertical farming sounds fantastic until you consider its energy use". In: *The Conversation* (Sept. 2018). URL: https://theconversation.com/food-security-vertical-farming-sounds-fantastic-until-you-consider-its-energy-use-102657.

[50] May 2020. URL: https://www.worldwildlife.org/publications/indoor-soilless-farming-phase-i-examining-the-industry-and-impacts-of-controlled-environment-agriculture.

[51] "Vertical Crop Consultants". URL: https://verticalcropconsultants.com.

[52] *Multizone Series Seer 21*. MMRSHT48AS5. TGM. 2023. URL: https://refricenter.net/product-details.asp?id_product=623.

[53] *180 Pint Pro Series Dehumidifier*. 701600. Ideal-Air. 2023. URL: https://growershouse.com/filemediadownload?file=/I/d/Ideal_Air_Pro_Series_Dehumidifier_180_Pint_Manual.pdf.

[54] *F9 Air Mover*. 4035030. Quest. 2023. URL: https://www.questclimate.com/wp-content/uploads/sites/7/2020/02/Quest-Air-Mover-F9-Spec.pdf.

[55] *ThinkGrow Horticulture LED Growth Light*. Model-V. ThinkGrow. 2023. URL: https://www.thinkgrowled.com/#/modelv.

[56] *Sun 48 6500k 187 Watts*. HGC960441. AgroLED. 2023. URL: https://hydrobuilder.com/agroled-sun-48-led-6500k.html.

[57] *Leader Ecotronic 110, 1/2 HP Jet Pump - 960 GPH*. Ecotronic 110. Leader. 2023. URL: https://hydrobuilder.com/media/pdf/specs/leader-eco-jet-spec-sheet.pdf.

[58] *Growing Strawberries - Strawberries and More*. URL: https://web.extension.illinois.edu/strawberries/growing.cfm.

[59] *NREL Champion Photovoltaic Module Efficiency Chart*. 2023. URL: https://www.nrel.gov/pv/module-efficiency.html.

[60] S. Odeh. "Analysis of the Performance Indicators of the PV Power System". In: *Journal of Power and Energy Engineering* 06 (June 2018), pp. 59–75. DOI: 10.4236/jpee.2018.66005.

[61] *550W Monocrystalline Solar Panel*. RSP550D-144. Renogy. 2023. URL: https://www.renogy.com/content/RSP550D-144/RSP550D-144%20Datasheet.pdf.

[62] *Powerwall 3*. Tesla. 2023. URL: https://www.tesla.com/powerwall.

[63] E. Mengi, O. A. Samara, and T. I. Zohdi. "Crop-driven optimization of agrivoltaics using a digital-replica framework". In: *Smart Agricultural Technology* 4 (2023), p. 100168. ISSN: 2772-3755. DOI: https://doi.org/10.1016/j.atech.2022.100168. URL: https://www.sciencedirect.com/science/article/pii/S2772375522001320.

[64] C. Zhao et al. "A SIMPLE crop model". In: *European Journal of Agronomy* 104 (2019), pp. 97–106. ISSN: 1161-0301. DOI: https://doi.org/10.1016/j.eja.2019.01.009. URL: https://www.sciencedirect.com/science/article/pii/S1161030118304234.

[65] S. von Caemmerer, G. Farquhar, and J. Berry. "Biochemical Model of C3 Photosynthesis". In: *Photosynthesis in silico: Understanding Complexity from Molecules to Ecosystems*. Dordrecht: Springer Netherlands, 2009. Chap. 9, pp. 209–230. ISBN: 978-1-4020-9237-4. DOI: 10.1007/978-1-4020-9237-4_9.

[66] A. Senevirathna, C. Stirling, and V. Rodrigo. "Acclimation of photosynthesis and growth of banana (Musa sp.) to natural shade in the humid tropics". In: *Experimental Agriculture* 44.3 (2008), pp. 301–312.

[67] A. Senevirathna, C. Stirling, and V. Rodrigo. "Growth, photosynthetic performance and shade adaptation of rubber (Hevea brasiliensis) grown in natural shade". In: *Tree Physiology* 23.10 (2003), pp. 705–712.

[68] P. Siles et al. "Photosynthetic performance of banana ('Gros Michel', AAA) under a natural shade gradient". In: *VII International Symposium on Banana: ISHS-ProMusa Symposium on Bananas and Plantains: Towards Sustainable Global Production 986*. 2011, pp. 71–77.

[69] M. A. A. Mamun et al. "A review of research on agrivoltaic systems". In: *Renewable and Sustainable Energy Reviews* 161 (2022), p. 112351. ISSN: 1364-0321. DOI: https://doi.org/10.1016/j.rser.2022.112351. URL: https://www.sciencedirect.com/science/article/pii/S1364032122002635.

[70] H. Marrou et al. "Microclimate under agrivoltaic systems: Is crop growth rate affected in the partial shade of solar panels?" In: *Agricultural and Forest Meteorology* 177 (2013), pp. 117–132. ISSN: 0168-1923. DOI: https://doi.org/10.1016/j.agrformet.2013.04.012. URL: https://www.sciencedirect.com/science/article/pii/S0168192313000890.

[71] N. F. Othman et al. "Modeling of Stochastic Temperature and Heat Stress Directly Underneath Agrivoltaic Conditions with Orthosiphon Stamineus Crop Cultivation". In: *Agronomy* 10.10 (2020). ISSN: 2073-4395. DOI: 10.3390/agronomy10101472. URL: https://www.mdpi.com/2073-4395/10/10/1472.

[72] J. L. Monteith. "Evaporation and environment". In: *Symposia of the society for experimental biology*. Vol. 19. Cambridge University Press (CUP) Cambridge. 1965, pp. 205–234.

[73] A. Weselek et al. "Agrivoltaic system impacts on microclimate and yield of different crops within an organic crop rotation in a temperate climate". In: *Agronomy for Sustainable Development* 41.5 (2021), pp. 1–15.

[74] M. Elborg. "Reducing land competition for agriculture and photovoltaic energy generation– A comparison of two agro-photovoltaic plants in Japan". In: *International Conference on Sustainable and Renewable Energy Development and Design (SREDD2017)*. Vol. 3. 2017, p. 5.

[75] F. Letternmeier et al. *Agri-photovoltaic systems – Requirements for primary agricultural use English translation of DIN SPEC 91434:2021-05*. Standard. Berlin, Germany: Deutsches Institut für Normung, May 2021.

[76] M. D. of Energy Resources. *Solar Massachusetts Renewable Target (SMART) Program regulation 225 CMR 20.00*. Program Regulations. Massachusetts, United States: Massachusetts Department of Energy Resources, 2021. URL: https://www.mass.gov/doc/225-cmr-2000-final-071020-clean/download.

[77] C. Dupraz. "Combining solar photovoltaic panels and food crops for optimizing land use: towards new agrivoltaic schemes". In: *Renew Energy* 36 (2011), pp. 2725–2732. DOI: https://doi.org/10.1016/j.renene.2011.03.005.

[78] Y. Elamri et al. "Water budget and crop modelling for agrivoltaic systems: Application to irrigated lettuces". In: *Agricultural Water Management* 208 (2018), pp. 440–453. ISSN: 0378-3774. DOI: https://doi.org/10.1016/j.agwat.2018.07.001. URL: https://www.sciencedirect.com/science/article/pii/S0378377418309545.

[79] B. Valle et al. "Increasing the total productivity of a land by combining mobile photovoltaic panels and food crops". In: *Applied Energy* 206 (2017), pp. 1495–1507. ISSN: 0306-2619. DOI: https://doi.org/10.1016/j.apenergy.2017.09.113. URL: https://www.sciencedirect.com/science/article/pii/S0306261917313971.

[80] R. Mead and R. W. Willey. "The Concept of a 'Land Equivalent Ratio' and Advantages in Yields from Intercropping". In: *Experimental Agriculture* 16.3 (1980), pp. 217–228. DOI: 10.1017/S0014479700010978.

[81] S. of California. *California Irrigation Management Information System*. 2022. URL: https://cimis.water.ca.gov/Default.aspx.

[82] P. E. Campana et al. "Optimisation of vertically mounted agrivoltaic systems". In: *Journal of Cleaner Production* 325 (2021), p. 129091.